

POLITECNICO DI TORINO

Master of Science in Energy and Nuclear Engineering



**Politecnico
di Torino**

Master's Degree Thesis

Solar-Driven Reduction of Iron Oxides with Methane for Chemical Looping Application

Supervisors

Prof. Massimo Santarelli

Dr. Davide Papurello

Candidate

Ahmed Guri

March 2022

Abstract

In the present work the chemical looping process driven by the high heat temperature provided by a solar dish concentrator was assessed. This process aims at using water or carbon dioxide (or a mixture of the two) to produce hydrogen or carbon monoxide; starting from the mixture it's possible to obtain high value chemicals with further processes. Since Global Warming has become one of the most challenging issues of our era, finding new pathways for the decarbonization of the energy sector has become a vital issue. Thanks to thermochemical processes such as chemical looping it is possible to produce high value chemicals (hydrogen and syngas) but also to collect and reuse CO_2 with CCS (Carbon Capture and Storage) and CCU (Carbon Capture and Utilization) processes. In order for the process to be sustainable and non-polluting, it requires the exploitation of renewable resources; in the case here analyzed the solar dish positioned on the rooftop of the Energy Center will be used to drive the high temperature heat reaction. Both the experimental and numerical approach took place to analyze the reduction process of hematite (Fe_2O_3) reduction using methane (CH_4) as a reducing agent. During the experimental part of the work the attention was focused on the process happening inside the reactor, where the hematite was inserted, and on the choice of the reactor itself. The main aim was to understand the feasibility of the process and its effectiveness in non-artificial environment (laboratory). During our five main experiments the main issue was the high temperature reached on the focus of the solar dish concentrator, which didn't allow for long standing measurements, as the reactors' materials couldn't endure for extended duration the high heat of the concentrated solar radiation. Indeed, all the experiments had destructive effects on the reactors. This led to the necessity of focusing also on the aspect related to the material of the reactors, in order to understand the direction of possible future evolutions. For what concerns the numerical analysis, COMSOL Multiphysics was used. The focus of the simulation is the validation of the result of the data collected during the experiment and also of the data found in literature. The main goal was to recreate the chemical reaction happening inside the reactor, through a chemically focused simulation. In this simulation only the cylindrical reactor was considered. The solar concentrator's role was approximated to the solar radiation it concentrates, without considering its geometrical and optical features, for simplification. The main quantities related to the kinetic of the reaction were taken from literature, according to the boundary conditions of our experimental work. The numerical analysis allowed to obtain the evolution of the reduction reaction.

Summary

List of Figures	5
1 Introduction	9
1.1 Concentrated Solar Power (CSP) Technology	12
1.1.1 Parabolic-through collector	15
1.1.2 Linear Fresnel Collector	15
1.1.3 Central Receiver Collector	16
1.1.4 Parabolic Dish Collector	17
1.2 Thermodynamic and Optical analysis	19
1.2.1 Concentration Ratio	19
1.3 Maximum theoretical absorber temperature.....	24
$G_{sc} = A_{ap} P_s 4\pi r_s^2 = A_{ap} (4\pi r_s^2 \cdot \sigma \cdot T_s^4) 4\pi r_s^2$	24
1.4 Thermal and Optical losses	28
1.4.1 Optical losses.....	28
1.5 Thermal Losses	33
1.6 Analysis of the dish concentrator system	35
1.7 Mirror Material.....	38
1.8 Design of the opening area of the concentrator	40
1.9 Rim angle	40
1.10 Length of the focal point.....	42
1.11 Solar tracking system.....	43
1.12 Reactors Materials	44
1.12.1 Alumina	44
1.12.2 Hastelloy	48
1.12.3 Inconel	52
2 Literature Review.....	56
2.1 Thermochemical Cycles.....	56
2.1.1 Volatile Oxygen Carriers.....	57
$ZnO \rightarrow Zn + 1/2 O_2$	58
2.1.2 Non-volatile Oxygen Carriers	59
$Fe_3O_4 \rightarrow 3FeO + 1/2 O_2$	60
$3FeO + H_2O \rightarrow Fe_3O_4 + H_2$	60
2.2 Chemical Looping Combustion.....	60

2.3	Methane aided chemical looping reaction.....	64
2.4	Iron Oxides chemical looping.....	71
2.5	Co-doped iron oxides reduction	79
3	Experimental Activity at the Energy Center	82
3.1	Test Bench description	82
3.2	Experimental set-up	87
3.3	Test #1.....	89
3.4	Test #2.....	91
3.5	Test #3.....	93
3.6	Test #4.....	95
3.7	Test #5.....	97
3.8	Conclusions	100
4	Chemical simulation.....	101
5	Conclusions	109
	References	111

List of Figures

Figure 1 solar fuel production	10
Figure 2 high-temperature reaction for syngas production	11
Figure 3 yearly sun [1]	13
Figure 4 schematic example of CSP plant [2]	14
Figure 5 types of CPS receivers	14
Figure 6 Parabolic-through collector [1]	15
Figure 7 linear Fresnel collector [1]	16
Figure 8 central receiver collector [1]	16
Figure 9 parabolic dish collector [1]	18
Figure 10 Conical radiation with aperture of $\theta_s=4.65$ mrad	19
Figure 11 Scheme of a receiver hit by radiation with a generic angle θ [7]	20
Figure 12 parabolic dish collector scheme	21
Figure 13 Radiant flux density distribution in the focal spot of a paraboloid [8]	23
Figure 14 Maximum theoretical temperature of the absorber varying the concentration ratio	26
Figure 15 System efficiency depending on geometrical concentration ratio and collector reflectivity [8].....	26
Figure 16 Energy flows at the receiver [7].....	28
Figure 17 specular error scheme [7]	29
Figure 18 slope errors [7]	29
Figure 19 Receiver tube [9].....	31
Figure 20 Efficiencies for different concentrator systems [7].....	33
Figure 21 Correlation between T_{amb} and the receiver temperature [9]	34
Figure 22 dish concentration system	35
Figure 23 Cross section of parabolic dish [9]	36
Figure 24 parabolic dish collector da cambiare	37
Figure 25 Reflective coefficients [10].....	39
Figure 26 standard thick-glass mirror (left) and silver mirror (right) [7].....	39
Figure 27 Rim angle	41
Figure 28 focal point	42

Figure 29 Temperature dependence of Young’s modulus, shear modulus and Poisson ratio for alumina [11]	45
Figure 30 Fracture toughness trend of alumina with temperature	46
Figure 31 Creep behavior of alumina of the refractory type	47
Figure 32 Temperature dependence of residual strength after single quenching of alumina [11]	48
Figure 33 mass change as function of time during isothermal oxidation at 950°C for 72h [12]	49
Figure 34 weight gain vs. time for oxidation of Hastelloy C276 in (a) 0.01% and (b)100% oxygen environment [16]	51
Figure 35 flow curves for the current Inconel 718 at different temperature and strain rates [17]	53
Figure 36 tensile specimens A,B,C and D [18].....	53
Figure 37 Mechanical properties [18]	54
Figure 38 Tensile strenght, yield strenght and elongation vs. temperature [19].....	54
Figure 39 room temperatures of Inconel 686 [19]	54
Figure 40 mechanical properties with temperature [19]	55
Figure 41 Elastic modulus and Poisson's modulus for Inconel 686 [19]	55
Figure 42 Thermodynamic data for thermal reduction	59
Figure 43 basic principles of CH ₄ chemical-looping reforming [5]	62
Figure 44 Conversion of CH ₄ to CO ₂ as a function of temperature for different oxygen carriers [6]	63
Figure 45 specific surface area, porosity, tortuosity and diffusion coefficient [8]	65
Figure 46 composition of original and calcinated magnetite [8]	65
Figure 47 evolution of H ₂ , CO ₂ and CO during the isothermal reduction reaction at 1223 K (original magnetite) [8]	66
Figure 48 evolution of H ₂ , CO ₂ and CO during the isothermal oxidation reaction at 1223 K (original magnetite).....	67
Figure 49 oxidation and reduction step for original magnetite [8]	68
Figure 50 reduction and oxydation cycle for H ₂ , CO and CO ₂ [8]	68
Figure 51 reduction via methane of (a) original magnetite and (b) original magnetite after 6 cycles [8]	69

Figure 52 activation energy for different studies	70
Figure 53 chemical conversion given by thermodynamics [11]	72
Figure 54 Equilibrium composition results of the Fe/O system (100 mol of N ₂ , 1 mol of Fe ₂ O ₃ , P=1 bar) [11]	72
Figure 55 Equilibrium composition results of the Fe/O/H system (3 mol of FeO, 1 mol of H ₂ O, N ₂ atmosphere, P =1 bar) [11]	73
Figure 56 set-up of the experiment	74
Figure 57 Temperature measurements of a Fe ₂ O ₃ pellet heated under an inert atmosphere by a solar furnace [11]	75
Figure 58 x-ray diffraction pattern of solar-reduced Fe ₂ O ₃ under air or N ₂ atmosphere [11]	75
Figure 59 Results obtained from x-ray diffraction after heating Fe ₂ O ₃ up to 1700°C with a solar furnace [11]	76
Figure 60 schematic of the experimental set-up for the oxidation step [11]	77
Figure 61 mol fraction of hydrogen vs temperature produced by the reaction of FeO (30<dp<50 μm) and water.....	78
Figure 62 Reduction of doped iron oxides [12]	79
Figure 63 reduction reaction at 600°C, 700°C and 800°C [13]	81
Figure 64 Piping system (change the picture with a scheme) Errore. Il segnalibro non è definito.	
Figure 65 pumping system	83
Figure 66 weight of the hematite.....	84
Figure 67 Siemens display	84
Figure 68 solar dish collector	85
Figure 69 cylinder mounted on the solar collector.....	86
Figure 70 emerson gas analyzer	86
Figure 71 Carbon contents in reduced hematite for different temperature and CH ₄ concentrations (20% and 35%)	88
Figure 72 alumina tube after thermal shock.....	90
Figure 73 parabolic collector with covered reflected surface	91
Figure 74 results of test #3	94
Figure 75 result of test #4.....	95
Figure 76 Test #5 results	97

Figure 77 hastelloy tube failure..... 99

Chapter 1

1 Introduction

The unstoppable demographic increase and economic growth, together with a continuous rise in the urbanization level have led to a massive increase in the energy demand around the globe. Even if the last decade has been characterized by a large increase of the share of energy produced via renewable source, the trend of energy supply is still depending on hydrocarbon energy sources. The latter further depend on geographical distribution and extraction availability. Since the industrial revolution, the main route for energy production was fossil fuel exploitation; this led to a dramatic increase in the CO₂ levels in the atmosphere, as well as other Green House Gases (GHG), which are the main responsible for the global warming issue. To guarantee energy sustainability and global security it is necessary to take the path of decarbonization of the energy supply by utilizing alternative and clean resources. A key role will be played by renewable energy resources in order to implement the transition toward cleaner and more sustainable energy systems. The main issue about renewable resources is related to the volatility and intermittency of their nature. To address the variability of renewable resources a technical adaptation is necessary, aiming at the balance between the constantly changing supply and demand for energy. Therefore, the need for large-scale energy storage system is required to deal with this variability and intermittency of renewable resources. Supply and demand will have to be decoupled by shifting the produced energy on different time scales (hourly, daily and seasonally). In this perspective an important role is gained by energy carriers such as hydrogen and syngas (synthetic fuels), which can be produced exploiting spare energy produced from renewable energy systems. In general, syngas is a commercial scale liquid or gaseous fuel produced starting from low-energy carbon sources, such as coal, natural gas and biomass, which are valued at the expense of additional energy. Syngas is a gas mixture composed of varying amounts of CO and H₂; this exothermic conversion to fuel has been commercially available for a long time and has been exploited also for the Fischer-Tropsch technology. Furthermore, it is possible to make these processes more sustainable and eco-

friendlier by driving them with renewable energy resources (such as solar energy). Indeed, hydrogen and syngas are the base chemicals for the production of synthetic liquid fuels through industrial available processes. In fact, thanks to the magnitude and availability of the solar energy resource, solar-driven technologies are considered a permanent solution to both oil independence and climate change. The products of processes to produce high value chemicals using solar energy as the driving force are called solar fuels; in this categorization fall also hydrocarbons and alcohols produced from the reaction between hydrogen and CO that are originated by solar aided dissociation or produced using metal powders obtained by the solar thermal reduction of metal oxides. In the following picture it is possible to see the possible pathways for syngas production:

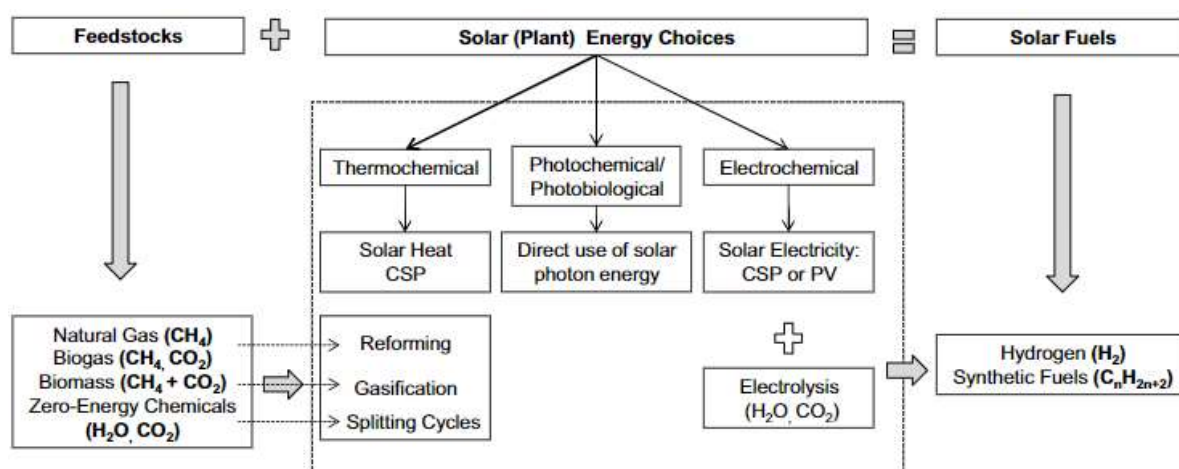


Figure 1: Solar Fuel production.

As it can be seen, there are three main routes to follow for the solar fuel production: photochemical/photobiological, thermochemical and electrochemical.

Photochemical/photobiological are low-temperature processes that directly exploit the solar photon energy. On the other side, thermochemical processes exploit high temperature heat generated by concentrated solar rower systems to drive the reaction that converts other fossil and non-fossil fuels into syngas. As it can be seen from figure 1, methane steam reforming, gasification of solid carbonaceous materials (coal or biomass) and water splitting belong to this category. Among these categories the water splitting/carbon monoxide splitting thermochemical cycle has a significant role in the optic of valorizing CO_2 present in the

atmosphere by treating it as a carbon containing raw material and not as a waste of production processes.

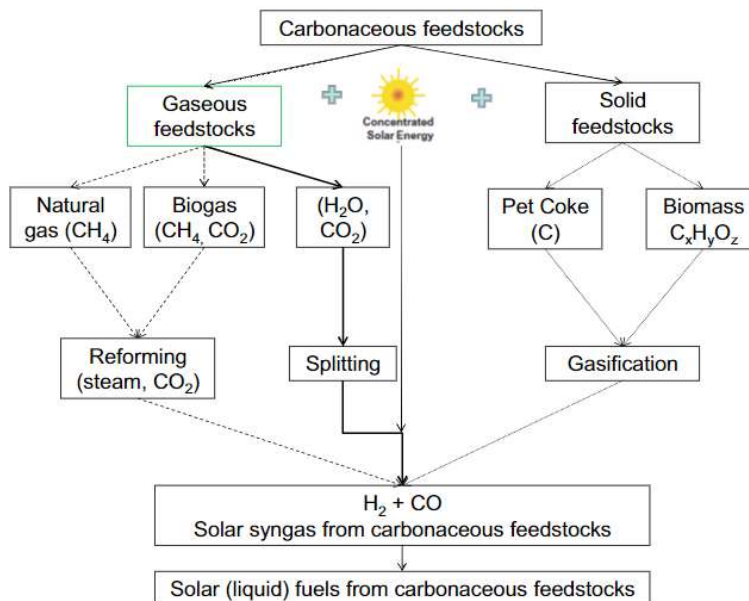


Figure 2: High-temperature reaction for syngas production;

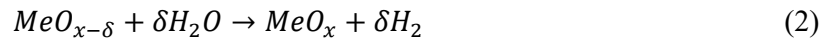
Conceptually, the simplest way to get the water split into hydrogen and oxygen would be a single-step thermal dissociation called water thermolysis; actually, this would bring many issues such as the need for very high reaction temperatures (around 2500 K) and an efficient separation technique of H_2 and O_2 in order to avoid the formation of an explosive mixture. A water-splitting thermochemical cycle allows to work with lower temperatures and have proper H_2/O_2 separation. In these types of processes water is split into hydrogen and oxygen through loop chemical reactions using intermediate reactions and substances; these intermediate substances will be recycled and reused within the process. Having a heat process at 1200K would require more than two steps for the water splitting to happen; this would bring a decrease in productivity due to the losses in heat transfer and the inefficiencies related to each step. Chemical looping for H_2 generation is a promising technology that can be used to convert fossil fuels to produce pure hydrogen and allow capturing CO_2 using oxygen carriers. The main feature that makes the oxygen carriers suitable for this application is that they have multiple state of oxidation; an example is represented by the iron oxide that presents different oxidation states: Fe_2O_3 , Fe_3O_4 , FeO and Fe . Thanks to the development in large-scale optical systems, it is possible to achieve mean solar concentration ratios of 5000 suns which would allow to reach stagnation temperatures up to 3000K. These temperatures would allow the production of

hydrogen via two step thermochemical water splitting. During this process the starting oxide is reduced, using high temperature heat, in the first step releasing oxygen molecules; then this reduced oxide reacts with water in the second step of the reaction to produce hydrogen and the starting oxide. The reaction can be represented in the following:

Solar-driven exothermic step:



Exothermic step:



In case of CO_2 splitting the reaction would be:



For this study, among the metal oxide that can be used as oxygen carrier, hematite (Fe_2O_3) was selected since it is relatively inexpensive, readily available as natural mineral sand also environmentally safe compared to other metal oxide. The present study was carried out in the Energy Center Lab (Turin), using the solar dish placed on the roof, with the aim of analyzing the most significant parameters of the system and to the feasibility of the process in a non-controlled environment.

1.1 Concentrated Solar Power (CSP) Technology

Utilization of solar energy is considered one of the most competitive approaches to solve the GHG related issues. Solar energy is the most abundant energy resource on Earth, with approximately 885 million TWh of energy reaching the planet surface every year. This amount of energy can well cover the annual energy consumption of the entire human population,

estimated at 104,426 TWh by 2012 [1]. The fact, however, that the solar flux distribution over the surface of the planet is non-uniformly distributed, and is constantly changing, represents a large technical challenge. This is one of the reasons why the exploitation of solar energy is not at its maximum capacity. In the following picture it's evident that the solar radiation lack uniformity in its distribution all over the globe:

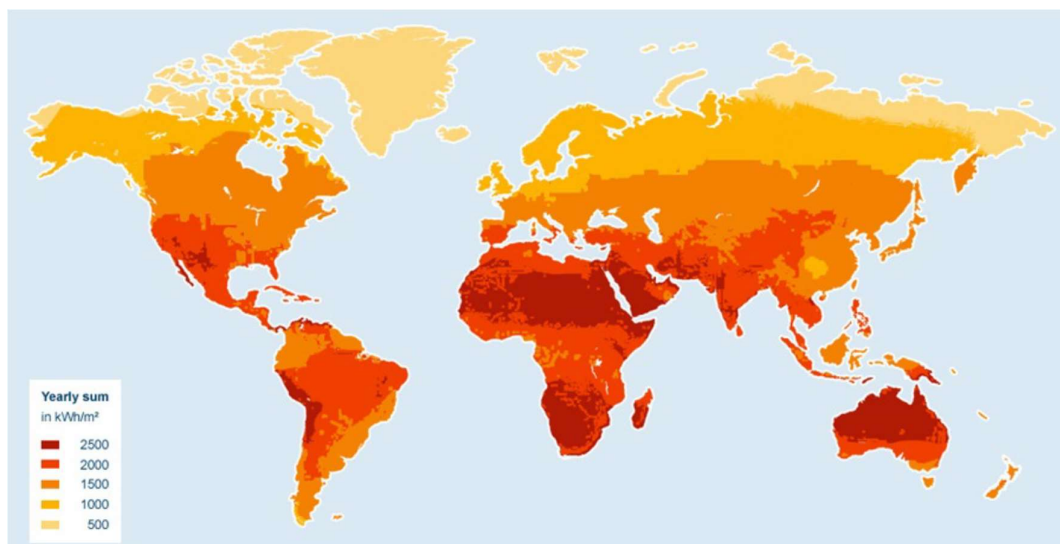


Figure 3: Yearly sun [1].

Lately, technologic development and cost reductions, pushed by policies reflecting the need for accelerating clean energy development, brought competitive penetration of solar power in suitable markets (such as South Africa), and in other well-developed nations (Germany). There most important solar energy technologies that can allow, today, to harvest this abundant energy resource are solar photovoltaics (PV) and concentrating solar power (CSP). In particular the concentrated solar power (CSP) technology is a promising option: in the last few years making this technology low cost and large-scale has become a key issue. A concentrated solar plant (CSP) is a system in which the solar radiation is captured using mirrors and concentrated on a surface in order to obtain high temperature heat, that is exploited thanks to the heat exchange network and a power block (these kinds of plants are often composed by a storage system). In the plant, the solar radiation is firstly concentrated, and then transformed into thermal energy that is taken away by the heat transfer fluid (HTF) in the receiver. Then, the thermal energy can be stored in the thermal storage unit or utilized to produce high-temperature steam or gas in heat exchangers; this gas/steam will be used to run a power cycle for electricity production[2]. In the following picture the CSP structure is summarized:

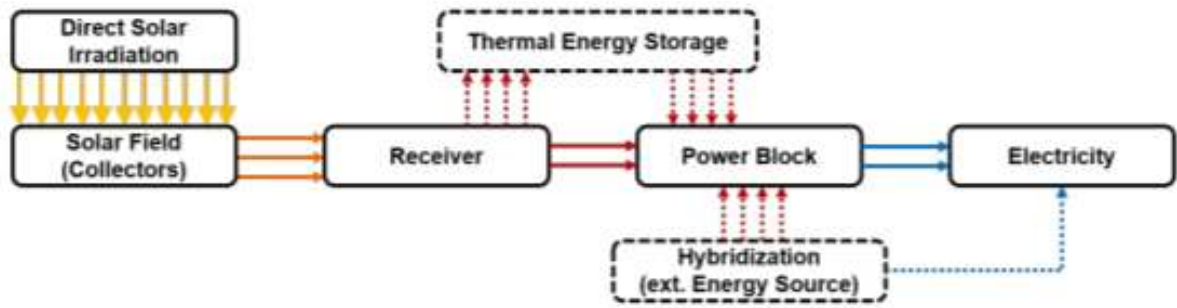


Figure 4: Schematic example of CSP plant [2].

Electricity production is not the only possibility for this technology; indeed, it can provide process heat for industrial processes, in the metallurgical sector for instance. Indeed, the possibility to provide controllable power on demand, either through TES integration or through hybridization, is what makes CSP plants “*dispatchable*”, which is one of their main competitive advantages. That’s why CSP is one of the few renewable alternatives that have already penetrated the market of large power generation. The CSP technologies can be classified into the following four types: parabolic-trough collector (PTC), linear Fresnel collector (LFC), solar power tower (SPT), and parabolic-dish collector (PDC), that can be seen in the picture:

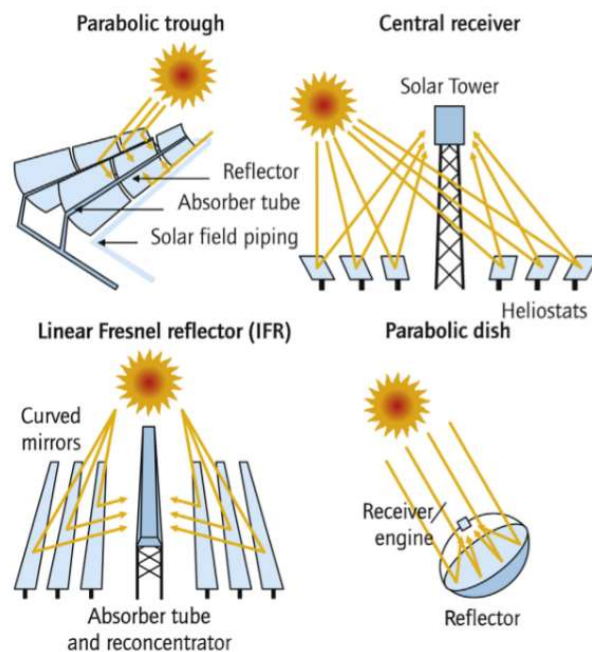


Figure 5: Types of CPS receivers[1].

1.1.1 Parabolic-through collector

The parabolic through collectors are mobile collectors that focus the radiation on a line: they consist of parabolic shape mirrors and a linear tubular receiver, as it can be seen in the figure. The radiation hits the outer cylindrical surface of the linear tubular receiver, which is located along the focal line of the parabolic channel.

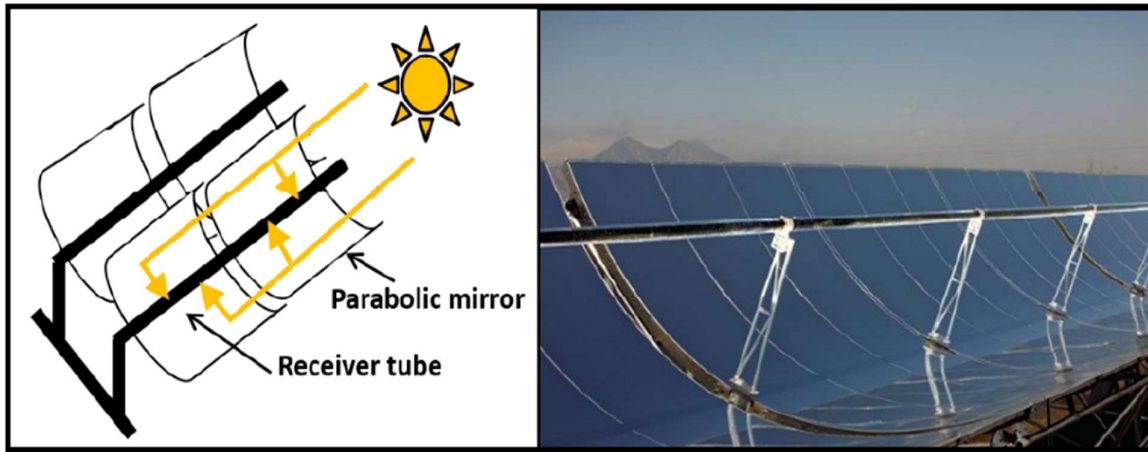


Figure 6: Parabolic-through collector [1].

It is the most developed among all CSP technologies and it covers up to 85% of the total CPS installations around the world. The receiver consists of a metal pipe enclosed by a vacuum tube (used to minimize convection losses); the HTF flows through the tubular external receiver. The tracking system allows the collector to follow the solar path on its longitudinal axis. These types of collectors are generally used to carry heat for the generation of steam in a steam cycle. Due to technological limitations regarding the high temperature fluid, heat can be delivered at a maximum temperature of 390°C.

1.1.2 Linear Fresnel Collector

Linear Fresnel (LF) collectors are composed by long row flat mirror segment that focus the solar radiation on a fixed linear receiver. Thanks to a tracking system the mirrors rotate in order to keep the radiation focused on the receivers. This technology is very similar to the PT collectors; however, the low profile and the less complex fixed structure makes the LF cheaper.

This doesn't compensate a lower efficiency, which has led to a slower development of this technology. Steam is often used as a working fluid for this kind of concentrators.

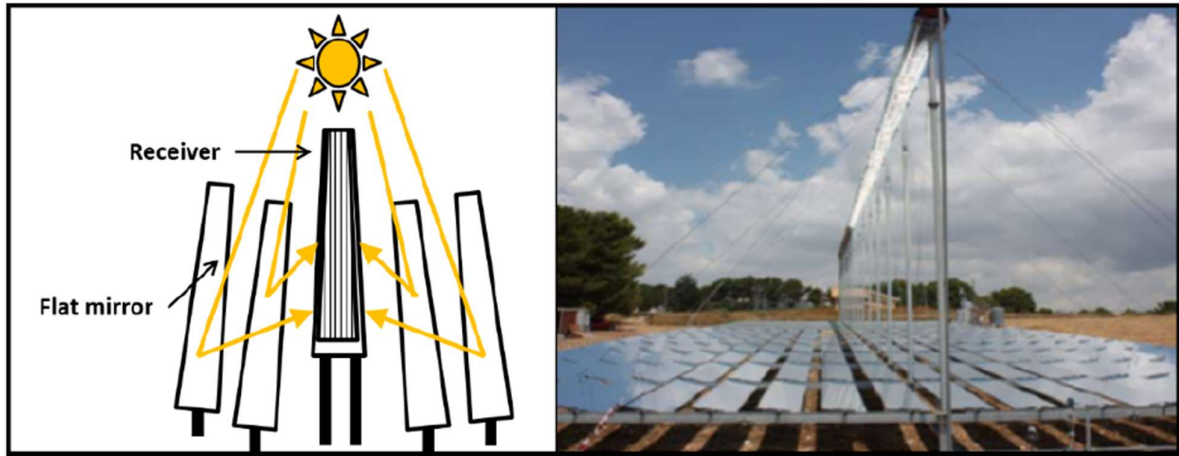


Figure 7: linear Fresnel collector [1]

1.1.3 Central Receiver Collector

Central receiver (CR) systems are composed by an array of tracking mirrors (heliostats), which concentrate the direct radiation onto a central receiver placed in an elevated support, usually referred to as the tower, as it can be seen in the following figure:

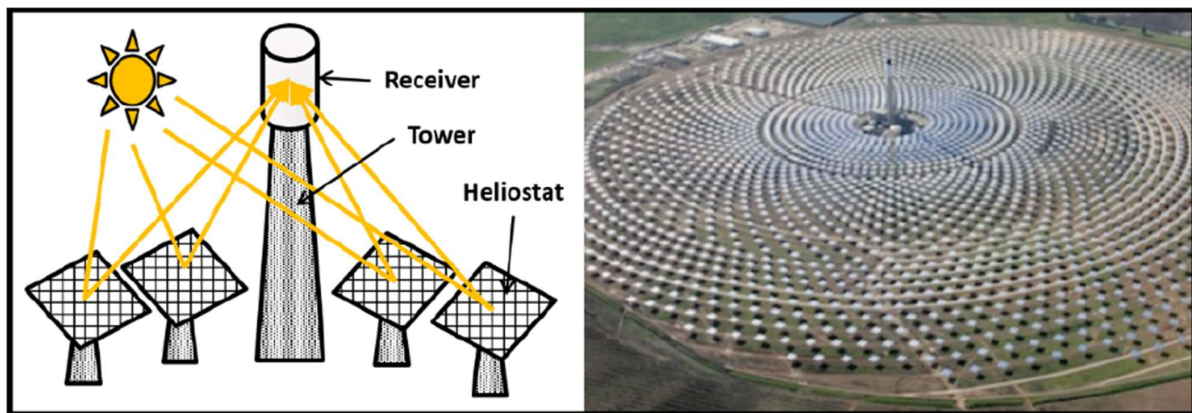


Figure 8: central receiver collector [1].

This is the fastest increasing technology to date, and it accounts for 14% of the world spread CPS technologies. The main advantages of this technology are:

- i. Solar-to-heat and heat-to-electricity conversion processes occur in a confined area.
- ii. It can reach higher temperatures than PT collectors.
- iii. Several commercially available TES (thermal energy storage) can be integrated.
- iv. Has great potential for efficiency improvement and cost reduction.

There are several possibilities for HTF choice, according to the CRC and TES systems considered; in particular it is possible to use air, molten salt or water/steam. The systems in which water is used are called Direct Steam Generators (DSG) and they don't require any intermediate heat carriers (which means that heat transfer losses are reduced). The main disadvantage of the DSG system is that up to date no cost-effective solution exists. On the other hand, molten salts can be used both as HTF and TES media, which means that it is possible to reduce the number of components and therefore the cost of the system and of the integration of TES. The high temperatures reached by this system allow it to use air as HTF that will be fed to a gas turbine for electricity production. However, this has not yet been proven at large scale and presents several technological issues such as the maximum temperature that the material composing the receiver can reach and the development of a suitable TES system.

1.1.4 Parabolic Dish Collector

In Parabolic-dish collectors the solar radiation is reflected on the receiver which is placed on the focal point of the dish. Here, the radiation is absorbed and transferred to the HTF for electricity production or to the thermochemical process to drive endothermic chemical reactions. Being point-focusing technologies (theoretically), dish systems can reach very high concentration ratios, which allows to reach higher temperatures and efficiencies; indeed these system have the highest optical efficiencies among other CSP technologies and are able to reach a solar-to-electric efficiency of 30%[3] . Thanks to the flexibility and modularity of this technology it is possible to install the in stand-alone and small-scale configuration or for large scale applications[3]: it is possible to install a large number of dishes in a solar park. Parabolic-dish collector's main advantages are:

- i. High power densities.
- ii. Moisture resistance.

iii. Long lifetime.

The tracking system is of the biaxial type. Generally, this technology is used for electricity production using a Stirling engine (power block), as shown in Figure 9:

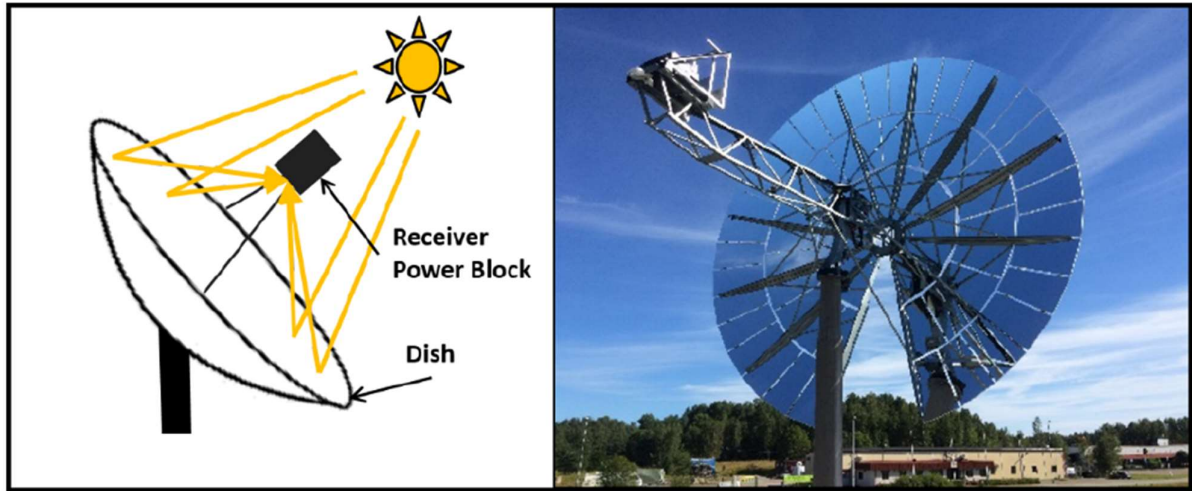


Figure 9: Parabolic dish collector [1].

The solar dish system is composed by a paraboloidal concentrator, a receiver, a biaxial tracking system and, according to the application, an engine. Due to non-idealities, such as the sun radiation which is spread on a cone of aperture 4,65 mrad (due to the finite diameter of the sun) and the non-perfect reflectivity of the mirrors, the focus of the dish is not a point but a finite region around the focal point.

1.2 Thermodynamic and Optical analysis

1.2.1 Concentration Ratio

While analyzing a CSP system it is necessary to consider that there are several sources of losses that deviate the actual results from the ideal one. The main phenomena that reduce the efficiency of the conversion chain are the thermal losses, which can be found at the receiver level, or the optical ones, that belong mostly to the concentrator level. An important factor that defines the performances of a CSP system is the solar concentration ratio, which is defined as the ratio between the radiation intensity in the focal area and the radiation intensity before the concentration; it is often approximated to the ratio between the area of the reflective surface, which captures and reflects the solar radiation, and the area, which is intercepted by the reflected radiation, on the receiver surface. Its expression can be written as:

$$C_{geom} = \frac{S_c}{S_r} \quad (1.1)$$

Where S_c is the concentrator surface, while S_r is the reflected surface. From this formula it may appear that it is possible to reach any value of the concentration ratio, having an ideal reflective surface and a punctual focal surface. However, the solar radiation doesn't reach the earth atmosphere with perfectly parallel rays, which means that the concentrated surface cannot be a point but must be a finite surface: the sun shape is a finite surface, not a point.

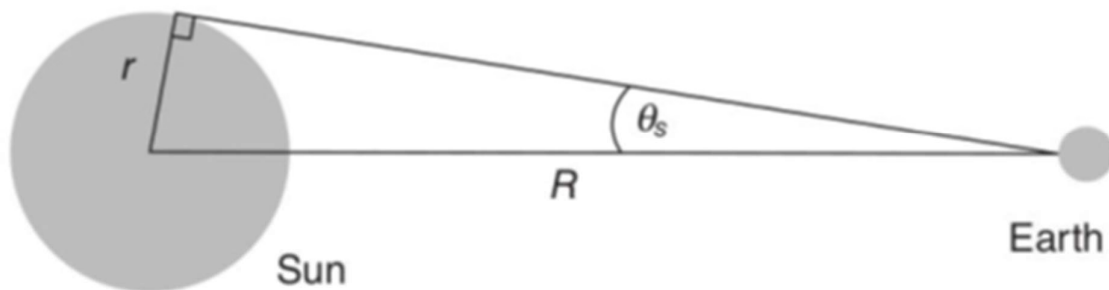


Figure 10: Conical radiation with aperture of $\theta_s=4.65$ mrad.

The main goal is to reach the highest concentration factor possible; however, there are some thermodynamic limits concerning the solar radiation. Considering the conical radiation aperture before mentioned, it is possible to calculate the maximum solar radiation reaching the earth surface with the following formula [5]:

$$G = G_0 \left(\frac{r}{R}\right)^2 = G_0 \left(\frac{R \sin \theta_s}{R}\right)^2 = G_0 \sin^2 \theta_s = \sigma T_s^4 \sin^2 \theta_s \quad (1.2)$$

Approximating the receiver, having an area A_R with a black body at temperature T_R , and supposing that the receiver is hit by the incident solar radiation without losses, it is possible to write:

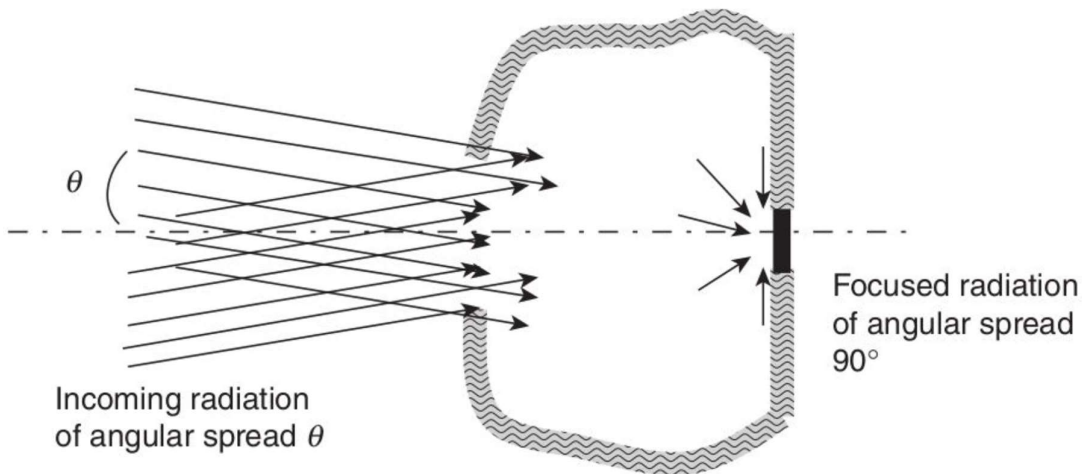


Figure 11: Scheme of a receiver hit by radiation with a generic angle θ .

In which the expression of solar irradiance previously obtained is equal to the power absorbed by the receiver. According to the second law of thermodynamics, the temperature of the receiver will always be lower than the sun temperature. As a consequence, the geometric concentration factor of a punctual concentration device, in perfect equilibrium conditions ($T_R = T_S$), will have a maximum threshold value. Therefore, considering the expression provided for the concentration ratio, the maximum theoretical value of concentration reachable by a system that focuses the radiation in a single point can be written with the following expression [4]:

$$G_{c,punct} = \left(\frac{A_{opening}}{A_R} \right) = \frac{A_C}{A_R} \leq \frac{1}{(\sin \theta_s)^2} = 46200 \quad (1.3)$$

The theoretical temperature corresponding to the maximum concentration ratio is 5500°C; however, this value of the concentration is obtained with the assumption of ideal conditions. In reality, there are some optical limits that make this value much lower than the ideal one. In particular, considering a parabolic dish collector with flat receiver, it is possible to write the concentration expression as:

$$C_{g,flat} = \frac{\pi R^2}{\pi t^2} \approx \frac{(\sin \phi_R)^2}{4 (\sin \theta_s)^2} \quad (1.4)$$

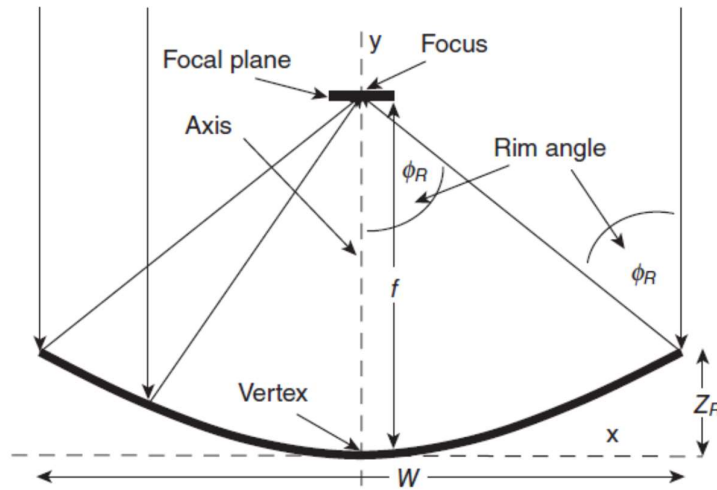


Figure 12: Parabolic dish collector scheme.

Where $2t$ is the length of the receiver and ϕ_R is the rim angle.

The derivative is calculated in order to find the maximum value of $C_{g,flat}$:

$$\frac{dC_{g,flat}}{d\phi_R} = 0 \quad (1.5)$$

$$\Phi_{R,max} = \frac{\pi}{4} \quad (1.6)$$

From which we obtain the maximum concentration ratio:

$$C_{g,flat,max} = \frac{1}{4} C_{g,punct} \quad (1.7)$$

Of course, the value of the concentration factor changes according to the shape of the receiver and the collector. It is possible to see that, considering a case study free of optical and geometrical imperfections, in which the receiver is considered as a black body, the optical limits related to the geometrical features of the system are much lower than the thermodynamic limits given by the maximum value of the theoretical concentration ratio achievable, as shown in the following table [5]:

Table 1: Maximum theoretical concentration ratio and optical limit for different solar concentration systems [7].

	Thermodynamic limit	Edge Ray optical limit
Dish Flat Aperture	46200	11550
Dish Spherical Aperture	46200	11550
Trough Flat Aperture	215	108
Trough Cylindrical Aperture	215	68.5

It can be seen that there is a huge difference between the thermodynamic limit and the optical limit of the concentration ratio for a parabolic dish collector; indeed, the first one, which is equal to 46200, refers to the maximum punctual value, while the second one, that is equal to 11500, refers to the concentration of the radiation calculated over the whole solar shape. It is important to highlight that these values are obtained for the forementioned type of technology and in case of ideal reflective surface. It is also necessary to consider a punctual concentration ratio taking into account that the radiant flux density varies within the focal spot: the aim is to

determine the concentration ratio in relation to a specific point in the focal area. The uneven radiant flux density distribution within the focal spot is a direct consequence of the beam spread of the direct solar radiation, which on its part is a consequence of the extension of the Sun shape. The consequence of that is that the inner part of the focal spot shows a much higher flux density and hence a higher punctual concentration ratio than the outer parts. Supposing that the direct normal irradiance at the collector aperture is about 800 W/m^2 (a typical value on a European summer day), real parabolic dish systems, where optical and geometrical losses are not neglected, can reach local concentration values up to 2000-6000. This concept is summarized in the following picture [5]:

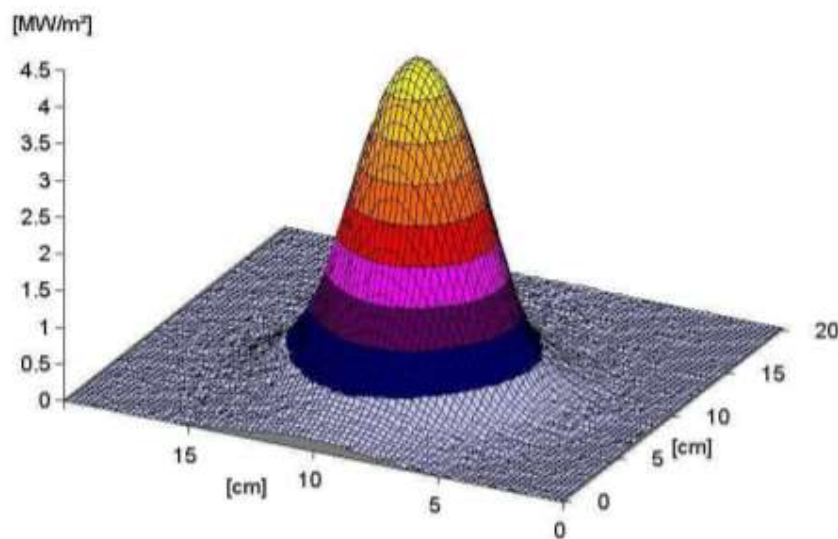


Figure 13: Radiant flux density distribution in the focal spot of a paraboloid [5].

This is why, for high temperature applications, it might be convenient to exploit the inner part of the focal point, where the concentration ratio results higher.

The main reasons why the ideal and theoretical concentration ratio are so different can be related to two main factors:

- i. Geometrical imperfections, due to superficial flaws of the reflective surface and to orientation mistakes.
- ii. Limits of the materials: reflection coefficient lower than one.

In the following paragraph the relationship between maximum temperature of the absorber and concentration ratio will be assessed.

1.3 Maximum theoretical absorber temperature

The correlation between the concentration ratio and the maximum theoretical temperature reachable by the absorber is now addressed. According to Stefan-Boltzmann law the power emitted by a black body is related to its surface and temperature:

$$P = A \sigma T^4 \quad (1.8)$$

It is possible to calculate the power emitted by the sun as:

$$P_s = 4\pi r_s^2 \cdot \sigma \cdot T^4 \quad (1.9)$$

From which it is possible to obtain the solar constant:

$$G_{sc} = \frac{P_s}{4\pi r_{ts}^2} = 3.85 \frac{10^{26}}{4\pi(1.496 \cdot 10^{11})^2} = 1367 \text{ W/m}^2 \quad (1.10)$$

Where $r_s = 696000 \text{ km}$ be the sun radius, $r_{ts} = 1.496 \cdot 10^{11} \text{ m}$ the mean distance between the sun and the Earth.

It is possible now to write the expression of the power received by the opening surface of a collector (neglecting atmospheric losses):

$$G_{sc} = \frac{A_{ap} P_s}{4\pi r_{ts}^2} = \frac{A_{ap} (4\pi r_s^2 \cdot \sigma \cdot T^4)}{4\pi r_{ts}^2} \quad (1.11)$$

The radiative power reflected on the absorber, considered a black body of surface A_{ab} , is given by the formula:

$$P_{ab} = A_{ab}\sigma T_{ab}^4 \quad (1.12)$$

The maximum temperature that can be reached by the absorber can be found when the power at the absorber is equal to the power received by the collector:

$$P_{ab} = \dot{Q}_{ap} \quad (1.13)$$

$$A_{ab}\sigma T_{ab}^4 = A_{ap}\sigma T_s^4 \frac{r_s^2}{r_{ts}^2} \quad (1.14)$$

Through some approximation we can introduce the maximum concentration ratio as:

$$\frac{r_s^2}{r_{ts}^2} = \frac{1}{C_{max}} \quad (1.15)$$

$$A_{ab}T_{ab}^4 = A_{ap}T_s^4 \frac{1}{C_{max}} \quad (1.16)$$

Knowing that the maximum concentration can be calculated as the ratio between the opening area and the absorbing one, it is possible to obtain the expression of the absorber temperature in relation to the concentration ratio:

$$T_{ab} = T_s \left(\frac{C}{C_{max}} \right)^{\frac{1}{4}} = 5777 \left(\frac{C}{46200} \right)^{\frac{1}{4}} \quad (1.17)$$

In the following graph it is possible to see the correlation between Tab and C:

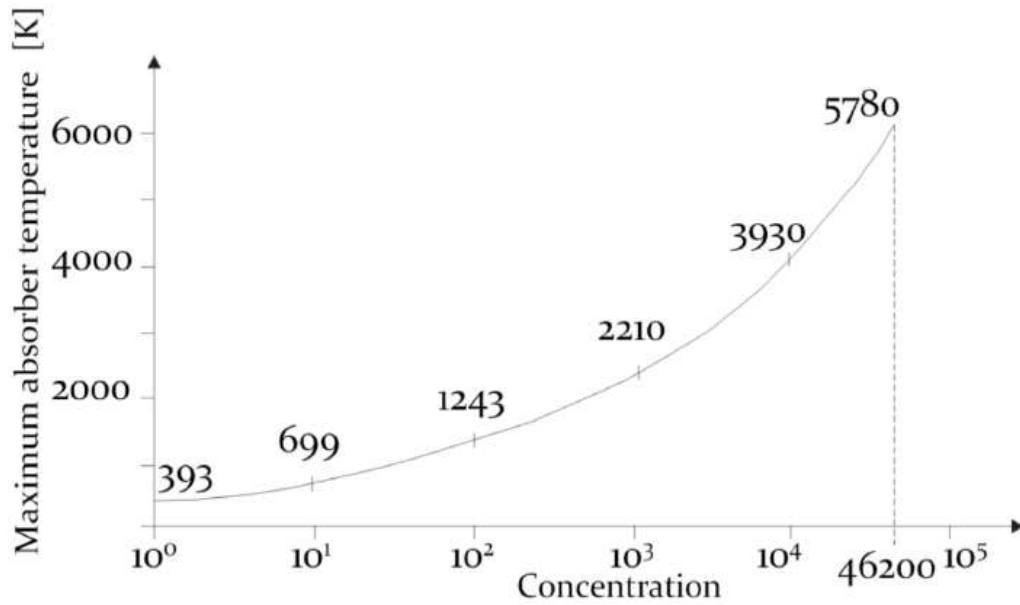


Figure 14: Maximum theoretical temperature of the absorber varying the concentration ratio [5].

The higher the concentration ratio, the higher the temperature on the absorber. It can also be seen that increasing C the efficiency of the system increases [5]:

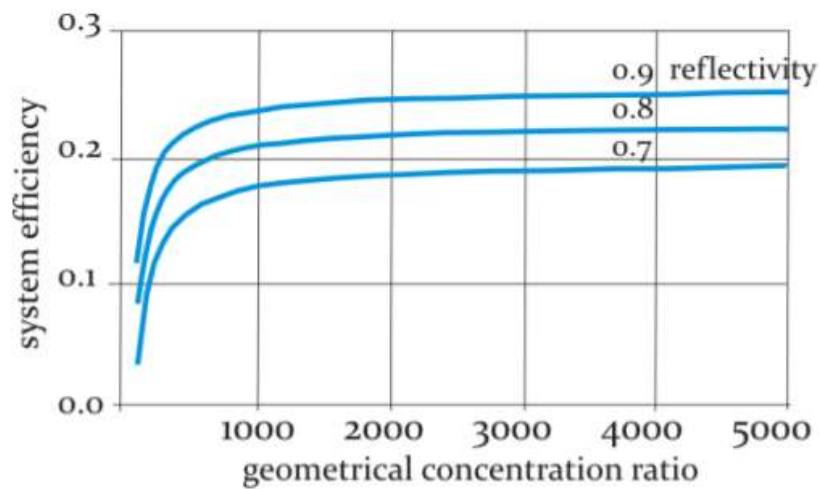


Figure 15: System efficiency depending on geometrical concentration ratio and collector reflectivity [5].

However, the expression of temperature written before is just theoretical, because many assumptions were made to obtain it: both the sun and the absorber were treated as black bodies, which is an important approximation because in nature no body behaves as a perfect black body. It is possible to reduce the emissivity of the absorber by using some selective coatings that allow it to reach higher temperatures. Writing the expression of temperature, the atmospheric phenomena of dissipation of the solar radiation were not considered. Moreover, just radiation was taken into account, neglecting all the convective and conductive heat transfer phenomena that can develop during the process, and that would lead to a reduction of the maximum temperature reachable.

1.4 Thermal and Optical losses

In the following figure we can see a schematic representation of the losses that occur at the receiver level: there are thermal and optical losses that make the usable power lower than the power that is projected on the receiver.

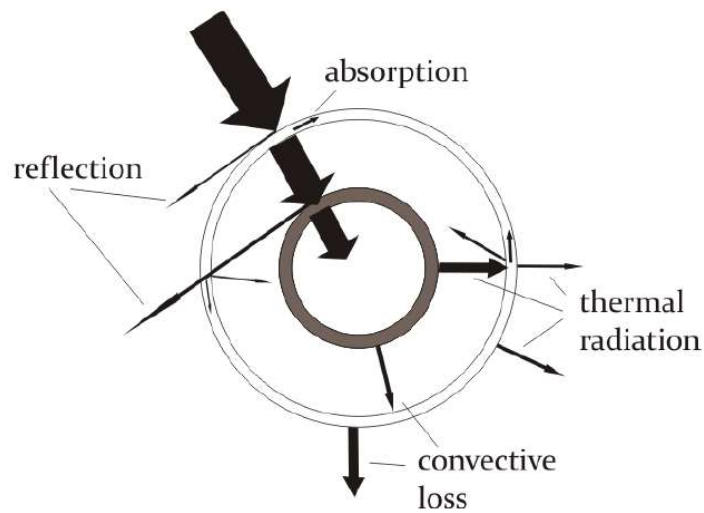


Figure 16: Energy flows at the receiver

1.4.1 Optical losses

1.4.1.1 Specularity Errors

These losses are related to very local roughness effects due to mirror production process, that imply having a non-perfect surface of the mirror and which leads to reflection that is not symmetrical.

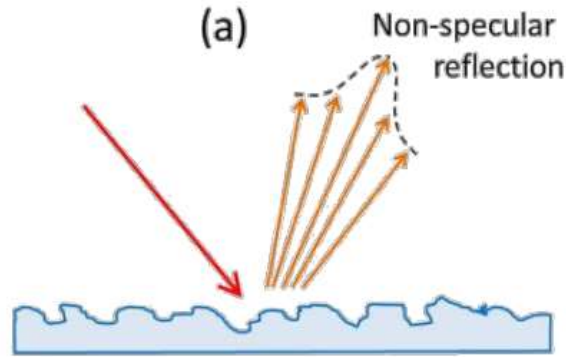


Figure 17: *Specularity error scheme*

These geometrical imperfections that are present on the surface of the mirrors can be either macroscopic or microscopic. The macroscopic errors are mostly related to imperfections of slope or shape, while the microscopic ones are present due to roughness on the surface of the mirrors that will reflect the incident rays with less precision.

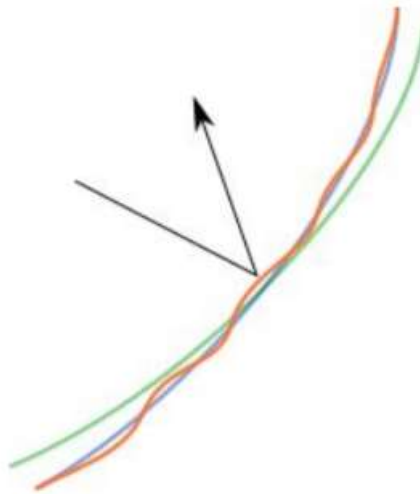


Figure 18: *Slope errors*

The optical losses, quantified as the amount of reflected radiation that don't hit the absorber, can be defined using the intercept factor, which is the ratio between the reflected radiation that hits the absorber and the total radiation which is reflected. Generally speaking, intercept factor for parabolic dish system can reach values up to 0,96-0,97. Higher values of this factor can be reached but would require investment cost which are too high, having just a slight increase in the overall efficiency. Furthermore, to increase the intercept factor, a bigger area of the absorber

is required; this would lead to an increase in thermal losses, due to the increase of the surface involved in the heat exchange process.

1.4.1.2 Blocking Losses

They occur when the reflected radiation encounters an obstacle (a mirror for instance) and cannot reach the receiver (spillage losses).

1.4.1.3 Shading Losses

The phenomenon of shading is related to the slope of the solar rays in respect to the reflective surfaces. In this case not all of the reflective surface is hit by solar rays due to the interference of some obstacles, like buildings for instance. The shading effect depends mostly on the disposition of the heliostat arrays and on the slope of the solar radiation. Lately, systems of ray tracing have been developed in order to maximize the efficiency of solar fields in the case of central tower systems, where the shadowing phenomena can be more relevant.

1.4.1.4 Reflection, Absorption and Transmittance Losses

Reflection losses take place when there is not perfect reflectivity of the mirror surface; it can be due to the slope error, which occurs due to local waviness of the surface for a length in the order of 1 cm-1m, or to specular errors, caused by surface roughness of much smaller dimension. Absorption coefficient is related to the materials of which the absorber is composed. The selective coatings of which the absorber tube is made have low reflectivity in the solar spectrum, which leads to high values of absorption, up to 95%. For what concerns transmittance, its values depend on the composition of the glass adopted for the application and the presence of dust on its surface; soiling effect affects directly this factor: the cleaner the surface the higher the transmittance coefficient.



Figure 19: Receiver tube [6].

1.4.1.5 Cosine Losses

These losses occur when the reflecting mirror is not perfectly oriented in the perpendicular direction with the solar radiation; this implies that the radiation will meet a smaller reflective surface, compared to the normal direction, and thus the overall reflected radiation is smaller than the ideal case. This source of error is related to tracking imperfections, that lead to a non-perfect alignment of the normal direction of the mirror with the solar rays. This issue is more relevant for single-axis tracking devices.

1.4.1.6 Atmospheric Attenuation Losses

Related to the atmospheric scattering phenomena that takes place in the path from the mirror to the receiver.

1.4.1.7 Overall Consideration

Optical losses are also produced at the glass tube as well as at the absorber tube. The glass tube has only a limited transmittance so that a part of the radiation is reflected, and another part is

absorbed. As mentioned before, antireflective coatings and highly transparent glass materials reduce the loss to around 4%. The absorber tube has only a limited absorptance so that another part of the incoming radiation is reflected at the absorber tube. Selective coatings reduce this loss to around 5%. These optical losses amount to

$$\frac{\dot{Q}_{loss,opt}}{A_{rec,act}G_{rec}} = 1 - (1 - 0.04)(1 - 0.05) = 8.8\%$$

Where G_{rec} is the irradiance on the active receiver surface area $A_{rec,act}$.

This equation relates the losses to the active receiver surface area and not to the total receiver surface area. This is the case because an additional optical loss has to be taken into account: the bellows and metal shields at the ends of the receiver reduce the active receiver area by nearly 4% (Siemens indicates 3.6%). Taking into consideration this additional loss and assuming the mentioned value, the optical losses over the whole receiver amount to [6].

$$1 - (1 - 0.036)(1 - 0.04)(1 - 0.05) = 12.1\%$$

It is possible to summarize all the losses mentioned with a single expression, by introduction the field efficiency (efficiency of the whole solar field or more in general, of the concentration system), which contains all the sources of loss from the optical and geometrical point of view: cosine efficiency, shadowing efficiency, blocking efficiency, reflection efficiency and atmospheric attenuation efficiency.

$$\eta_{field} = \eta_{cos}\eta_{shado} \eta_{block}\eta_{refl}\eta_{atten}$$

In the following the different efficiencies of different concentrator systems are listed:

	$\bar{\eta}_{\text{shade}}$	$\bar{\eta}_{\text{cos}}$	$\bar{\eta}_{\text{refl}}$	$\bar{\eta}_{\text{block}}$	$\bar{\eta}_{\text{atmos}}$	$\bar{\eta}_{\text{rcv,th}}$	$\bar{\eta}_{\text{rcv,opt}}$	$\bar{\eta}_{\text{trans}}$	$\bar{\eta}_{\text{field}}$
LFR	0.786	0.758	0.940	0.888	1.00	0.907	0.923	0.997	0.415
trough	0.879	0.847	0.940	1.00	1.00	0.921	0.888	0.979	0.558
tower	0.966	0.844	0.940	0.991	0.955	0.928	0.974	0.989	0.655
dish ₁	0.947	1.00	0.940	1.00	1.00	0.91		0.965	0.782
dish ₂	0.965	1.00	0.940	1.00	1.00	0.91		0.962	0.794

Figure 20: Efficiencies for different concentrator systems

1.5 Thermal Losses

The main source of thermal losses is located at the receiver level, where the heat provided by the concentrated solar radiation is balanced by the heat absorbed by the heat transfer medium (that flows inside the receiver), and by the losses related to heat transfer phenomena between the receiver surface, at higher temperature, and the surrounding atmosphere. The main source of thermal losses are thermal radiation, convection, and heat conduction. Heat conduction and convection between the hot absorber tube and the cooler glass tube can be reduced considerably introducing a vacuum. Heat conduction can be neglected. The thermal losses are strongly related to the temperature difference between the absorber tube and the ambient temperature, as shown by the results of the experiments on Solel UVAC3 receiver, done with an ambient temperature of 23°C [6].

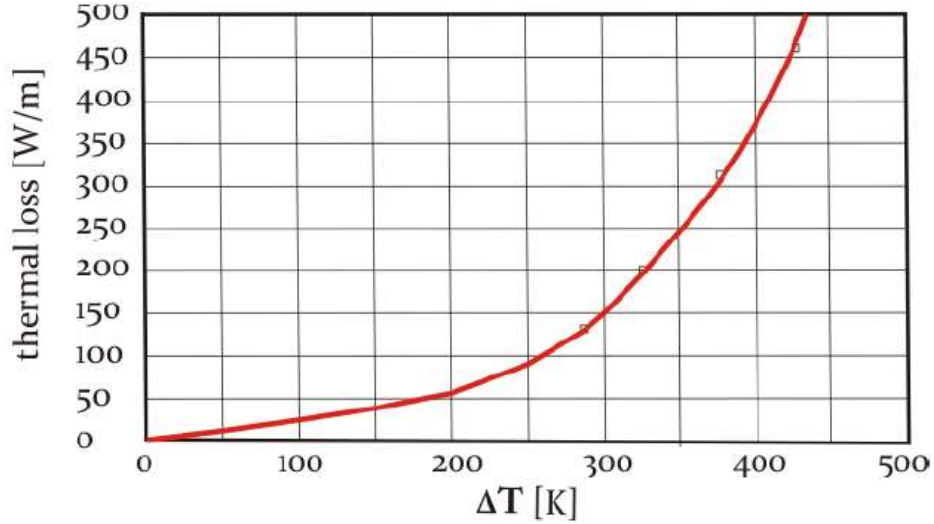


Figure 21: Correlation between T_{amb} and the receiver temperature [6].

The expression of the heat exchanged for convection can be written as:

$$Q_{conv} = Ah\Delta T \quad (1.18)$$

Where h is the heat exchange coefficient and A is the surface through which the heat transfer phenomenon occurs.

For what concerns the radiative heat exchange it is necessary to take into account the absorption of the radiation at ambient temperature and the emission that occurs at the temperature of the surface of the heat exchange element considered:

$$Q_{rad} = \alpha_{T_{amb}} \sigma A T_{amb}^4 - \varepsilon_{T_{HTE}} \sigma A T_{HTE}^4 \quad (1.19)$$

Where σ is the Boltzmann constant, T_{amb} is the temperature of the surrounding ambient and the temperature of the tube/receiver used as the element through which the heat exchange is performed.

$\alpha_{T_{amb}}$ and $\varepsilon_{T_{HTE}}$ are the mean absorptivity and emissivity for the spectrum of thermal radiation at the temperature T ; their difference, for a linear parabolic mirror, is very little: they are often considered equal, so the previous expression can be written as:

$$Q_{rad} = \varepsilon_{T_{HTE}} \sigma A (T_{amb}^4 - T_{HTE}^4) \quad (1.20)$$

In general, it is possible to say that convective losses increase as the external surface area increases, while radiative emission losses increase with the aperture area. However, even if radiative losses decrease by decreasing the aperture area, it will give as a result the increase of spillage losses. It is possible to reduce or minimize radiative losses either using a cavity receiver instead of an external one and assuring that the lower temperature region is the nearest one to the external aperture while the highest temperature one is as far as possible from the external aperture or using selective surfaces, with high solar-weighted absorptivity but low thermal-weighted emissivity. To reduce convective losses, it is possible to enclose the receiver surface with a transparent window.

1.6 Analysis of the dish concentrator system

As it can be seen from the figure, the rays entering the parabolic dish parallel to its axis, will be reflected towards the direction of the focal point: this happens thanks to the specific properties of the parabolic shape.

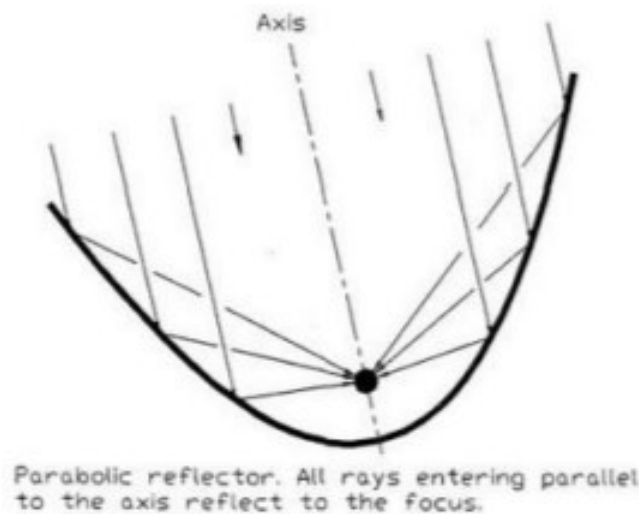


Figure 22: Dish concentration system.

In the following figure the cross section of parabolic dish can be observed; here the geometric features of the system can be studied more in detail:

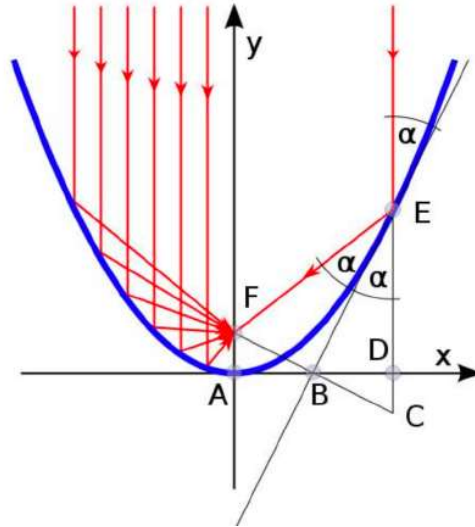


Figure 23: Cross section of parabolic dish [6].

The function that describes the parabolic shape can be written as:

$$y = px^2 = \frac{x^2}{4f} \quad (1.21)$$

From fig. 21 it is also possible to see how every ray hitting the parabolic surface with a direction parallel to its axis, will pass through the focal point. For our analysis we will be addressing the specific case of a parabolic dish that reflects all the incoming rays in a single point. This geometry can be built by rotating the 2D paraboloid around its own axis.



Figure 24: Parabolic dish collector.

The design of these structures is very complex, especially considering the compromise that has to be made between optic quality and price: imperfections and reflectivity of the mirrors has to be considered, as well as possible tracking errors. The cost of the parabolic dish collector depends on the materials of the reflecting surface, the base structure, the tracking mechanism (because of the bearing and leverage system costs) and the receiver's material. Costs are also affected by the operating condition of the conversion chain used of this system: higher operation temperatures translate to higher efficiencies of the machine, but also to higher complexity in the choice of the components that form it. Indeed, it would require optical components of higher quality increasing fabrication costs.

For what concerns the reactors, it can be either a Stirling internal combustion engine motor placed at the focal point, or they can be designed to work as chemical reactors, in which the energy coming from concentrated radiation drives thermochemical processes whose aim is to produce synthetic fuels. During our experimental work the solar energy was exploited to drive thermal dissociation processes aimed at producing molecules with high energy content and economic value. The solar concentration configuration used in our case consists of a parabolic dish collector made of aluminum and coated with a polymeric fil to guarantee a high reflectivity and, consequently, higher optic efficiency.

The parabolic dish collector used during our study has the following features:

- i. Concentrator surface of 4,5 m^2 .
- ii. Optic efficiency of 80%.
- iii. Mean direct solar radiation of 800 $\frac{W}{m^2}$
- iv. Concentrated power, at optimal conditions, can reach the value of 2,8 kW.
- v. Focal point temperatures above 1800°C.

The solar radiation is focused of an alumina (Al_2O_3) reactor (cylindrical tube). The system is composed by a double axis tracking system to maximize the exposure of the collector to the sun.

The parameters that affect the most the design of a solar dish concentrator are the diameter and reflective material of the concentrator, the sizing of the opening catchment area, the focal length, the diameter of the focal point, the geometric concentration ratio and rim angle. In the following paragraph these aspects will be shortly analyzed.

1.7 Mirror Material

The concentration of the solar radiation, required to achieve a sufficient temperature on the focus of the parabolic dish, is highly dependent on the mirror material, because they allow to have an effective reflection of the solar rays. Depending on the reflectivity of the solar concentrator, and so on the material of which it is composed, the solar radiation will reach the receiver with different efficiency: among the most used coatings it is possible to find silver, aluminum or stainless steel, with reflective coefficients that can be seen in the following table [3].

Product Name	Manufacture	Materials	Working Temp. (°C)	Reflective (%)	Emissive (%)
VM2000	3 M	Polymeric Film, Non Metal	125	98	2
SA - 85	3 M	Aluminum, Acrylic	95	98	2
ECP-305	3 M	Silver, Aluminum Acrylic	125	97	3
Acrylic Mirror	Gcip	Silver, Acrylic	100	95	5
MIRO-SUN	Alanod	Aluminum, Acrylic	98	95	5
Reflect Tech	Alanod	Aluminum, Acrylic	95	92	8
Reynolds	Alcan	Aluminum	500	86	14
Astro	Astro Aluminum	Aluminum	85	97	3
Clear Dome	Metalized Products	Aluminum, Polyethylene	100	97	3
Heat Shield I	Metalized Products	Aluminum, Polyethylene	100	97	3
Heat Shield II	Metalized Products	Aluminum, Polyethylene	100	97	3
Plexiglas	Evonic Industries	Plexiglas with Mirror	90	90	10
MirroFlex	ATI	Thermoplastic, Silver, Gold, Brass, etc.	125	80	20
Mylar	Gafix plastics	Aluminum Mylar	89	97	3
Spin Off	Metalized Products	Aluminum Polyethylene	110	97	3
IBAD	IBAD	Polymer, Copper, Silvered, Alumina	95	97	3
Kraft Paper	Ra Bar Products Inc	Aluminum	98	90	10
Roche John SA-85	3 M	Aluminum, Acrylic	95	98	2
Mirror Polished Stainless	MSS	Polished Stainless	80	50	50
CERMET	Sun Select	Ceramic Metallic Coating Layer	90	95	5

Figure 25: Reflective coefficients [3].

Generally, concentrators are composed by glass or plastic reflective plates which are superficially coated with aluminum or silver. The most performing among them are the silver mirrors mounted on a 1 mm thick glass; cheaper solutions may be aluminum or silver coated with thin polymeric reflective films. It is also possible to distinguish between thick and thin glasses: thick glass (4 mm) has typically ~1 % lower reflectivity than thin one.

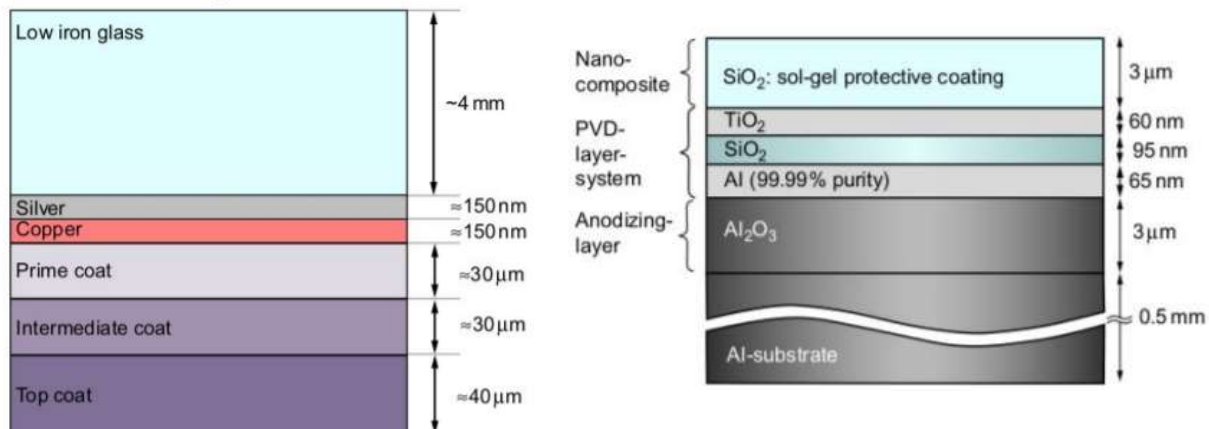


Figure 26: Standard thick-glass mirror (left) and silver mirror (right)

Thin glass needs to be supported on a substrate; thick glass can potentially be self-supporting. It was proven by several studies that by adding a certain amount of iron the reflectivity of the mirrors would be improved; for instance, silver reflectors on iron enriched glass layers have a solar reflectance of 90-94%, which depends on the thickness and iron content. The reflectance

provides a measure of the amount of solar radiation lost during the reflection process, through the following expression:

$$Q_{in} = CG\rho \quad (1.22)$$

Where:

- C is the concentration ratio
- G is the solar irradiance
- ρ is the reflectivity coefficient of the concentrator

1.8 Design of the opening area of the concentrator

This surface depends on the power required, in our case, for the chemical reaction to happen. It is possible to define the opening area of the dish as the total surface area of the concentrator affected by solar energy or, as the area receiving the radiation. The formula can be written as:

$$A_{conc} = \frac{\pi}{4} D_{conc}^2 \quad (1.23)$$

1.9 Rim angle

The rim angle (Φ_{rim}) plays a fundamental role as it is an indicator of the curvature of the paraboloid and is always measured near the geometric focus of the system. The rim angle represents the angular width formed between the joining line the focal point with the outer edge of the paraboloid and the optical axis of the concentrator. It can be demonstrated that the rim

angle is equal to the ratio between the focal length and the opening diameter of the concentrator; furthermore, it can be seen that values of the rim angle equal to 45° give the possibility to reach high values of the concentration ratio, which translates to the maximization of the thermal power. It is possible to show the rim angle through the following scheme:

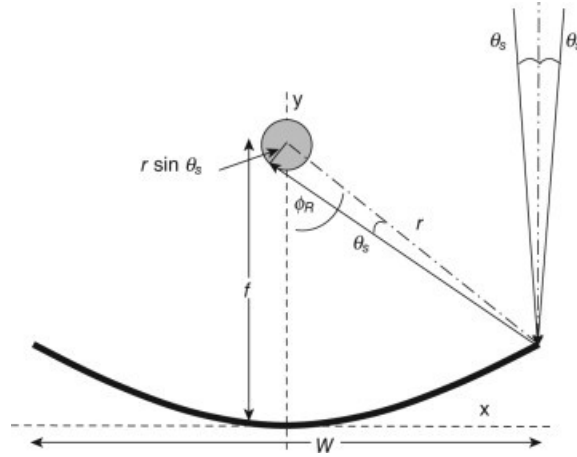


Figure 27: Rim angle.

It can also be expressed through the formula:

$$\Phi_{rim} = \frac{W/2}{4f - R^2} \quad (1.24)$$

1.10 Length of the focal point

The focal length f is defined as the distance between the edge and the focal point if the parabolic dish.

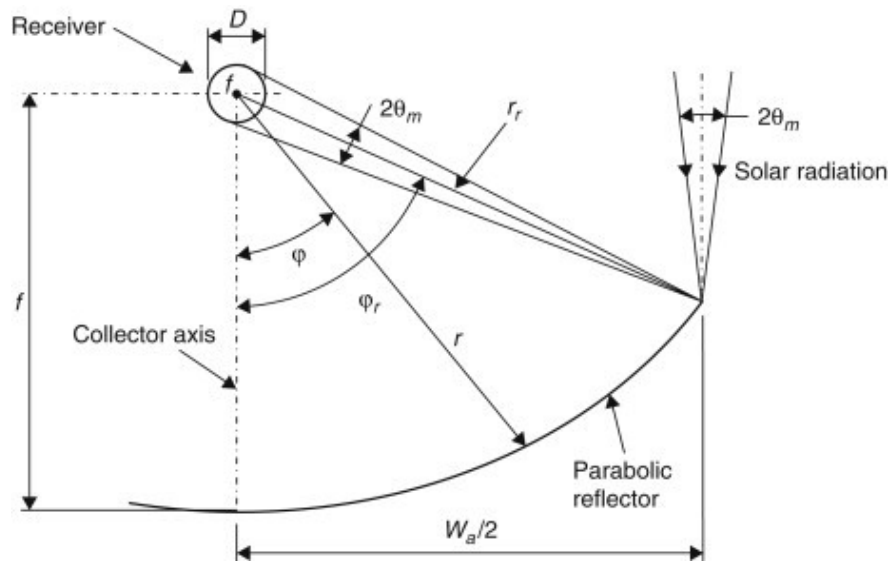


Figure 28: Focal point.

Focal length and depth of the paraboloid can be calculated as:

$$f = \frac{D_{conc}}{4 \tan\left(\frac{\Phi_{rim}}{2}\right)} \quad (1.25)$$

$$h = \frac{D^2_{conc}}{16f} \quad (1.26)$$

It is also important to calculate the diameter of the focal point:

$$d_{focal\ point} = \frac{f\theta}{\cos\Phi_{rim}(1 + \cos\Phi_{rim})} \quad (1.27)$$

1.11 Solar tracking system

Like any solar concentration system, for a parabolic reflector there is the need for a tracking system of the Sun in a continuous way, in order to concentrate its radiation. The latter, in fact, continuously changes direction with respect to the horizontal coordinate system of a position date and, consequently, relative to the optical system fixed on the surface terrestrial. Since the sun's rays must enter the collection system with a precise direction, because concentration system works only with direct radiation and not with diffuse one, it is essential to keep the mirrors in line with the incident radiation. Point concentration systems, such as paraboloid and solar tower, require a high precision two-axis tracking system, while for systems it is sufficient to achieve the pursuit on a single axis.

Since we are working with a two axis tracking system it is necessary to focus the attention on the zenith angle, that indicates the inclination of the concentrator compared to the vertical (in other words it is the angle between the direction of the optical axis of the concentrator and the vertical direction of the zenith), and must be kept equal to 0 in order to guarantee the proper tracking of the solar radiation, and the azimuth angle, which indicates the angular displacement from the south of the projection of the solar beam in the horizontal plane.

There are three main methods for solar tracking:

- the active tracking method is based on the calculation of the altitude angle and solar azimuth by an exact mathematical algorithm integrated with a preset program. The optical axis of the collector is compared with the solar position and the possible angular difference is eliminated by the drive. The automatic system can determine the position of the Sun provided that latitude/longitude and date/hour information are given as input. The positive feature of this method is that it's not affected by external factors such as clouds, dust; however it's less precise.
- the passive tracking method, is based on optical sensors or devices that detect the deflection of incident light and send an electrical signal to the panel which will activate the electric or hydraulic cylinders. This ensures that the surface capturing follows the apparent movement of the Sun. Using such a system is not only economic but also efficient, although effectiveness decreases if the sensor is obscured by clouds
- to improve the overall efficiency, it is possible to adopt a hybrid method that combines active and passive tracking methods.

1.12 Reactors Materials

1.12.1 Alumina

The first two tests were performed using alumina (Al_2O_3) as the reactor material. This material is a ceramic and is generally characterized by high densities, between $3.75 - 3.85 \text{ g/cm}^3$ and high sintering temperatures of manufacturing (around $1500-1900^\circ\text{C}$).

In the following table the main thermal properties of alumina can be analyzed:

Table 2: Thermal properties of alumina [7].

Thermal expansion coefficient 10^{-6} 1/K	Specific heat J/gK	Thermal conductivity W/mK
5.4	0.775	25 - 35

The main mechanical properties of alumina can be listed in the following table:

Table 3: Mechanical properties [7].

Al ₂ O ₃ /Porosity %	Young's modulus GPa	Shear modulus GPa	Poisson's ratio
$\geq 99.6 / 3 - 6$	380 - 340	150 - 140	0.26 - 0.24

These values are reasonably valid in a certain range of operating temperature: for E up to about $750 - 1000^\circ\text{C}$, for G up to $650 - 800^\circ\text{C}$ and for ν up to about $650 - 700^\circ\text{C}$. However, for materials specifically designed to work at high temperatures, these upper boundary limits increase; beyond these limits the nonlinearity increases, as it can be seen in the following picture:

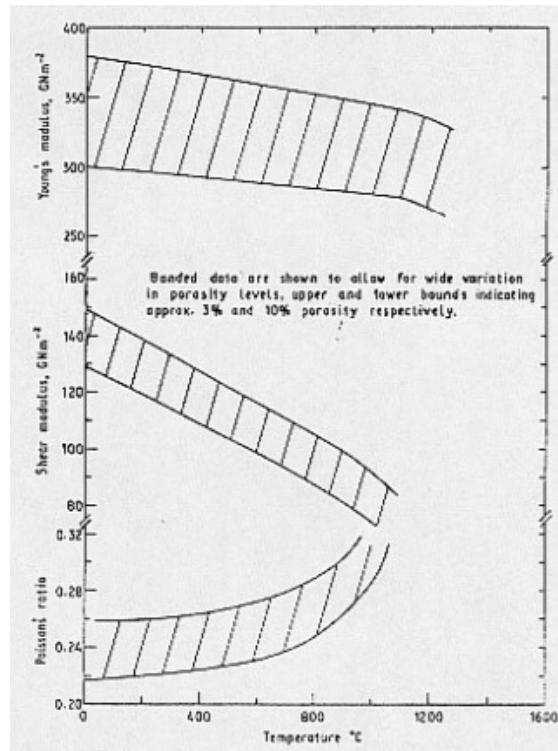


Figure 29: Temperature dependence of Young's modulus, shear modulus and Poisson ratio for alumina [7].

Testing standards for ceramic are not particularly effective, as they provide a limited picture of the total material characteristics. In most of the engineering applications of alumina the viscoplastic behaviour of the material is negligible, and the ceramic can be considered only in its elastic field (approximation that is valid in for temperatures up to 900-1000°C). Other mechanical properties are:

Table 4: Mechanical properties of alumina at ambient temperature for specimens with a cross-sectional effective diameter of 3 - 15 mm.

Avg. flexural/compressive strength MPa	Weibull modulus m	Fracture toughness MPa√m	Hardness HV1.0
150-450 / >4000	na	4.5 - 4.9	na

It can be noted that by increasing the dimensions of the specimen average strength, fracture toughness and hardness tend to increase. Being a ceramic material, the strength of alumina is

not a specific quantity but a statistical one with a relatively wide scatter (which depends on the Weibull modulus) because of the low toughness and high dependence on small pre-existing defects. The compression strength of alumina is much higher than the tension one. Fracture toughness of alumina is really temperature dependent, in particular it decreases greatly for temperature values higher than 1000°C:

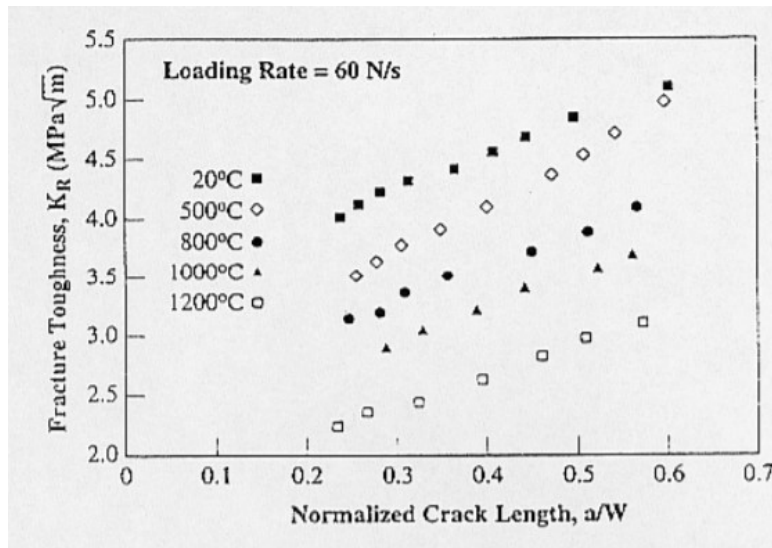


Figure 30: Fracture toughness trend of alumina with temperature.

Creep behavior of alumina becomes interesting to study for very high temperatures ($>1000^\circ\text{C}$). The threshold temperatures vary from about 800 - 1000°C for alumina with mechanical/electrical/insulation applications in long-term use under load, to 1700 - 1900°C for refractory alumina in short-term unstressed use.

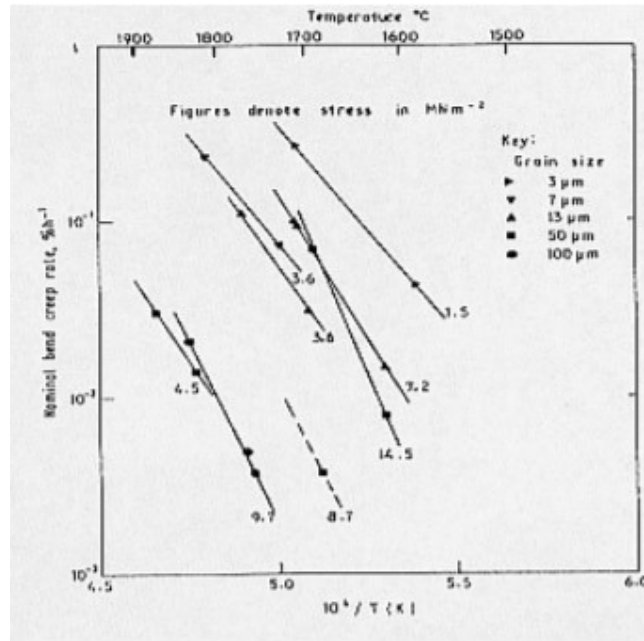


Figure 31: Creep behavior of alumina of the refractory type.

The most interesting behavior of alumina for this study concerns the thermal shock resistance R , which is defined as “*maximum change in temperature that the component can withstand without failure*” [7]. The main characteristics that affect the thermal shock resistance of ceramic materials are:

- type of thermal cycle
- component geometry and strength
- elasticity
- thermal conductivity
- thermal expansion characteristics

Under the assumption that the material will fail if the rate of change of the temperature on the surface is changing at such a rate ϕ that the resulting biaxial surface stress equals the material strength σ_s , the following expression of the thermal shock resistance can be written:

$$\phi = \frac{\sigma_s(1 - \nu)D(\text{shape factor})}{E\alpha} = R_0(\text{shape factor}) \quad (1.28)$$

Where D is the thermal diffusivity and R_0 is a thermal shock resistance parameter for components with similar geometry. For higher grades of alumina this value is higher, as it can be seen from the table:

Table 5: Thermal shock resistance for alumina for quenching from 200°C to room temperature.

α 1/K	E GPa	P g/cm^3	λ W/mK	R_0 $10^{-4}m^2K/s$
5.43	410 - 340	.75 - 3.95	30 - 40	10 ± 4

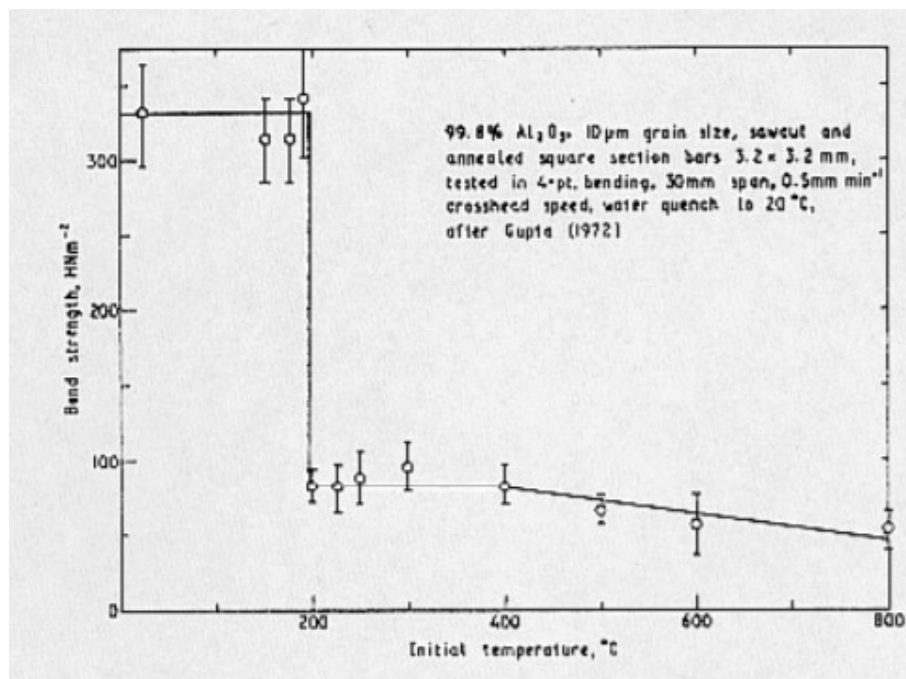


Figure 32: Temperature dependence of residual strength after single quenching of alumina [7].

1.12.2 Hastelloy

The choice of using a Nickel-based alloy was necessary to face the high temperatures that could be found on the surface of the reactor corresponding to the focal point. These materials are heat-resistant and have superior mechanical/chemical properties at high temperatures, high melting temperatures, enhanced corrosion resistance/thermal fatigue. The manufacturing of these materials is more complex than other materials and they have low workability. The properties

of the material vary according to the manufacturing processes and temperatures. Romedenne et. Al [8] studied the oxidation of three types of hastenalloys: two manufactured with Electron Beam Melting (EBM) technology with different Si and Mn contents (named as EBM1 and EBM2) and the other fabricated with the Selective Laser Melting technology (named as SLM). They were compared also with commercial piece manufactured by Haynes International. In order to reduce residual porosity, after fabrication the rods underwent a Hot Isostatic Press (HIP) at 150MPa for 2h at 1176°C and were then quenched. EBM specimen used in the test had diameter=15mm and thickness=1.5mm, while for the SLM type the specimen was had a square cross-section of with length=13mm, width=13mm and thickness=1.5mm. For what concerns the tests the heating process were conducted for 8 and 72h at 950°C. The heating rate in was 40°C/min for the temperature range of 25-650°C to 40°C/min and then 20°C/min from 650 to 950°C with 2h cooling at the end of the test. The tests were performed in an air environment, with a flow equal to 36cc/min. The change in mass that followed the oxidation process can be seen in the following picture:

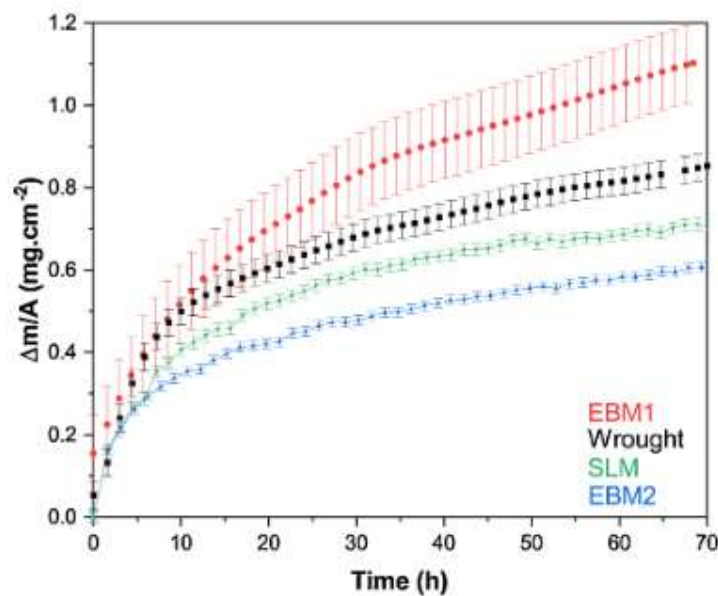


Figure 33: Mass change as function of time during isothermal oxidation at 950°C for 72h [8].

It's possible to find many typologies of hastelloys with different characteristics: Hastelloy-X, with a chemical composition of Cr-22wt%, Fe-18wt%, Mo-9wt%, and Co-1.5wt%, is suitable for high temperature environments, such as the combustion chamber of gas turbines where the temperature can get as high as 1100°C for several thousand hours [9].

The physical properties of Hastelloy X manufactured by Haynes International can be found in the following table:

Table 6: Dynamic Modulus of Elasticity [14].

Dynamic Modulus of Elasticity Gpa	RT	205
	500°C	180
	600°C	173
	700°C	165
	800°C	157
	900°C	148

Table 7: Properties of Hastelloy X.

Density	Thermal Conductivity	Specific Heat	Mean Coefficient of Thermal Expansion	Melting Range
8.22 g/cm ³ at 22°C	9.22-26.7 W/m°C in the range RT-900°C	486-784 J/kg°C in the range RT-900°C	16.6 10 ⁻⁶ m/m°C in the range 26-900°C	1260-1355 °C

In the following table it can be seen the oxidation phenomena:

Table 8: Static Oxidation Data in Flowing Air for 1008 Hours.

Alloy	1095°C			
	Metal Loss/Side		Metal Loss + CIP**/Side	
-	mils	mm	mils	mm
X	1.5	0.038	2.7	0.069

CIP: Continuous Internal Penetration

Other hastelloy compositions can be used not only for high operating temperature but also for cryogenic conditions, such as the hastelloy C-276 [10].

Very often hastelloy is found as substrate for $YBa_2Cu_3O_x$ (YBCO); according to the type of deposition technique used, the material can undergo different atmospheres with temperatures up to 800°C. This would lead to an oxidation process of the alloy. This can happen for long term exposure, being hastelloys more resistant to oxidizing environment. The formation of dense layers may be beneficial for the structure of a coated YBCO conductor. Previous studies showed that the oxide that formed on Hastelloy C after 10,000 h in air at 1000°C were formed by an inner layer of Cr_2O_3 and an outer layer of Mn-rich spinel. In the oxidation process the specimen of 1-1,5 cm^2 surface and 0,4mm of thickness, underwent temperatures ranging between 300-800°C and partial pressures of oxygen ranging from 0,01-100%/balanced Ar. These tests show the following mass-growth trends [11]:

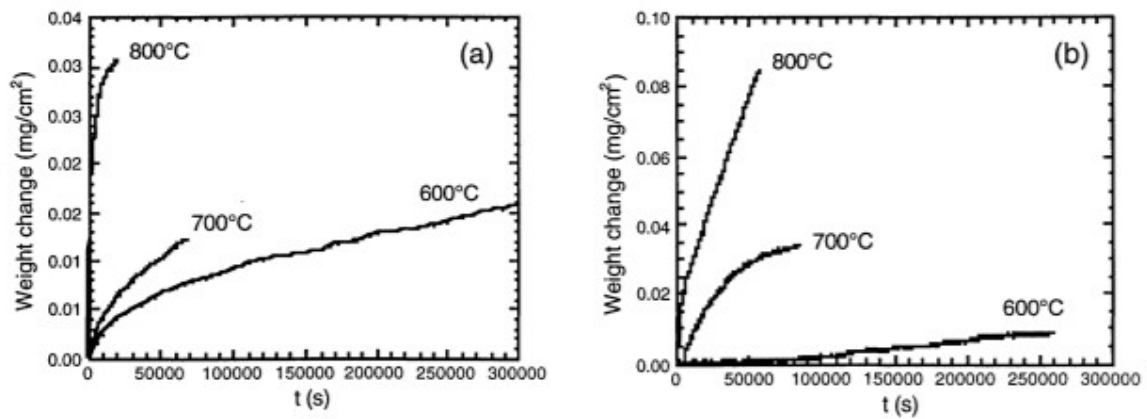


Figure 34: Weight gain vs. time for oxidation of Hastelloy C276 in (a) 0.01% and (b) 100% oxygen environment [11].

1.12.3 Inconel

Inconel alloys are part of the Ni–Cr based superalloys family that are designed to cover a wide range of compositions and mechanical properties. Ni and Cr allow components to have resistance to corrosion, oxidation, carburizing and other damage mechanism that can be found especially at high temperature. At moderate temperatures these alloys have good cryogenic properties, fatigue, and mechanical strength while for relatively high temperatures they have good creep behavior. Usually, Inconel alloys are extra-alloyed with Al, Ti, Nb, Co, Cu and W to increase mechanical and corrosion resistance [12]. It can also be possible to find Fe in amounts ranging 1–20%. Their application can be for heat treatment recipients, turbines, aviation, nuclear power plants, and so on. According to the composition it can be possible to find various typologies of Inconel, such as the Inconel 718:

Table 9: Inconel 718 composition [12].

Al	0.52
C	0.021
Co	0.11
Cr	19.06
Cu	0.02
Fe	18.15
Mo	3.04
Ti	0.93
Nb	5.08
Ni	53.0

The strain of this superalloy, depending on the temperature, can be seen in the following figure:

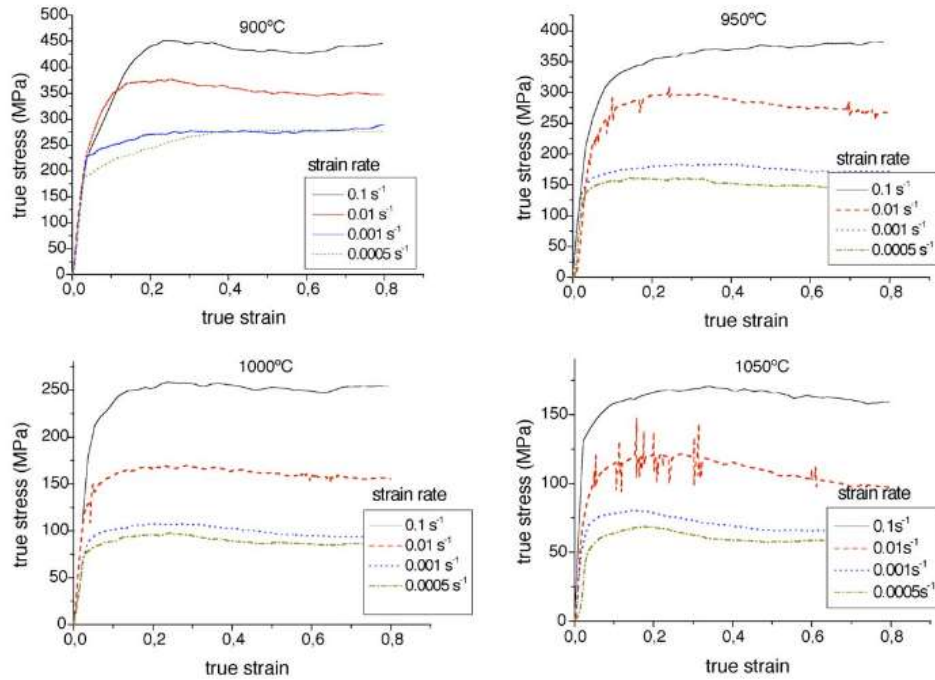


Figure 35: Flow curves for the current Inconel 718 at different temperature and strain rates [12].

In E. Chlebus' study, cylindrical specimens with diameter of 4 mm and gauge length 19 mm underwent tensile stress while oriented in different directions, in order to calculate the material's mechanical properties; the testing results and the scheme of the specimens can be seen in the following:

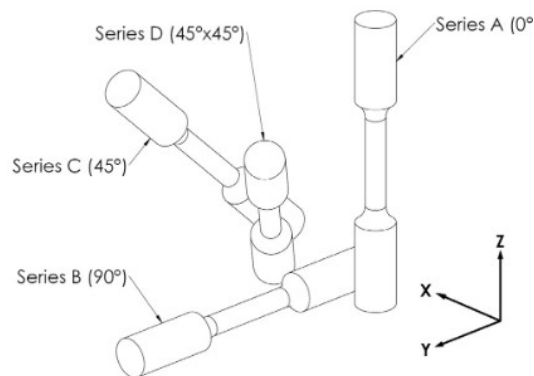


Figure 36: Tensile specimens A,B,C and D [13].

Properties	Series			
	A	B	C	D
Young's modulus, E [GPa]	162 ± 18	193 ± 24	200 ± 23	208 ± 48
Yield strength, $\sigma_{0.2}$ [MPa]	572 ± 44	643 ± 63	590 ± 15	723 ± 55
Tensile strength, σ_t [MPa]	904 ± 22	991 ± 62	954 ± 10	1117 ± 45
Elongation at fracture, ϵ_f [%]	19 ± 4	13 ± 6	20 ± 1	16 ± 3
Hardness HV1	xy-plane: 297 ± 5; xz-plane: 319 ± 10; yz-plane: 322 ± 10			

Figure 37: Mechanical properties [13].

In the following picture it is possible to see the elongation, the tensile strength and yield strength varying with temperature:

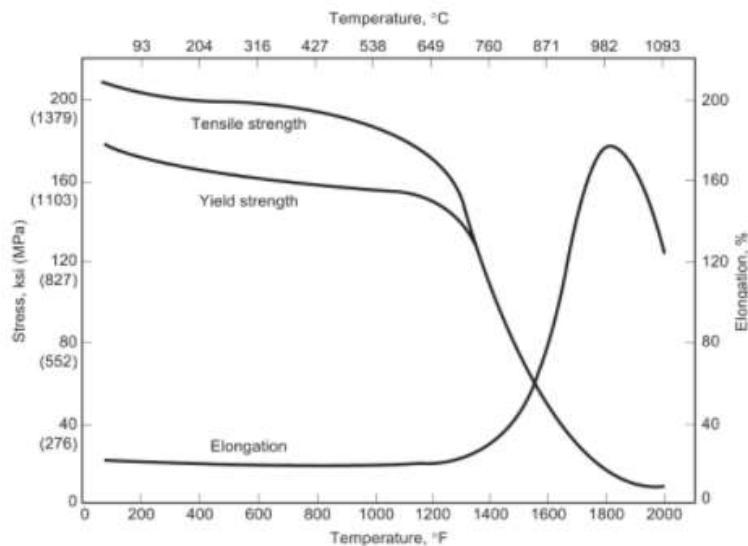


Figure 38: Tensile strength, yield strength and elongation vs. temperature .

Another type of Inconel commercially available are the Inconel 686, which has the following properties at room temperature:

Product form	Thickness or diameter		Tensile strength		Yield strength (0.2% offset)		Elongation, %
	mm	in.	MPa	ksi	MPa	ksi	
Plate	12.7	0.500	722	104.7	364	52.8	71
	6.35	0.250	733	106.3	399	57.9	68
Sheet	3.18	0.125	803	116.5	421	61.1	59
	1.57	0.062	848	123.0	408	59.2	59
Rod	38.1	1.50	810	117.5	359	52.1	56

Figure 39: Room temperatures of Inconel 686.

Increasing the temperature, the change in these properties can be seen:

Temperature		Yield strength		Tensile strength		Elongation, %
°C	°F	MPa	ksi	MPa	ksi	
24	75	396	57.5	740	107.3	60
93	200	323	46.8	691	100.2	69
204	400	290	42.1	635	92.1	67
316	600	288	41.7	602	87.3	60
427	800	224	32.5	570	82.6	69
538	1000	261	37.9	545	79.1	61

Figure 40: Mechanical properties with temperature.

Temperature, °C	Elastic modulus, GPa	Shear modulus, GPa	Poisson's ratio
20	207	77	0.34
100	205	75	0.37
200	197	72	0.37
300	193	70	0.38
400	185	69	0.34
500	183	67	0.37
600	173	65	0.33
700	165	61	0.35

Figure 41: Elastic modulus and Poisson's modulus for Inconel 686.

Other Inconel typologies can be found in literature, such as Inconel 600, 625 [14], 622.

Chapter 2

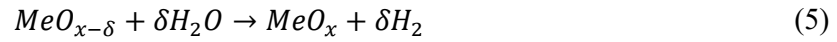
2 Literature Review

2.1 Thermochemical Cycles

Thermochemical cycles of water splitting are proposed for the production of hydrogen and oxygen starting from water. Theoretically, the easiest way to achieve this would be through a single step reaction; however, it would require very high temperatures (around 2500 K) and would also imply hazards related to the non-perfect separation of H_2 and O_2 , with risks of explosion. Chemical looping processes are therefore considered as a consistent pathway for the realization of such reactions. It consists of a series of consecutive chemical reactions in the form of a closed cycle, and it aims at producing a high value chemical (syngas or hydrogen) starting from a less valuable chemical. Considering in particular the two-step water splitting process, the maximum temperatures of the process remain lower than that of the one step reaction. However, the energy demand for these processes remains consistent; to provide this high temperature heat it is possible to exploit solar concentrator systems. The most common chemical looping processes imply the production of liquid fuels, such as H_2 through H_2O splitting, from the decarbonization of fuel mixtures or the CO_2 capture and following conversion into syngas. The chemical looping process exploits metal material that present multiple oxidation states which will be subjected to a redox reaction in the form of metal oxides Me_xO_y . The reaction occurs through the transition between the oxidized form and the reduced form of the metal oxide. In the first step of the process the metal oxide goes through a reduction reaction, which is driven by a high temperature heat source (concentrated solar radiation in our case): the external energy induces the material to release oxygen molecules and therefore transform into a lower valence metal oxide. In the second step the reduced metal oxide is oxidated to its original form through a reaction in which oxygen will be taken from water molecules, producing hydrogen. The general chemical formula for the reduction reaction is:



Then according to the desired result, it is possible to have a water splitting or a CO_2 splitting in the oxidation reaction:



In these types of reactions, a key role is played by the oxygen carrier and its capability of gaining different oxidation states in order to release or acquire oxygen molecules. Many materials can be used as oxygen carriers. Among them, the most important are ceria oxides [15], in which it can be seen that oxygen release from the oxygen carrier occurs starting from 1200K and above, Cu-based, Fe-based, Mn-based [16] and perovskite based [17]. A further classification between volatile and non-volatile cycles can be done, which depends on whether the metal oxides keep their solid state during the process, or they evaporate.

2.1.1 Volatile Oxygen Carriers

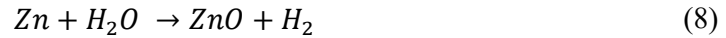
Zinc, Cadmium, Germanium and Tin Oxides are amongst the most common volatile oxygen carriers. Under high temperature conditions these materials undergo a solid-to-gas transition. This phenomenon occurs because temperatures required for chemical looping can reach high values, even larger than the boiling temperature of the non-oxygen materials employed. This is what happens in the reduction reaction for the redox pair ZnO/Zn, in which the solid-gaseous transition by all chemical species other than oxygen occurs.

Although this transition may appear favorable from an entropy point of view, it has a disadvantage related to the recombination of products of dissociation with oxygen to form the

initial reagent, or oxidized metal, in the gas stream produced; therefore, the main drawback of volatile cycles is the recombination of the decomposition products back to the oxidized state of the oxide. Analysing more in detail the ZnO/Zn , one of the most common volatile redox pair, it can be seen that it is characterized by many attractive features, such as the low atomic weight and therefore high energy content per mass (factor that makes this pair an interesting energy vector) [18]. However, the thermal reduction decomposition of this oxygen carrier occurs at temperatures around 2300 K; through thermogravimetric (TGA) experiments it was possible to observe that the dissociation of ZnO to Zn(g) and oxygen starts around 1273 K, which is the evaporating point of zinc [19]. ZnO can be exploited for the production of hydrogen through water splitting reaction, as well as CO from CO_2 splitting. In the following the reaction of ZnO reduction can be observed:



And, according to the chemical species used in the oxidation step, it is possible to have, as final product, hydrogen or carbon monoxide:



Many experimental studies, such as the one led by Levêqu et al.[20], analyzed the utilization of volatile cycles (ZnO, MgO, SnO₂ and GeO₂) for chemical looping application exploiting concentrated solar energy. Here are shown the main results for a solar reactor with $I=1kW/m^2$ and $C=5000$:

	Temperature	Reaction	ΔH° (kJ mol ⁻¹)	$\eta_{\text{Solar to fuel}}$
MgO	3440 °C	$\text{MgO} \rightarrow \text{Mg(g)} + 0.5 \text{O}_2$	603	–
ZnO	2070 °C	$\text{ZnO} \rightarrow \text{Zn(g)} + 0.5 \text{O}_2$	378	29% (@ 2000 °C)
SnO ₂	2060 °C	$\text{SnO}_2 \rightarrow \text{SnO(g)} + 0.5 \text{O}_2$	519	29.8% (@ 1600 °C)
GeO ₂	1830 °C	$\text{GeO}_2 \rightarrow \text{GeO(g)} + 0.5 \text{O}_2$	469	34.6% (@ 1500 °C)

Figure 42: Thermodynamic data for thermal reduction.

2.1.2 Non-volatile Oxygen Carriers

The non-volatile cycle exploit metal oxide that doesn't go through the phase transition during the chemical looping process, avoiding the recombination problem [21]. The most common non-volatile cycles for water splitting/carbon dioxide splitting involve oxygen carriers such as iron oxide, ceria, hercynite and perovskite. They stay solid through the reduction process and require lower endothermicity, which translates to a lower temperature of the reduction step. The main drawback of the non-volatile cycles is they non-stoichiometric conditions of the redox reaction. This translates to a lower oxygen storage capacity compared to the volatile counterpart.

Ferrite can be utilized both for water splitting/carbon dioxide splitting both separately or at the same time. The range of temperatures at which the reaction of reduction of ferrites occur is still high, in the order of 1600-1700 K [22]. The two steps of the reaction that occurs during the chemical looping are listed below:



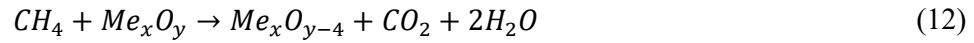
An important limitation related to iron oxide oxygen carriers is the fact that they can withstand a limited number of cycles, after which the reactivity of the material decays, due to accumulative chemical and thermal stresses [23]. Furthermore, the temperatures are relatively lower if compared to volatile cycles but are still very high.

2.2 Chemical Looping Combustion

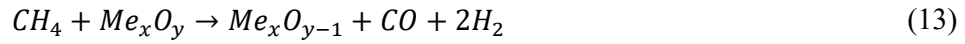
In the following section the study of the thermochemical cycles will be addressed. In particular, the attention will be focused on chemical looping processes that exploit iron oxides as oxygen carriers.

Chemical looping with methane as a reducing agent, also called Chemical Looping Combustion (CLC), is a process in which the partial oxidation of CH₄ occurs, where oxygen carriers are used as a source of undiluted oxygen; the results of this reaction will be high value chemicals. In the first step of the reaction, methane is decomposed using an oxygen carrier to form hydrogen atoms and carbon atoms. Then, hydrogen atoms recombine to produce H₂ or are oxidized by oxygen to generate H₂O; in the meantime, carbon atoms are oxidized by O to produce CO or

CO₂. The oxygen carrier (expressed in the generic for as Me_xO_y) is reduced by the following general reaction:



or



For what concerns the oxidation reaction, O is taken from the atmosphere to regenerate the reduced metal oxide, as it can be seen in the next formulas:



Or



These reactions can be summarized with the following scheme:

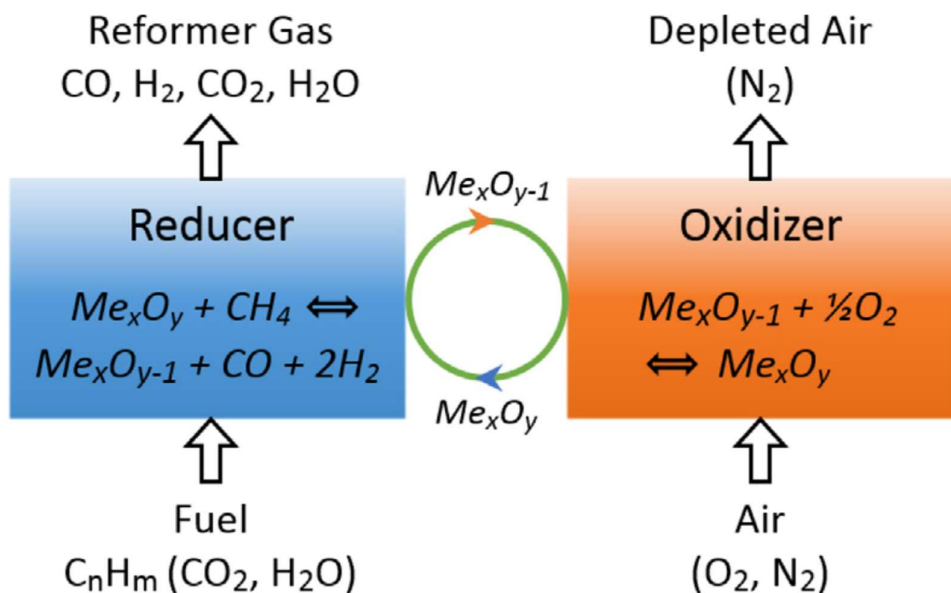


Figure 43: Basic principles of CH₄ chemical-looping reforming [24].

The resulting gas from the reduction reactor can contain a gas mixture of CH₄, CO₂, CO, H₂O and H₂. By properly selecting the oxygen carriers and dosing the relative amount of carbon (contained in the fuel) and oxygen (in the oxygen carrier) in the reduction reactor, it is possible to achieve a selective generation of syngas. This means that the oxygen carrier has to be properly selected in order to have high activity, selectivity and redox stability for the fuel (methane in our case). Many are the material proposed as metal oxides with the purpose of transporting oxygen, such as Ni, Cu, Fe, Co, and Mn. To improve the structure, dispersion, durability and oxygen mobility of oxygen carriers, they are commonly found in combination with various support materials, such as Al₂O₃, SiO₂, TiO₂ and CeO₂. Among these many options, Fe-based oxygen carriers are considered to be the most promising candidate for the chemical looping of methane application, because of its easy handling, nontoxicity, and environmental-friendly features, which are unique advantages. Their main advantage is the high thermal stability, which makes them suitable for chemical looping processes. Iron oxides present also some important drawbacks, such as the relative low oxygen transfer capacity and the weak redox properties, as well as the low reactivity toward CH₄. Even if iron has four intermediate states (Fe₂O₃, Fe₃O₄, FeO, and Fe), the state transition able to perform the oxidation of CH₄ to CO₂ in the most complete way is Fe₂O₃ to Fe₃O₄, as it can be seen in the following [25]:

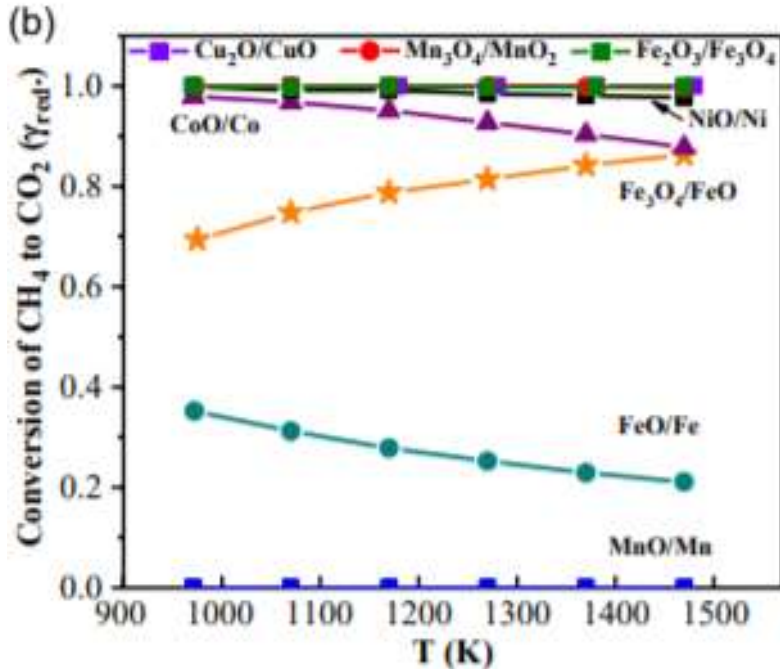


Figure 44: Conversion of CH₄ to CO₂ as a function of temperature for different oxygen carriers [25].

It is possible to say from literature research that the iron oxide reduction performed with the use of methane requires an activation energy that can vary from 49 to 271 kJ/mol [24]. As it can be seen from Ghosh studies [26] the reduction of iron oxide (Fe₂O₃) with 100% methane at the temperature of 800–1025 °C, the apparent activation energy was obtained as 206 kJ/mol in the temperature range of 800–950 °C, while between 950–1025°C it is equal to 105.7 kJ/mol. In another study proposed by Monazam the reduction of hematite in methane atmosphere was carried out in the range of 700–825 °C with CH₄ concentrations that varied between 15%, 20%, and 35% in N₂ mixture.

Here, the majority of the CH₄ was totally oxidized, turning into CO₂ and H₂O at the early stages of the reduction process. As the reaction proceeded, a minor amount of CO and H₂ were released due to partial oxidation of some CH₄.

In the following paragraph some examples of chemical looping processes found in literature will be shown and analyzed.

2.3 Methane aided chemical looping reaction

In many studies, such as the one led by Chunqiang Lu [27], the chemical looping process of methane using magnetite (Fe_3O_4) as oxygen carrier was analyzed. The redox experimental procedure can be divided in several steps:

- the samples were reduced by methane (10% CH₄-90% N₂, 250 mL/min) for 60 min at 1223 K
- a gas flow of N₂ was introduced for 20 min before sending in the oxidizing gases on order to purge the reaction site
- a mixture of water vapor steam and N₂ was sent in the reaction site for 55 minutes at the temperature of 1123K in order to have the oxidation reaction

Before testing, the magnetite is crushed and sieved to the desired sizes (20–200 μm). Then it was dried at 383 K for 24 h and then calcinated under ambient air at 1273 K for 2 h. The mass loss of magnetite during the reduction process will be analyzed under different isothermal condition: temperature of 1223, 1248, 1273 and 1298 K. Six redox (CH₄ reduction/ H₂O oxidation) cycles were performed to obtain a stable state before kinetic analysis. The samples were placed in a high purity alumina crucible; the heat source is a furnace that brought the oxygen carrier from ambient temperature to the reaction temperatures with a heating rate of 10 °C/min under an inert gas flow of pure N₂. When the desired temperature was reached, a flow of CH₄ (90% N₂ + 10% CH₄) was introduced into the furnace. The reducing gas flow rate was equal to 150 mL/min while the sample weight was of 300 mg and the sample particle size of 380–830 μm. The kinetics of magnetite reduction process was determined by observing the weight loss of the specimen during its transformation under the mentioned isothermal conditions.

Considering the different oxidation states of the oxygen carrier ($Fe_2O_3 \rightarrow Fe_3O_4 \rightarrow FeO$), it is possible to calculate the theoretical weight loss using the stoichiometry of the reactions



In the first reaction, the complete reduction of hematite to FeO corresponds to a 10% decrease of the initial sample weight, and a complete reduction of Fe₂O₃ to metallic Fe results in a 30% weight decrease[27]. The weight difference of the Fe₂O₃ reduction to FeO accounts for 33.33%

of Fe₂O₃ complete reduction. From the second reaction it is possible to see that the complete reduction of Fe₃O₄ to FeO corresponds to a 6.90 wt% decrease of the initial sample weight, while the complete reduction of magnetite to metallic Fe corresponds to a 27.57 wt% weight loss. Here the difference in weight from Fe₃O₄ to FeO is equal to 25% of the total reduction. During this experiment two types of magnetite were investigated: the original one and the calcinated one (pretreated at 1273 K for 2 h to improve its stability). Their main properties can be seen in the following figure:

Samples	S (cm ³ /g)	φ	τ (× 10 ¹⁴)	K (× 10 ³)
Original magnetite	0.89	0.031	1.95	2.10
Calcinated magnetite	2.18	0.016	2.70	0.20

Figure 45: Specific surface area, porosity, tortuosity and diffusion coefficient [27].

It is also possible to see the different composition of the two magnetites:

Sample	Fe (wt%)	O (wt%)	Ti (wt%)	Mg (wt%)	Al (wt%)	Si (wt%)	V (wt%)	Mn (wt%)
Original magnetite	44.14	38.50	5.31	4.40	1.77	1.85	0.35	0.29
Calcined magnetite	44.95	40.15	5.00	3.70	1.53	1.79	0.33	0.26

Figure 46: Composition of original and calcinated magnetite [27].

In the following figure the evolution of H₂, CO₂ and CO during the isothermal reduction (1223 K) reaction of the original magnetite with methane can be analyzed:

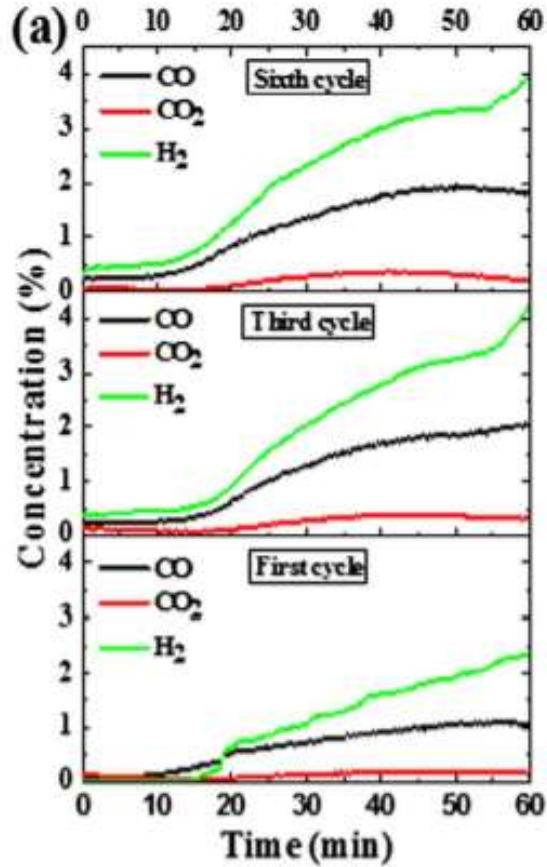


Figure 47: evolution of H_2 , CO_2 and CO during the isothermal reduction reaction at 1223 K (original magnetite) [27].

It is evident that in the first 10 minutes of the reduction reaction the concentrations are very low; however, after that time, the concentrations of CO and H_2 start increasing. This delay can be due to the dense structure of magnetite that generates these long induction times. It can also be seen that, until the last stages of the reaction, the concentration of hydrogen almost doubles the one of the CO . The concentrations of CO_2 are low during all the cycles duration. This indicates that the methane is selectively oxidized by the magnetite to CO and H_2 with a H_2/CO ratio of about 2.0 [27]. In the end of the reaction, the further increase in the H_2 concentration suggests the occurrence of methane decomposition.

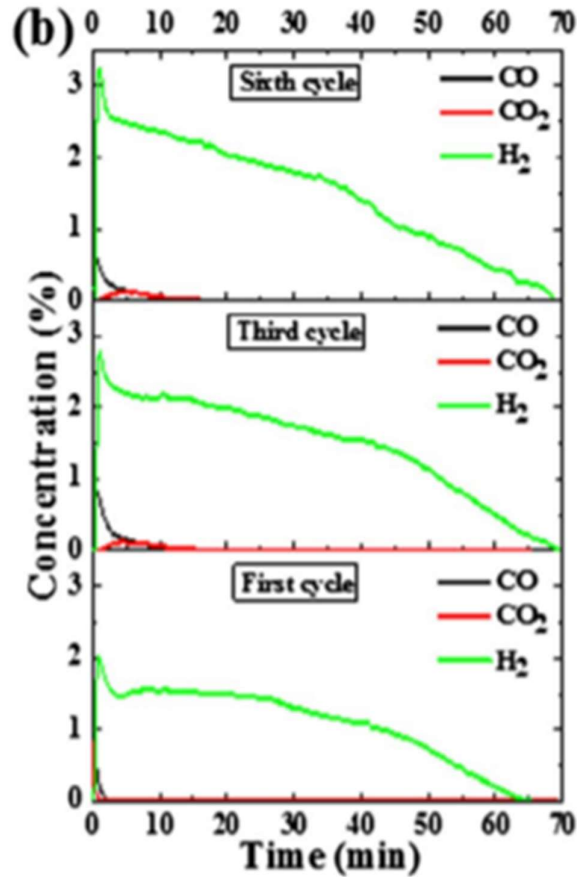


Figure 48: Evolution of H₂, CO₂ and CO during the isothermal oxidation reaction at 1223 K (original magnetite).

For what concerns the oxidation reaction CO and CO₂ are also detected; this is related to the formation of carbon deposition. During this process it is possible to see that the production of CO and CO₂ fall sharply, while the production of hydrogen lasts for around 55 minutes. From the next figure it is also possible to see that can be seen that both the yields of the syngas in the reduction step and of the hydrogen in the water oxidation step change during the first three redox cycles, and then they reach a stable state the final yield of syngas if equal to 10.29 mmol/g (the total yield of CO and H₂) and purity of 95.11% while hydrogen's one is 4.94 mmol/g and purity of 96.22%.

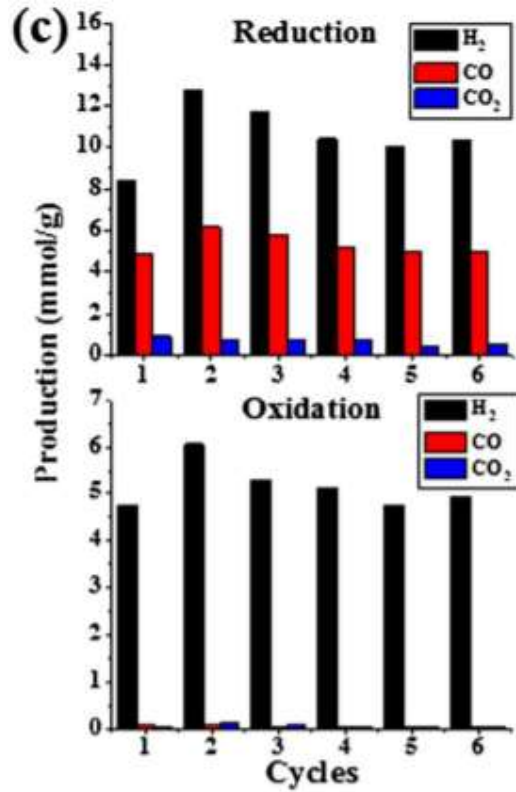


Figure 49: Oxidation and reduction step for original magnetite [27].

For what concerns the calcinated magnetite it can be seen that the trends of H₂, CO and CO₂ are similar to the one of the original magnetite; it also stabilized itself after three redox cycle.

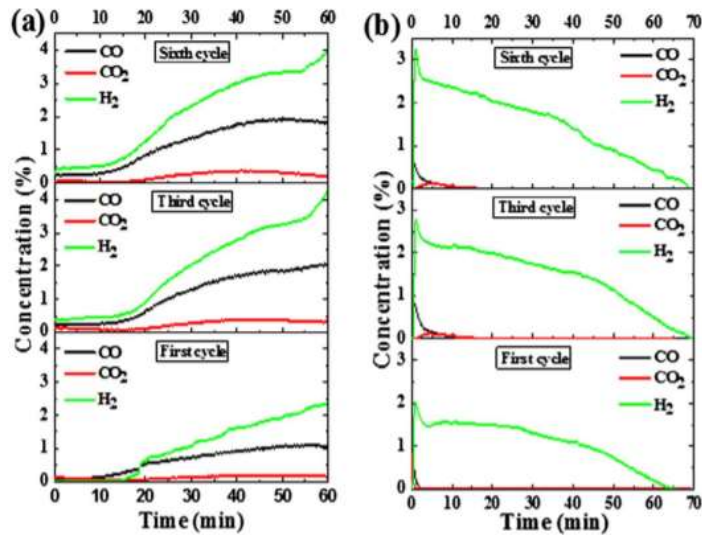


Figure 50: Reduction and oxydation cycle for H₂, CO and CO₂ [8].

In this case the average concentration of resulting gases is higher, which means that it will have higher yields of syngas and hydrogen. However, it is evident that the formation of CO₂ in the reduction step and CO in the water oxidation step is reduced compared with the original one; this means that the calcinated magnetite will have a higher relative selectivity of syngas and hydrogen. In the stable state, the calcinated magnetite oxygen carrier produces syngas with a yield of 10.64 mmol/g and purity of 96.30% and hydrogen with a yield of 5.25 mmol/g and purity of 96.52% [8].

Focusing on the reduction step of original magnetite it is possible to observe that all the reduction processes have a shorter duration period especially at temperatures above 1273 K.

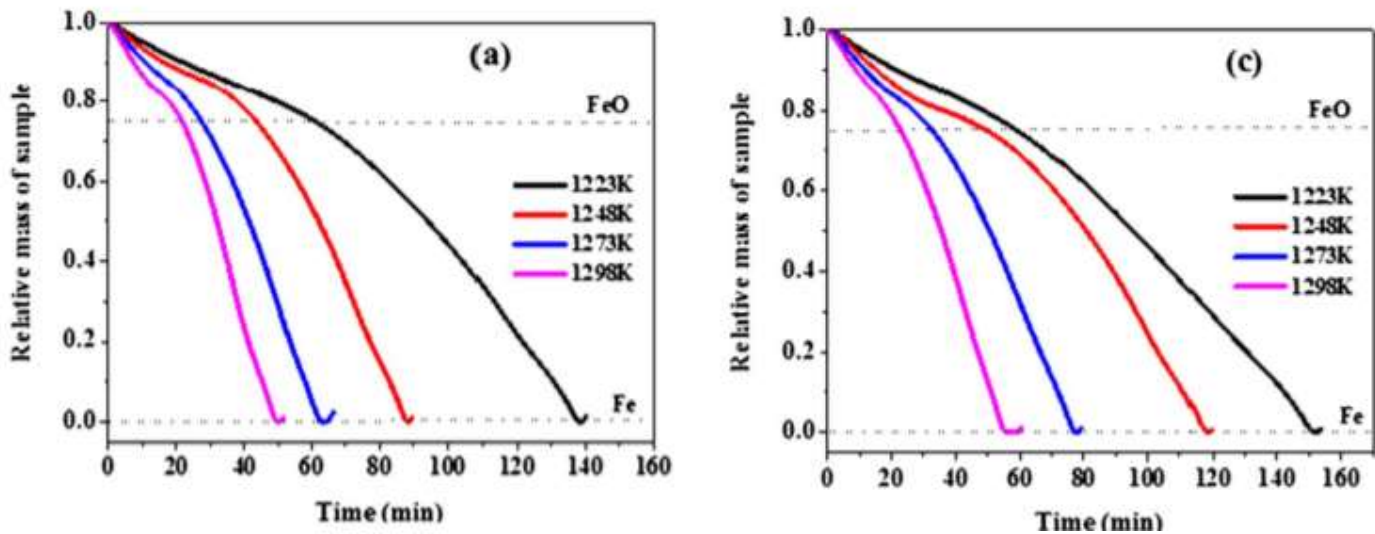


Figure 51: Reduction via methane of (a) original magnetite and (b) original magnetite after 6 cycles [27].

By increasing the reduction temperature, within the same reduction time the mass loss is bigger. It is possible to find that the activation energy for the analyzed samples (original and calcinated magnetite, first or sixth cycle) changes from 74.08 to 93.02 kJ/mol. The lowest activation energy (74.08 kJ/mol) is found in the calcinated sample. It may happen because part of Fe₃O₄ is oxidized to Fe₂O₃ after calcination in air, because the Fe₂O₃ shows much higher reducibility than Fe₃O₄. In Monazam's research the activation energy for the reduction of Fe₂O₃ to FeO over the temperature range of 973–1098 K was 34–39 kJ/mol, while for the reduction of Fe₃O₄

with CH₄ the activation energy (from Fe₃O₄ to FeO) is much higher (60–175 kJ/mol) at the temperature range of 1273–1573 K, which is higher than the one obtained for the calcinated magnetite [28]. The relatively low activation energy of calcinated magnetite can be attributed to the formation of Fe₂O₃, which has a higher reducibility than Fe₃O₄. It is also necessary to say that the activation energy varies largely between different studies, according to the different reducing atmosphere and oxygen carrier components. Reducing atmosphere are known to impact largely on the whole reaction process.

Source	Gas	Metal oxides	Temperature (K)	Reduction step	Activation energy (kJ/mol)
Current study	CH ₄	Original magnetite	1223–1298	Fe ₃ O ₄ to FeO	93.02
		Calcinated magnetite		Fe ₂ O ₃ to FeO	74.08
		Recycled original magnetite		Fe ₃ O ₄ to FeO	86.90
		Recycled calcinated magnetite		Fe ₃ O ₄ to FeO	90.98
Go et al. [26]	CH ₄	Fe ₂ O ₃	1073–1173	Fe ₂ O ₃ to FeO	271
Steninfeld et al. [44]	CH ₄	Fe ₃ O ₄	1273–1573	Fe ₃ O ₄ to FeO	60–175
Monazam et al. [46]	CH ₄	Hematite	973–1098	Fe ₂ O ₃ to FeO	34–39
Trushenskiet al. [59]	CO/CO ₂	Hematite	873–1173	Fe ₃ O ₄ to FeO	64.46–78.27
Moon et al. [60]	CO/H ₂	Fe ₂ O ₃	1073–1273	Fe ₂ O ₃ to FeO	19.84–42.15
Behdad et al. [61]	CH ₄	Fe ₂ O ₃ /Al ₂ O ₃	1073–1223	Fe ₂ O ₃ to FeO	25

Figure 52: Activation energy for different studies[28].

From the table it can also be noted that the activation energy using H₂ or CO is much lower than the case in which the reducing gas is methane. Indeed, from the studies conducted by Moon et al. it is possible to see that using CO and H₂ as reacting gases, the values of activation energy for Fe₂O₃ transform to FeO are in the range of 19.8–42.15 kJ/mol, while from Kang et al. [26] it can be noted that the value of activation energy for the reduction of Fe₂O₃ to FeO by methane is 271 kJ/mol. In the study presented by Chunqiang Lu [27], the lowest value of the activation energy for the reduction of Fe₂O₃/Fe₃O₄ to FeO is 74.08 kJ/mol, even if the reaction temperatures are higher. Generally, higher temperatures translate to lower activation energy because mobility of atoms and bondage breaking is promoted by higher temperatures. This discrepancy can be related to the bigger particle size of oxides. El-Geassy et al.[29] found a correlation between activation energies for iron oxides reduction and their particle size: for 100

μm particles, the activation energies of Fe_2O_3 transform to Fe is in the range of 9.5–21.5 kJ/mol.

In absence of a reducing agent in the chemical looping reaction, the temperatures required for the reduction step will be higher. The following study will address an experiment in which the iron oxide was reduced without the use of any gas to help reducing the temperature of the reduction.

2.4 Iron Oxides chemical looping

Many studies in literature, such as the one carried out by Charvin et al. [30] address the hydrogen production from the two-step iron oxide thermochemical cycle using solar radiation as source of energy. Thermodynamics of iron oxide thermal reduction and subsequent re-oxidation with steam was performed: in particular the solar reduction of iron oxide (Fe_2O_3) into Fe_3O_4 and FeO was studied. The equilibrium degree of conversion can be defined as the ratio between the quantity of products obtained and the quantity of products which could be obtained from a complete reaction, as it can be seen:

$$\eta_{chem} = \frac{n_{FeO}}{3n_{Fe_3O_4}} \quad (2.1)$$

Where n_{FeO} are the moles of FeO , and $n_{Fe_3O_4}$ are the moles of Fe_3O_4 .

Which refers to the chemical reaction:



The input conditions for the reaction are:

- 1 mol of metal oxide FeO
- Total pressure of 1 bar
- An inert atmosphere with N_2 (100 mol) to avoid presence of oxygen during the reaction step

In the next table the developing of the reactant, during the reduction step, in relation to pressure and temperature is shown [11]:

Reactant	Product	Reaction temperature (°C)	Total pressure (bar)	Chemical conversion (%)
Fe ₂ O ₃	Fe ₃ O ₄	1250	1	60
Fe ₂ O ₃	FeO	2100	1	98
Fe ₂ O ₃	FeO	1950	0.1	95
Fe ₂ O ₃	FeO	1770	0.01	92
Fe ₂ O ₃	FeO	1600	0.001	90

Figure 53: Chemical conversion given by thermodynamics [30].

It is possible to say that the effect of pressure and temperature on the reaction is very relevant. The thermodynamics predict the formation of non-stoichiometric wustite phases $Fe_{1-y}O$ (mainly Fe_{0.947}O) in addition to FeO.

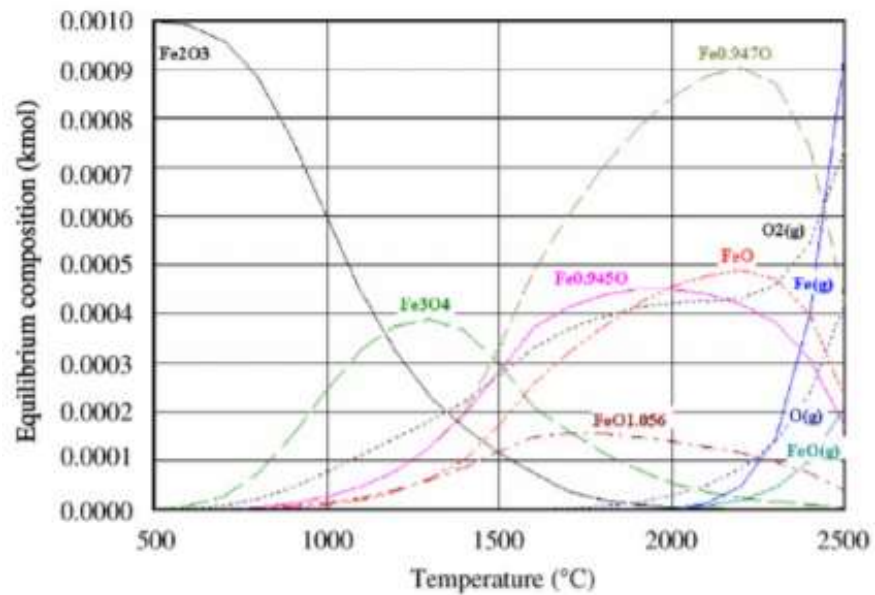


Figure 54: Equilibrium composition results of the Fe/O system (100 mol of N₂, 1 mol of Fe₂O₃, P=1 bar) [30].

A total pressure decrease lowers the reaction temperature below 2000 °C, which leads to higher exergy efficiencies than at atmospheric pressure because of a reduction of radiation losses (T₄

dependency) [30]. The oxidation step is thermodynamically possible if the Gibbs free enthalpy change of the metal oxide redox pair is higher than that of water reduction which means that water splitting with FeO is only possible below 800°C. Being Fe₃O₄ not able to split water spontaneously, an external energy source is required to drive the reaction ($\Delta G > 0$). Then the reaction between FeO and water produces Fe₃O₄ which is not able to further react with water to produce Fe₂O₃.

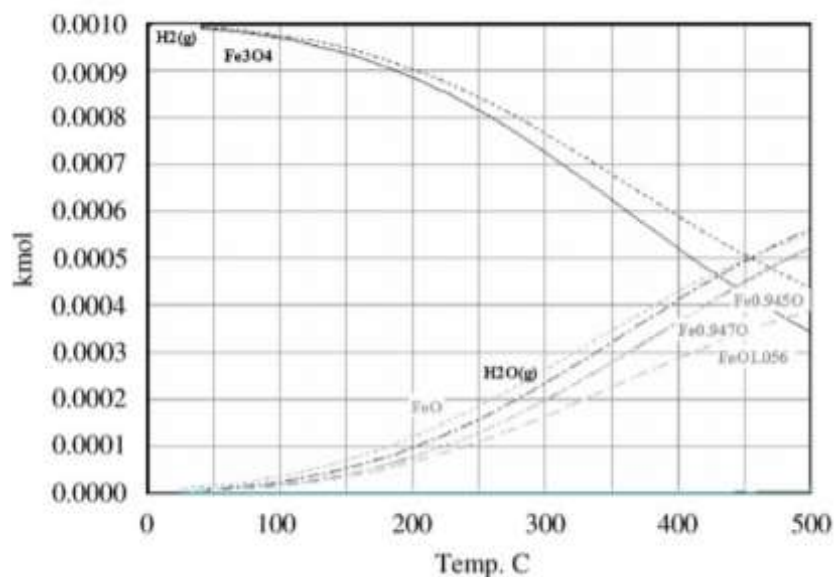


Figure 55: Equilibrium composition results of the Fe/O/H system (3 mol of FeO, 1 mol of H₂O, N₂ atmosphere, P = 1 bar) [30].

As it can be seen from the picture, the theoretical water splitting process decreases with temperature according to thermodynamics. Focusing on the reduction process, the endothermic reaction of Fe₃O₄/FeO cycles occurs at high temperature; the heat is provided by solar thermal power with concentrates direct solar radiation to produce high-temperature thermal energy. Commercial powder of pure Fe₂O₃ (99.9%), with 100 μm of average particle size, was used. The sample (about 1 g weight) was placed on a water-cooled holder and was heated by direct concentrated solar irradiation. For experiments requiring a controlled gas pressure, a glass vessel was placed on the support and an inert gas (static or flowing N₂) was used to provide a controlled atmosphere (vacuum or reduced pressure) around the sample [30].

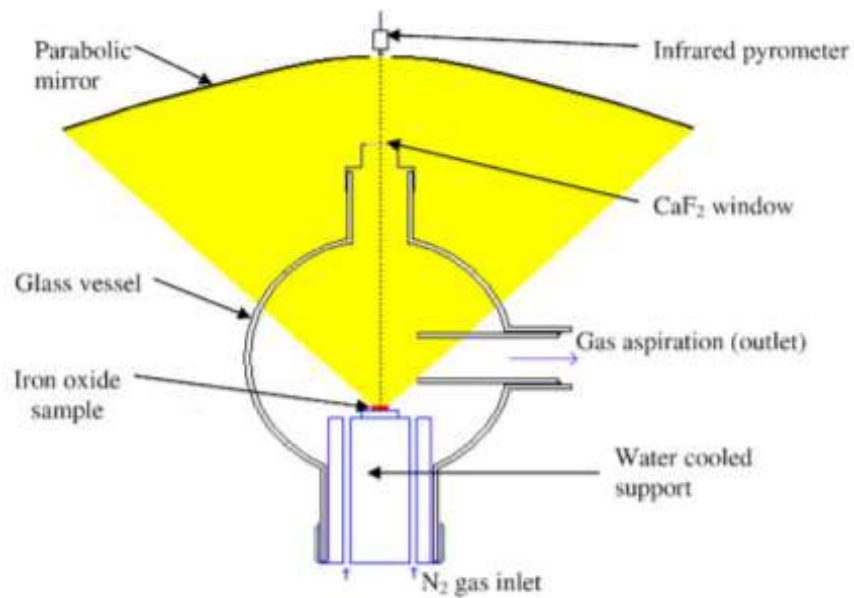


Figure 56: Set-up of the experiment [30].

In order to control the total pressure in the vessel and to guarantee the continuous flow of the inert gas inside the reactor, a vacuum pump is connected to the reactor outlet. The gas flow is used to drift the oxygen released from the reaction to the outlet of the reactor, to prevent the reoxidation of wuestite to magnetite. The whole device was set at the focus of a solar concentrating system consisting of one reflector (flat heliostat) and a concentrator (1.5 m diameter, peak flux density 16 MW/m²). The temperatures reached by the sample can be seen in the picture:

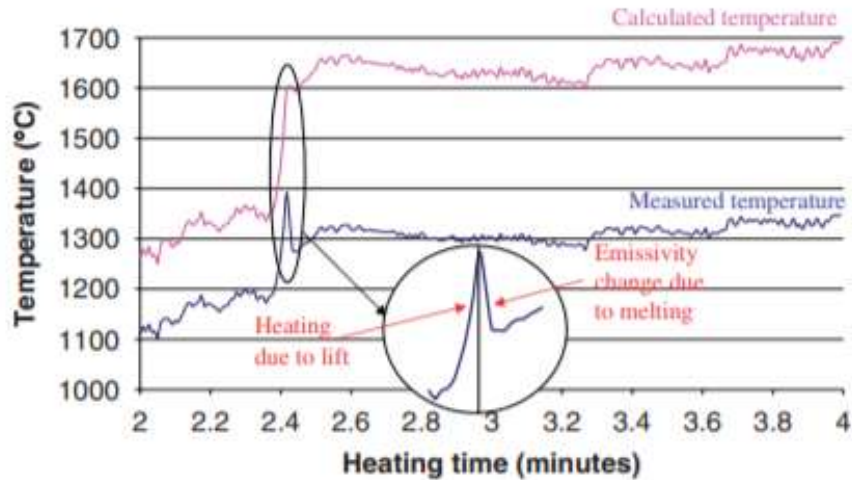


Figure 57: Temperature measurements of a Fe_2O_3 pellet heated under an inert atmosphere by a solar furnace [30].

For the reaction step hematite was used as the initial raw material in the Fe_3O_4/FeO cycle aiming at producing iron oxide (FeO) as pure as possible. Then, FeO (wustite) is used in the water split step (H_2 production), and Fe_3O_4 in the re-oxidation with steam. The cyclic thermal reduction of Fe_3O_4 will be exploited in the next cycles together with water hydrolysis with FeO to produce H_2 and regenerate Fe_3O_4 . Through an x-ray diffraction analysis, it was possible to analyze the process of reduction of hematite, in an atmosphere of $1700^\circ C$, as it can be seen in the figure:

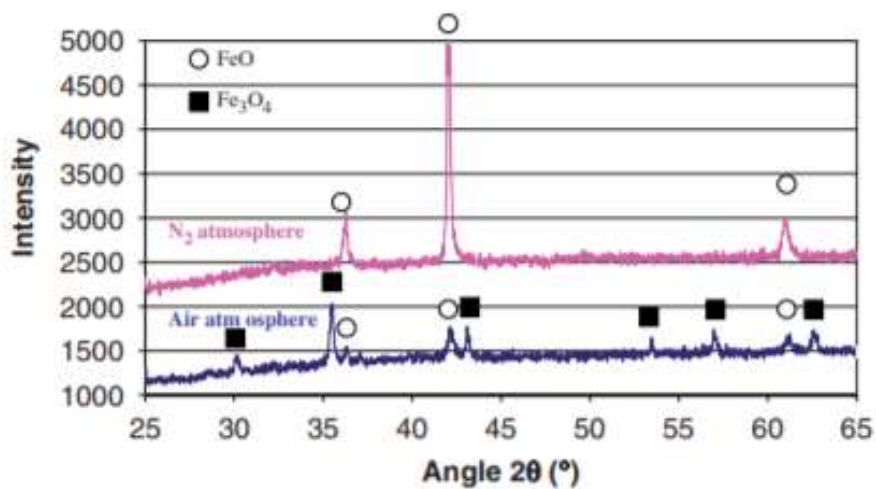


Figure 58: X-ray diffraction pattern of solar-reduced Fe_2O_3 under air or N_2 atmosphere [30].

In the following table it is also possible to understand that the reaction's result depends strongly on the atmosphere composition:

Reactant	Atmosphere	Pressure (bar)	Heating time	Product	Mass fraction of wustite (%)	Chemical conversion (%)
Fe ₂ O ₃	N ₂	0.1	30 s	Fe ₃ O ₄ + FeO	85	95
Fe ₂ O ₃	N ₂	0.1	1 min	Fe ₃ O ₄ + FeO	93	98
Fe ₂ O ₃	N ₂	0.1	2 min	FeO	100	100
Fe ₂ O ₃	N ₂	0.8	2 min	Fe ₃ O ₄ + FeO	91	97
Fe ₂ O ₃	N ₂	0.8	5 min	Fe ₃ O ₄ + FeO	95	98.5
Fe ₂ O ₃	Air	0.8	15 min	Fe ₃ O ₄ + FeO	82	93.5

Figure 59: Results obtained from x-ray diffraction after heating Fe₂O₃ up to 1700°C with a solar furnace [30].

Under air atmosphere the product is a mixture of Fe₃O₄+FeO, while in inert conditions the product is just FeO. The overall reaction can be written as the composition of two separate reactions:

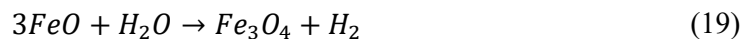


And



The first reaction was completed when 1500°C were reached, while the second one is more complex because the result is never pure FeO but contains also non-stoichiometric wustite. In particular, as it can be seen from the table, in an air atmosphere it was impossible to reach a full conversion into wustite. Instead, the low partial pressure of oxygen given by the inert atmosphere allows to reach a higher conversion into wustite.

For what concerns the water splitting step, the following formula can be considered:



The experiments were performed using samples of 2g. This step requires a lower temperature (approximately 800°C) and the experiment was performed in a tubular fixed-bed reactor (made of stainless steel) positioned in a vertical furnace.

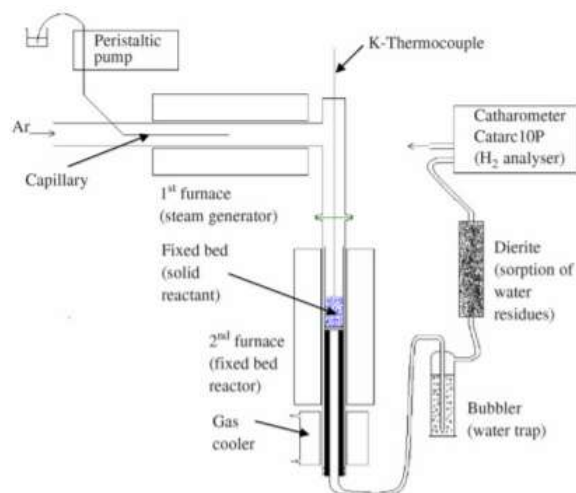


Figure 60: Schematic of the experimental set-up for the oxidation step [30].

The steam that was delivered to the reactor was precisely measured: the water flow was fixed at 12.5 mmol/min (0.225 ml/min). This flow was mixed with a certain mass-flow (220 Nml/min at 0 1C, 1 atm) of argon. At the outlet the flow is cooled down and sent to a gas dryer to obtain a dry mixture of hydrogen and argon. Then the mixture was sent to a gas analyzer that used argon as a reference to calculate the quantity of hydrogen at the outlet. The argon was sent into the reactor before each cycle in order to purge it from the air that could react with the wustite during the temperature increase. The results of the water-splitting step are shown in the following picture:

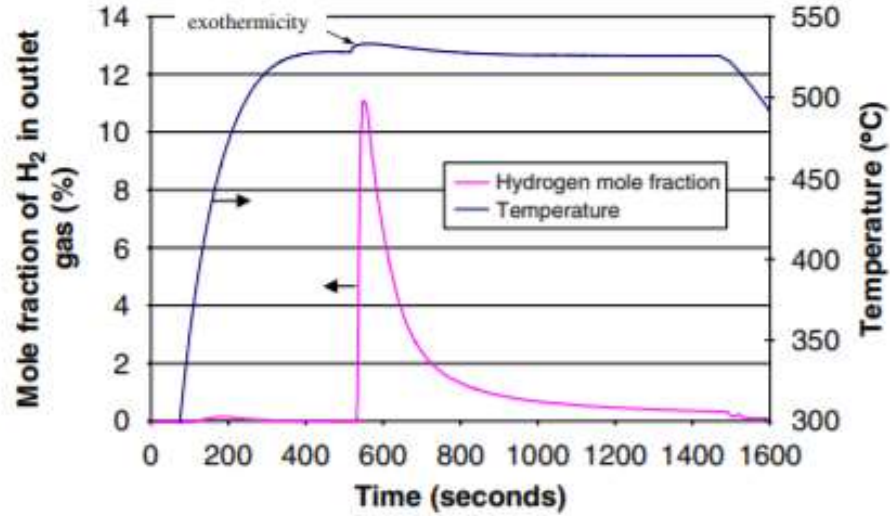


Figure 61: Mol fraction of hydrogen vs temperature produced by the reaction of FeO ($30 < dp < 50 \mu m$) and water.

The slight increase in hydrogen at the first phases of the reaction, when the optimal temperature hasn't been reached yet, can be related to the reaction between the metal oxide and the moisture trapped in the reactor's walls. When the reactor is at the operating temperature the steam is fed to it and the amount of hydrogen at the outlet of the reactor increases sharply. A small temperature increase can also be observed, because of the exothermicity of the reaction. After approximately 30 minutes the hydrogen production decreases sharply and becomes negligible because of the lack of reaction sites in the iron oxide. It is important to underline the impacting effect of temperature on the reaction: the increase in the bed temperature led to an increase in hydrogen productivity thanks to the improved kinetics of the reaction.

The following part is related to the analysis of doped iron oxide with the aim at finding a higher efficiency alternative to the simple oxygen carrier and at reducing the temperatures required for the reduction step.

2.5 Co-doped iron oxides reduction

An important limit for iron oxides oxygen carriers, as well as many other oxygen carriers, is the minimum temperature to trigger the reduction reaction. For this reason, it is interesting to analyze the performances of some doped iron oxide oxygen carrier. In particular, the doping of iron oxides with many earths abundant material can enhance its performance even at temperatures as low as 750°C [31]. The doped materials confronted are CoFe_2O_4 , $\text{Mn}_{0.2}\text{Co}_{0.8}\text{Fe}_2\text{O}_4$, $\text{Mn}_{0.4}\text{Co}_{0.6}\text{Fe}_2\text{O}_4$ and $\text{Mn}_{0.6}\text{Co}_{0.4}\text{Fe}_2\text{O}_4$. The reactor in which the test was performed is of the fixed bed type and has an internal diameter 10 mm and a total length of 350 mm. The heat for the reaction was provided by a furnace. The mass of the sample is 0.5g and it was firstly exposed to a reducing agent (with a 20% of H_2 and 80% of N_2 in volume inside a gas mixture of flow rate 800 mL/min) and then to an oxidizing agent (with a 20% of CO_2 and 80% of N_2 in volume inside a gas mixture of flow rate 800 mL/min). The range of temperatures in which the tests were performed are 550–850 °C. As can be seen in the following picture, all the materials have high reduction performances which, as expected, reduce with temperature:

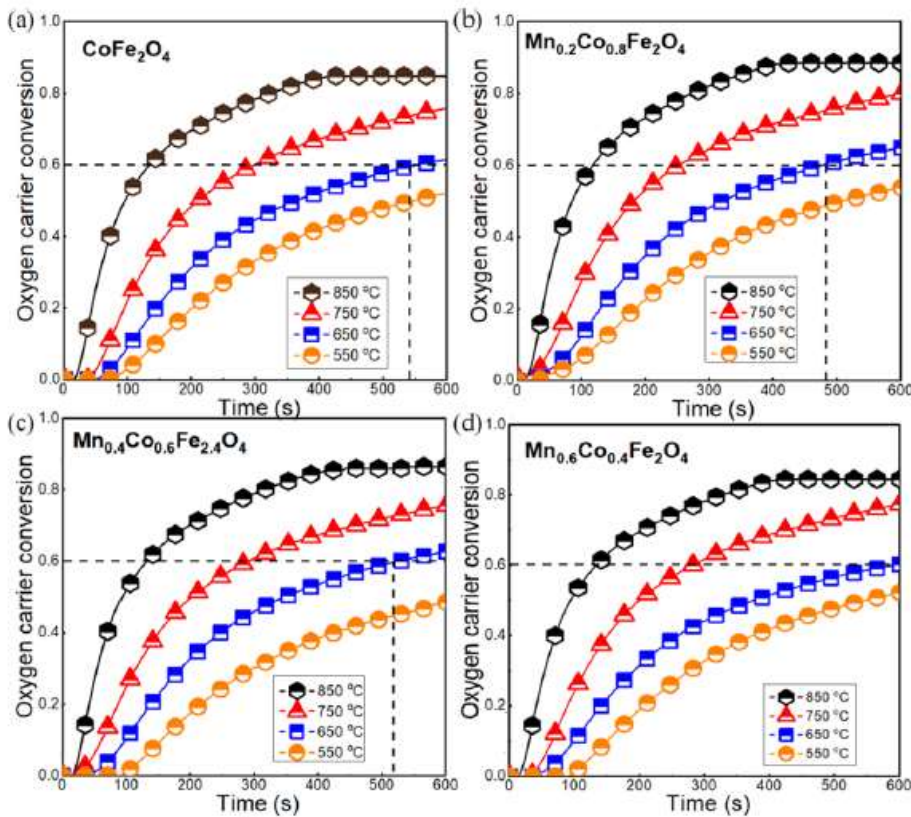


Figure 62: Reduction of doped iron oxides [31].

In particular it can be noted that an oxygen conversion of 0,6 was obtained, at 650°C, in 540, 480, and 490 s for CoFe_2O_4 , $\text{Mn}_{0.2}\text{Co}_{0.8}\text{Fe}_2\text{O}_4$, $\text{Mn}_{0.4}\text{Co}_{0.6}\text{Fe}_2\text{O}_4$ respectively. Among all these materials the one that showed higher performances at all temperature is $\text{Mn}_{0.2}\text{Co}_{0.8}\text{Fe}_2\text{O}_4$. The positive effect brought by the doping can be underlined by the activation energy as well: it is 30.8, 32.4, 35.9, and 40.7 kJ mol^{-1} for CoFe_2O_4 , $\text{Mn}_{0.2}\text{Co}_{0.8}\text{Fe}_2\text{O}_4$, $\text{Mn}_{0.2}\text{Co}_{0.6}\text{Fe}_2\text{O}_4$ and $\text{Mn}_{0.6}\text{Co}_{0.4}\text{Fe}_2\text{O}_4$ respectively. The relatively low activation energy of $\text{Mn}_{0.2}\text{Co}_{0.8}\text{Fe}_2\text{O}_4$ indicates its reduction potential at low temperatures.

Another group, Gou et al [32] analyzed the performance of Co-doped iron oxides. In particular, a sample weighting 15 mg (mounted on an alumina crucible and preheated at 800°C for 5 successive reduction-oxidation activation cycle) underwent 10 continuous reduction-oxidation cycles at 600, 700 and 800°C. The reduction agent used in the first step of the chemical looping was a mixture of 25% CH_4 (50 mL/min) mixed with an inert gas (50 mL/min of N_2 and 100 mL/min of helium mixture used as carrier gas) for 5 min, while the oxidation process used 25% air (50 mL/min) for 5 min. Before alternating the two processes a 10-minute flushing was applied to avoid mixing between of oxygen and methane. In the following figure it is possible to see the oxygen carrier conversion rate in 10 cycles of CH_4 partial oxidation and air regeneration adopting a 2% Co co-doped iron oxide at 600°C, 700°C and 800°C. The results of the TGA show that the use of the co-doped iron oxide dramatically increase the conversion rate in the oxygen carrier reduction and the also its regeneration in respect to the un-doped Fe_2O_3 . In particular, focusing on the reduction process, it can be seen that the rates of reduction for what concerns the 2% Co co-doped Fe_2O_3 were 390%, 526%, and 424% higher than that of un-doped at Fe_2O_3 600 °C, 700 °C and 800 °C respectively.

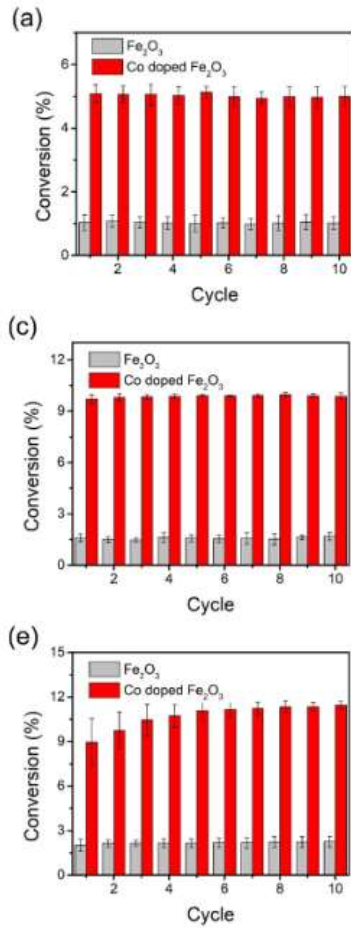


Figure 63: Reduction reaction at 600°C, 700°C and 800°C [32].

Other concentration of cobalt were analyzed in this study (0.5%, 1%, 2% and 5%) and in all these cases the co-doped oxygen carrier showed enhanced performances in respect to the undoped one, also in the oxidation step [32].

Chapter 3

3 Experimental Activity at the Energy Center

3.1 Test Bench description

The experimental activity was carried out on the rooftop of the Energy Center, Turin, where the solar concentrator system is positioned. The main instruments used during the experiments are listed in the following:

- The two cylinders containing methane, used for the reductio reaction, and nitrogen, use to purge the reaction zone from oxygen before sending in the methane.
- The piping system, which was used to connect the reactor, positioned on the focus of the solar concentrator system, with the cylinders. Through this system was both exploited to send nitrogen and methane into the reactor, but it was also utilized to connect the output of the reactor, in which the products of the reaction that took place in the reactor could be found, with the analyzed. Here the system of manual valves was used in order to make the purging possible at the beginning of every experiment. Indeed, by closing the valves it was possible to create a condition close to the vacuum one, during which the nitrogen was sent in the pipes to the reactor to remove as many traces of oxygen as possible from the reaction site.



Figure 64: Pumping system.

- Pumping system: it was used to create vacuum conditions inside the cylindrical reactor before sending methane in. When the reduction reaction could be started, after the required preparation, the pump would be turned off.
- Weigher, which was used to weight the mass of iron oxide required for the reaction, according to the dimensions of the cylindrical reactor.



Figure 65: Weight of the hematite.

- Caliber, which was used in order to calibrate the mass-flows of methane and nitrogen sent in the reactor
- Siemens display: in which the temperatures (thanks to the connection to a system of thermocouples), pressures and mass-flows in the reactor would be shown. For what concerned the mass-flows it required calibration in order to send the right amount of reactants inside the reacting zone.



Figure 66: Siemens display.

- Iron oxide: in the experiments hematite (Fe_2O_3) was used as oxygen carrier in the reduction process.
- Solar dish collector:



Figure 67: Solar dish collector.

The parabolic dish collector used during our study has the following features:

- i. concentrator surface of $4,5 \text{ m}^2$
 - ii. optic efficiency of 80%
 - iii. mean direct solar radiation of $800 \frac{\text{W}}{\text{m}^2}$
 - iv. concentrated power, at optimal conditions, can reach the value of 2,8 kW
 - v. focal point temperatures above 1800°C
- Hollow cylinder: many materials were used as solar reactors for this study. It was started with an Alumina reactor (Al_2O_3). Its fragile feature was an obstacle for the fulfillment of the experiment's goal which led to the choice of a more resistant material, mainly metallic. For this

reason, first stainless steel, then Inconel and also Astenalloj were used as reactor materials, all with destructive result, which will be discussed later.



Figure 68: Cylinder mounted on the solar collector.

- Emerson XR (gas analyzer): instrument used to analyze the output of the reduction reaction. It allowed the detection of five chemical species: CO_2 , H_2 , CH_4 , O_2 , and CO , one for each channel.



Figure 69: Emerson gas analyzer.

3.2 Experimental set-up

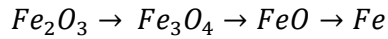
The experimental study took place on the rooftop of the Energy Center, where the solar dish collector is placed. The reactor preparation required some preliminary steps, as it was necessary to fill it with the iron powders under a vent to prevent human hazard. Indeed, it was necessary to position it in a plastic container in order to weight it. For what concerns the mass of iron oxide inserted inside the reactor, the following consideration was made:

$$L = 1,5D$$

Which means that the length of the reactor tube in which the hematite could be found would be 1,5 times the diameter of the tube itself. Therefore, according to the density of hematite, which is $6,9 \text{ g/cm}^3$, different masses of the oxygen carrier will be found in each experiment.

The reaction temperatures are not stable as it would be in a controlled environment, such as a laboratory, which means that to reach the optimal temperatures for the reduction reaction it was necessary to perform the experiments in specific moments, where the solar radiation was at its maximum. The objective was to run the experiment when the thermocouple would detect temperatures of 800°C or higher, which was the minimum required for the reaction to occur when methane is used as a reducing agent, as seen in literature [33]. At the beginning of the test, the gas analyzer was connected to the output of the reactor, the valves (in the piping system), connecting the reactor to the external environment were closed, the pumping system was activated (in order to apply a differential pressure in the cylinder with comparison to the environment), and a mass-flow of nitrogen was sent inside the cylinder where the reaction will take place in the following steps. This procedure was necessary in order to purge the system from any trace of oxygen present inside the reactor tube. Indeed, this would lead to a premature re-oxydation during the reduction process. This procedure was run until the Emerson gas analyzer would read a low value of oxygen at the output of the reaction. Then the pump was turned off, the valves connecting the methane tank to the reactors were opened and a mixture of methane and nitrogen was sent in. The ratio between the two gases, CH_4/N_2 , was selected according to literature, comparing the mass of the samples to the amounts of gases used for the experiments. Monazam et al. [33] analyzed the kinetics of the reduction of hematite using methane as a reducing agent; in particular, the reaction of reduction was assessed also considering the effect of the concentration of methane in the $\text{CH}_4\text{-N}_2$ mixture. The study focused on the analysis of several experiments, which were led within the temperature range of 700–

825°C and with concentration of methane varying from 15-20-35%. For hematite the following series of reaction was considered:



It can be noted that the amount of carbon deposition increases with temperature and with concentration of CH_4 . However, by analyzing the normalized data for CH_4 concentration of 20% and 35% it was possible to see that the increase in methane led to an increase in the carbon fed by 75% and an increase of the carbon deposition of only 30%, as can be seen in the figure:

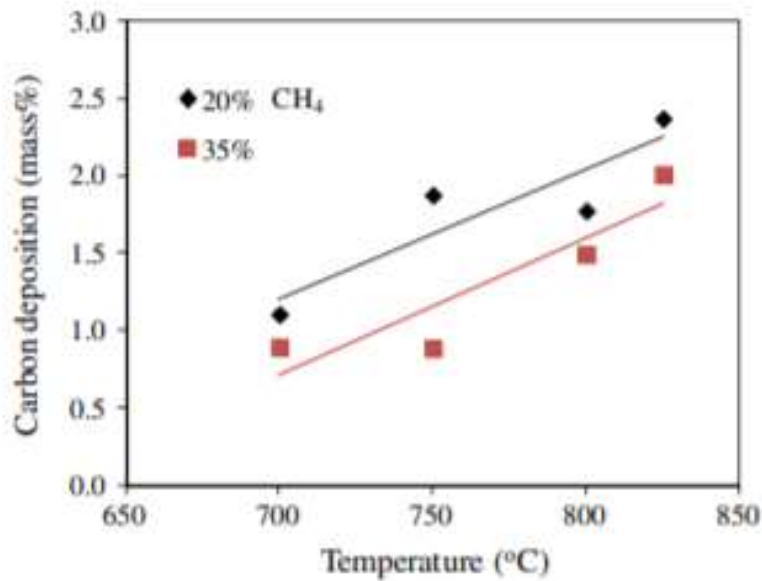


Figure 70: Carbon contents in reduced hematite for different temperature and CH_4 concentrations (20% and 35%).

This small increase in the carbon deposition phenomenon is countered by an increase in the total conversion of hematite, especially at higher temperatures.

For this reason, the mass-flow that would be sent to the reactor during the testing phase would have a methane concentration of 35% in a mixture with nitrogen. In particular the total mass-flow fed to the reactor would be equal to $260 \text{ Nmol}/\text{min}$.

3.3 Test #1

The first test was performed using an alumina tube reactor with the following dimensions:

- Internal diameter of 14 mm
- External diameter of 18 mm
- Length of 200 mm

First, a calibration operation was required in order to make sure that the amount of gas we want to react with the powders is the same read shown in the system's display. Then, after preparing the reactor, by introducing the iron oxide powder inside the tube and sealed inside with wool glass, it was mounted on the solar concentrator in a way that would allow the focal point to be in the same position in which the hematite powder is located. Then the reactor was connected to the piping system, from which the inert gas and the reactant gases would flow (as well as the products of the reaction afterwards).

The amount of hematite use for the first experiment was 3,79 g. This amount depends on the dimensions of the tube reactor in order to have a length of the volume occupied by the powders equal to 1,5 times the diameter of the tube. For what concerns the gaseous flows, the amount of methane sent inside the reactor was $91 \text{ Nmol}/\text{min}$, while the amount of nitrogen was $169 \text{ Nmol}/\text{min}$.

This test had a destructive ending from the reactor's point of view: when turning on the tracking system of the solar concentrator, the fact that a large temperature gradient on the alumina tube surface would damage it wasn't considered. Indeed, not long after the solar concentrator got in the optimal position to capture and reflect the direct radiation, the ceramic thermocouple mounted on the reactor showed a temperature increase from almost ambient conditions to up to 1000°C in just a few minutes. These conditions put the reactor's material under such a stress, due to the thermal shock, that even without any mechanical stress applied to it, the tube failed.



Figure 71: Alumina tube after thermal shock.

Despite the optimal meteorological condition, this accident didn't allow us to make any measurement; however, it was still a useful information that was used in the following tests in order to find a solution to the variability of the temperature on the reactor's surface. In particular the focus was on the possibility to avoid such large temperatures ramps.

3.4 Test #2

In the second test the same set-up of the first one was applied, and the attention was focused on how to deal with the thermal sock issue. In order to have a more gradual increase of the temperature on the reactor's surface, a "manual" solution was tried. The main purpose here was to reduce the initial reflective surface of the solar concentrator system and then to gradually increase it as the temperature would increase, in order to have a slower temperature increase. To do this the reflective surface of the solar dish was partially covered with paper sheets as shown in figure:



Figure 72: Parabolic collector with covered reflected surface.

Starting from the configuration in which most of the mirror's surface were covered, we would wait for the reactor to reach a constant temperature and then we would remove one sheet of paper in order for the system to reach higher temperature levels. Then the procedure would start

again, removing one by one all the sheets from the reflective surface, waiting, during each step, for the reactor to be at a constant temperature. When all the sheets were removed the thermocouple registered temperatures up to 800°C. In these tests it was possible to experience increase of temperature that wouldn't exceed 100°C, which is still not a gradual as in laboratory conditions, where the temperature can be regulated, but it's an improvement in respect to the previous case in which there was a temperature increase of 800°C within minutes. Indeed, this procedure is completely different from the procedure that would be carried out in laboratories, where the heating rate would be of approximately 5-20°C/min [33], but it was the simplest way to impose a slow heating rate on the solar reactor; otherwise, the ramps would have been much larger than the ones that were met in this test. However, even with this method it was impossible to perform a measurement. In this case the reactor was functional through the first stage of the experiment, as we could see from the low differential pressure inside the tube. This means that the gradual increase of temperature up to the operating ones of 800°C worked. However, the meteorological conditions didn't allow to keep the temperatures constant on the reactor's surface for long. Indeed, due to clouds that covered the sun, after all the procedure made to keep the heating rate as low as possible, the temperature difference perceived by the alumina tube was as high as 300°C. This was enough thermal shock for the tube to crack, making the measurements impossible. Indeed, the crack could be seen from the pressure measurement: the differential pressure was no longer at values that would lead to the conclusion that a semi-void condition was established inside the reactor. Generally, at best, the differential pressure inside the tube would reach values of -381,22 mbar. From this test it was clear that it was necessary to have a reactor's material that could stand not only the high temperatures, but also the high temperature ramps. That's why the following experiments were characterized by the use of a metallic reactor.

3.5 Test #3

In the third test a regular iron tube was used as the reactor. Its dimensions are:

- Inner diameter 15 mm
- Outer diameter 18 mm
- Length 245 mm

In this occasion the maximum temperature registered on the thermocouple mounted on the reactor was around 780°C. The mass of hematite present inside the reactor was equal to 2,7 g. In the following it's possible to analyze the results of the reaction. It's possible to see that at the beginning of the reaction, as soon as the methane is sent in, the output has an immediate production of hydrogen, which grown over time. However, it can also be noted that in the first minutes of the reaction the amount of methane found at the output is not negligible, despite what we would expect from an ideal reaction. This can be blamed to the fact that the temperature inside the reactor is not as high as the reaction would require, which is at least around 800°C; it can also be seen that the temperature over the whole duration of the reaction is not constant and increases; that is why the amount of hydrogen produced keeps increasing and the quantity of methane starts decreasing. Furthermore, the variability of the meteorological conditions can be noted by the fact that the concentration of methane at the output is never constant but varies largely, probably due to the variability of heat reaching the reactor. It can also be seen that the hydrogen production doesn't immediately stop with the pressure drop; the gas analyzer detected the presence of hydrogen until the concentration of oxygen increased. This can be attributed to the fact that the conditions inside the reactor are still favorable for the reaction to happen, as soon as there is no oxygen inside. It is also to be noted that at the beginning of the reaction there is a relatively higher concentration of CO, which is not generally expected to be that large in this kind of reactions. The most reasonable reason to explain it is that the methane reacted with part of the oxygen released (partially oxidated) by the reduction of the hematite producing CO.

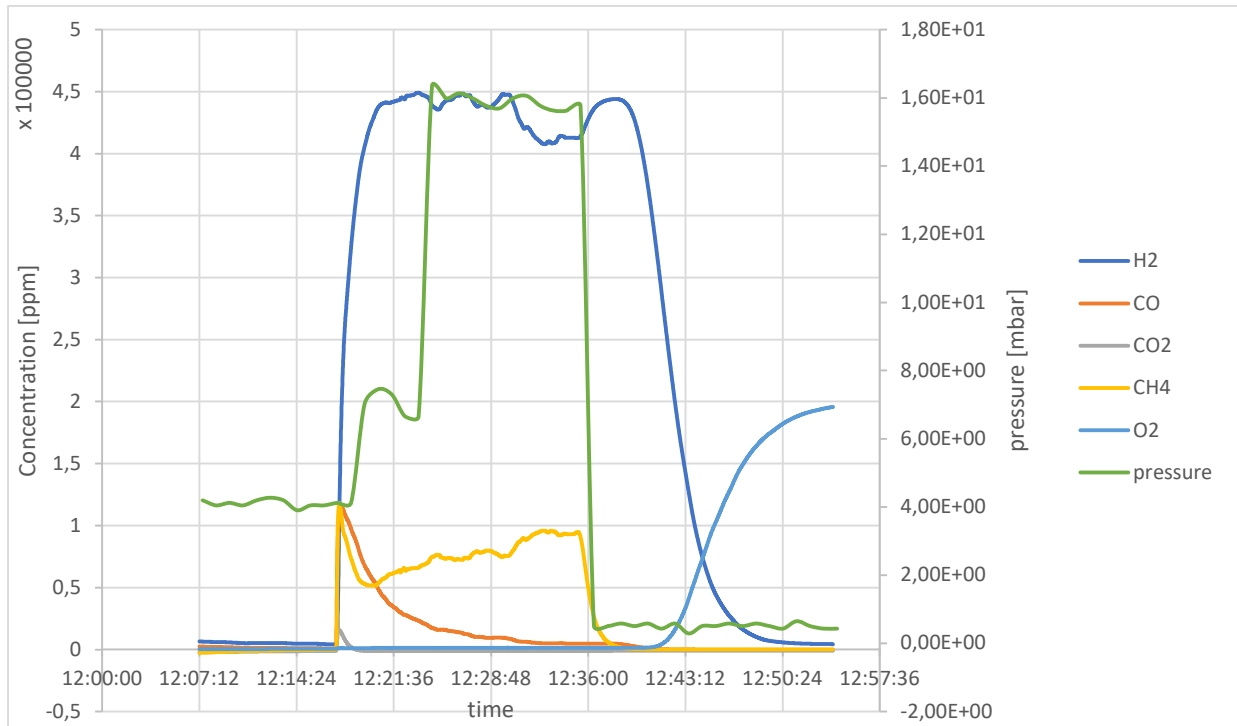


Figure 73: Results of test #3.

Here it is possible to see that after 30 minutes from the beginning of the experiment the reactor experienced the pressure drop. After that, within 15 minutes the presence of oxygen was detected at the output of the reactor, which indicates that the conditions are no longer favorable for the experiment to be carried out. Indeed, as we found out later, the tube melted and there was no longer the oxygen free condition outside the tube, which is necessary to properly analyze the reduction process of hematite and the following production of hydrogen. In this study the hematite wasn't analyzed after the reduction process, which means that it's not possible to know with high accuracy what is the quantity of oxygen carrier reduced. However, the attention here is not particularly focused on the efficiency of the reduction process as much as in the success of the reaction itself. Therefore, analyzing the graph it is possible to say that the reaction that occurred inside the reactor allowed for the reduction of the hematite with methane and the following production of hydrogen.

3.6 Test #4

The fourth test was the one giving the least significant results. It was carried out using an Inconel tube for the reactor. Its dimensions are:

- Internal diameter 8 mm
- External diameter 12 mm
- Length 210 mm

The mass of hematite that could be found in the reactor is equal to 0,53g. The mass-flows of methane and nitrogen are always 91 Nmol/min and 169 Nmol/min. The temperature generated by the solar concentrator on the surface of the reactors were around 750-950°C. In this test a proper measurement wasn't possible, and the outputs of the reaction were much lower than in the other measurements; furthermore, the early melting of the reactor tube didn't allow for the reaction to progress enough to give satisfying results. Focusing on CH_4 , H_2 and O_2 :

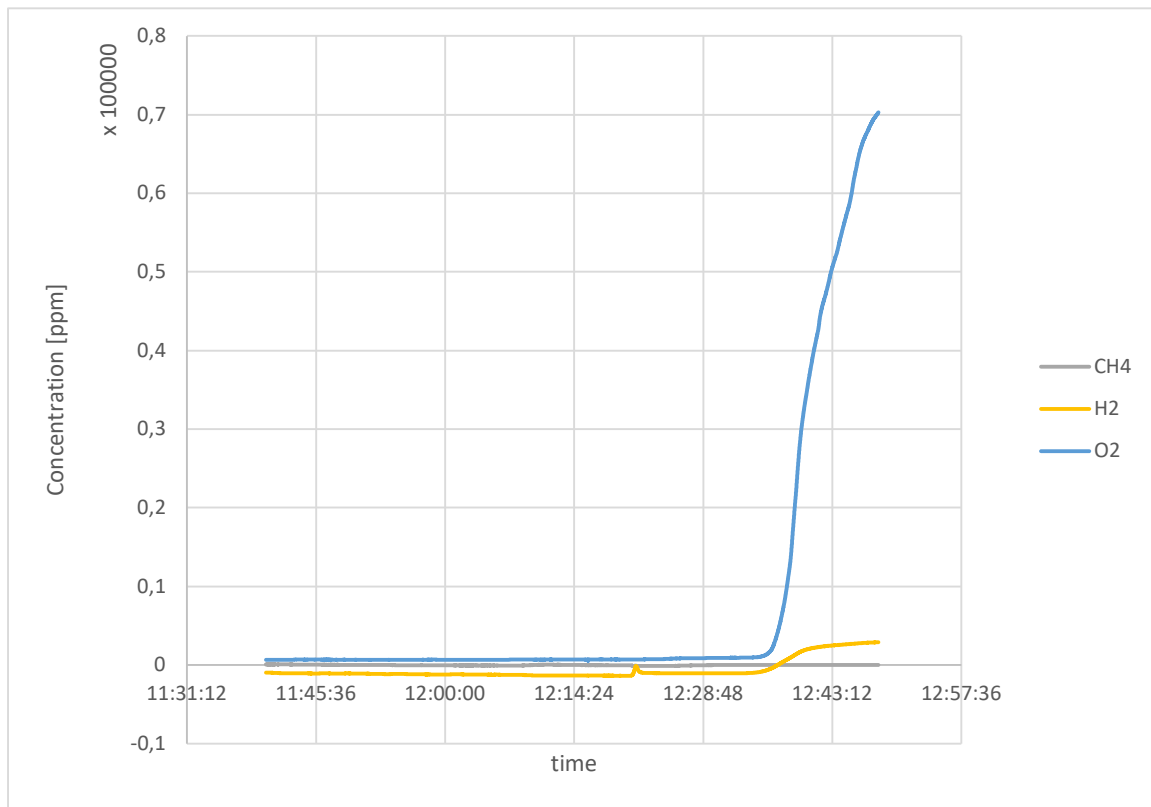


Figure 74: Result of test #4.

Here it is possible to see how the concentrations of hydrogen during the reaction are very low. Its negative value can be due to an error in the detection performed by the gas analyzer. The concentration of methane is negligible for all the duration of the reaction, being it three orders of magnitude lower than in the other cases. The beginning of the reaction can be identified with the increase of the hydrogen concentration, that takes place around 12:35. However, it is almost negligible compared to the other cases studied. Furthermore, it can be seen that, after a few minutes from the beginning of the reaction, a very large increase in the oxygen concentration occurs. This is a clear signal of the melting of the tube.

3.7 Test #5

In the last test the material used for the reactor was the hastelloy. The dimensions of the tube are:

- Internal diameter of 9 mm
- External diameter of 12 mm
- Length of 200 mm

According to the dimensions of the tube, the amount of hematite inserted inside it was equal to 0,865 g. The mass-flows of methane and nitrogen during the experiment are always $91 \text{ Nmol}/\text{min}$ and $169 \text{ Nmol}/\text{min}$ respectively. The temperatures in the reacting zone of the hastelloy tube are around 800°C (there is a large fluctuation of this value due to meteorological variability during the experiment).

Here it is possible to see that the data collected by the Emerson data analyzer are close to what we were expecting from the reaction, as can be seen in the following table:

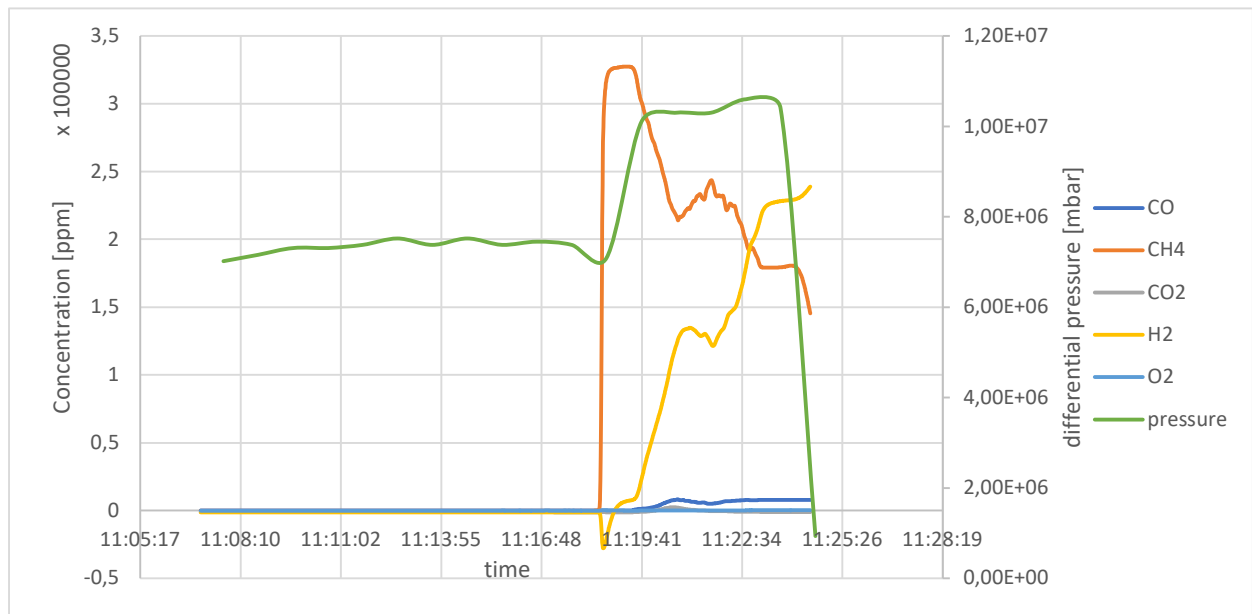


Figure 75: Test #5 results.

It can be seen how at the beginning of the test the concentration of methane at the output are higher because the reaction didn't start yet. Then it can be seen how the conversion of methane

into hydrogen occurs at approximately 11:16. Here it can be seen that the concentrations of methane start slowly reducing while those of hydrogen are increasing, how we expected also confronting our study with the data in literature [33]. Furthermore, it can be seen that the concentrations of CO and CO_2 are much smaller in respect to the amount of hydrogen, and their trend is very close to that of other studies previously analyzed. It is possible to observe that the concentration of methane at the outlet of the reactor is relatively high. This trend can be attributed to the relatively low temperature (around $600^{\circ}C$), that didn't allow for a complete reaction of the methane and that led to it being present in large quantities at the output. It can also be noted that even if the concentration of hydrogen is increasing in time there is a drop around 11:20. This decrease of the hydrogen concentration (that matched with an increase in methane concentration) is provoked by the variability of temperature due to meteorological conditions: presence of clouds and wind generated a drop on the solar power reflected on the reactor's surface and ended up in decreasing the reactor's temperature. However, as it can be seen from the pressure trend, the low-pressure condition was lost after a few minutes from the start. After some time, the reaction had to be stopped because as it can be seen from the figure, around 11:23 a pressure drop occurred, probably due to the failure of the reactor tube. Running the experiment even further would present risks for the mirror of the solar concentrator, because of the melted iron dropping on it.

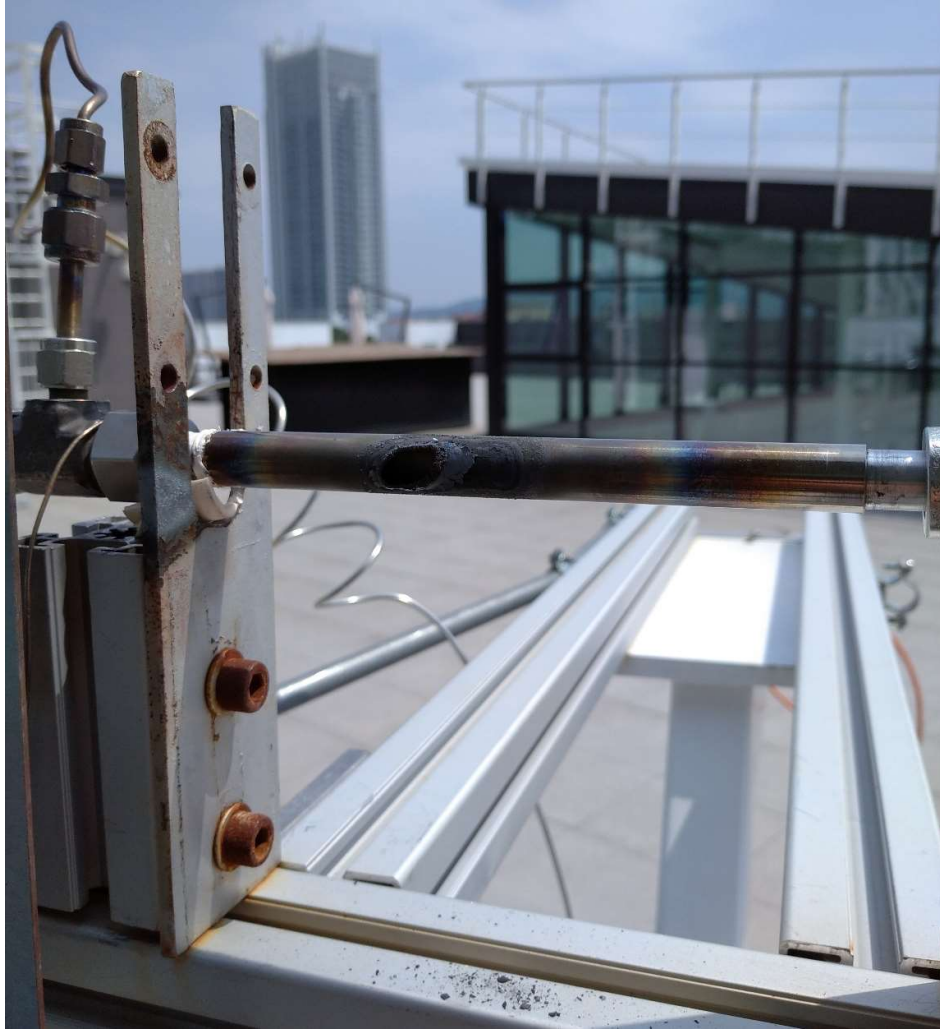


Figure 76: Hastelloy tube failure.

3.8 Conclusions

All these experiments led to the conclusion that the processes of solar chemical looping using methane as a reducing agent and hematite as oxygen carrier are feasible. Given favorable meteorological condition it is possible to reach temperatures high enough to perform the reduction reaction successfully. The tests carried out in the Energy Center had the following set-up:

Table 10: Tests set-up:

Test n°	Mass of Hematite [g]	Mass-flow of CH_4 [Nmol/min]	Mass-flow of N_2 [Nmol/min]	Temperature range [°C]
1	3,79	91	169	900-1000
2	3,79	91	169	800
3	2,7	91	169	780
4	0,53	91	169	750-950
5	0,865	91	169	800

The main issue regarding all the experimental tests is common to all renewable energy sources, which is the volatility of the energy source exploited. In particular the main problem faced was related to thermal ramps, which led to the failure of all the reactor's materials at a more or less developed point of the reaction. Nevertheless, it was possible in some cases, in particular experiment 3 and 5, to collect more data in order to understand more in detail the rate of the reaction. The main concern was related to the feasibility of the reduction at temperatures as low as 800°C. The gas analyzer provided precious information, in particular related to hydrogen concentration. Indeed, the concentration of hydrogen produced is related to the rate of reduction of the hematite, which is the main purpose of the experiments. Despite requiring several specific conditions in order to obtain it, with the solar concentrator, the reduction of hematite via solar concentrated radiation was performed.

Chapter 4

4 Chemical simulation

In order to validate the results obtained with the experimental activity, a model was built on the COMSOL Multiphysics was created. For reasons related to computational complexity the model was chosen to be in a 0-dimension space with the Reaction Engineering physics. At the beginning it is necessary to define the reactor type: in this case it was chosen to be a continuously stirred reactor with constant volume. Furthermore, we consider it to be perfectly mixed, and the operative temperature was set to 950 °C. The starting point of the model was taken from the study performed by Monazam et al. which can be summarized by the methane decomposition and reduction of hematite to Fe_3O_4 (R2), which occurs simultaneously with the reduction of Fe_3O_4 to FeO (R1). The two reactions occur with different rates, as can be seen from the following figure:

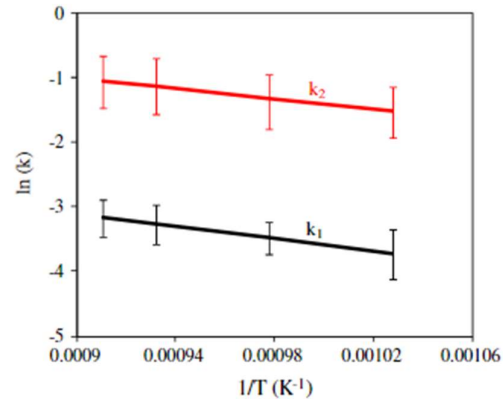
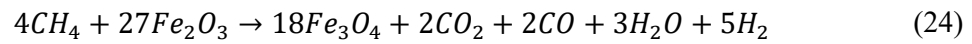
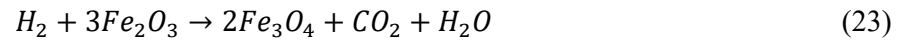
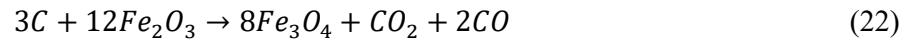
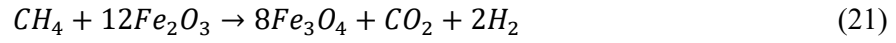


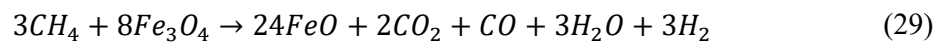
Figure 77: Reaction rate of R1 and R2.

The two reactions are expressed in the following:

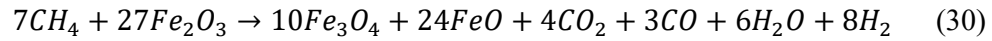
R2



R1



The overall reaction can be written as:



First of all, the reaction engineering model must select the type of reactor used and the temperature at which it is working. For the purpose of this simulation, the reactor was considered to be a continuously stirred reactor with a constant volume, as it allows reactions between a gas and a solid surface. It is assumed to be perfectly mixed, so that the species concentrations of the output flow are the same as the concentrations in the reactor volume. The temperature was set to about 950 °C. Reaction Engineering allows you to add various chemical reactions that happen simultaneously. The parameters needed by the software are the chemical reaction formula, the overall reaction orders (volumetric and surface) and the rate constants (determined through the Arrhenius expressions). All reactions included in the model were considered irreversible. The Arrhenius expression is written as follows:

$$k = A \left(\frac{T}{T_{ref}} \right)^n \exp \left(-\frac{E}{R_g T} \right) \quad (4.1)$$

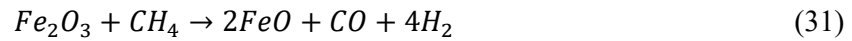
In which:

- A is the frequency factor and indicates the frequency of collision between reactant molecules and a standard concentration. It depends on temperature, activation energy, on the rate at which molecules collide and also their relative orientation.
- n is the temperature exponent and can be set to zero if the other parameters are referred to the operating temperature
- E is the activation energy and indicated the energy barrier that the reaction needs in order to start.

As mentioned before, the reduction reaction of hematite occurs through two parallel reactions, R₁ and R₂, which have a frequency factor of $4.759yCH_4^{0.636}$ and $1.33yCH_4^{1.06}$ respectively.

Here y_{CH_4} represents the molar fraction of methane in the inlet mixture. The apparent activation energies for both reactions R1 and R2 were estimated to be 34.4 ± 0.5 and 39.3 ± 1.5 kJ/mol respectively [9]. However, these reactions are not sufficient to represent the chemistry occurring inside the reactor, therefore a more detailed study has to be performed for what concerns the behavior of the main chemical species at the very high temperatures generated by the solar concentrator.

For the simulation it will be taken into account the fact that not only a complete oxidation is occurring, but also phenomena of partial oxidation. As it can be seen in the following formulas [Lu et al], these reactions don't yield directly CO₂ and H₂O, but only CO and H₂.



The Arrhenius parameters were considered the ones of the study performed by Lu et al., with an activation energy of 74.08 kJ/mol for the first one and 90.98 kJ/mol for the second one [27].

As the reactor used for the process reaches very high temperatures, many phenomena related to methane reactions have to be considered. Carbon deposition (methane cracking) is shown in the following:



In this reaction, which occurs at high temperatures, the methane molecule is directly split in solid carbon and molecular hydrogen. On one side it has the positive outcome of increasing the amount of hydrogen released in the output flow, on the other hand it partially inactivated the hematite powders due to the accumulation of carbon. The values used as input of the COMSOL model are an activation factor of $1.3 \cdot 10^7$ mol/(m²/s) and an activation energy equal to 214 kJ/mol [34].

The following formula, carbon gasification



has a positive effect as it helps to eliminate the carbon from the powders, by producing hydrogen and carbon monoxide. The pre- exponential factor over hematite is $1.8 \cdot 10^4$ m/s and activation energy is 172 kJ/mol [34].

Considering reactions occurring at temperatures higher than 1000K, a considerable effect is represented by the Boudouard reaction: not only it brings a positive contribution by cleaning the substrate from solid carbon deposition, but also helps increasing the transformation of CO_2 into CO .



Here, the value for the pre-exponential factor is $1.2 \cdot 10^6$ mol/(m²/s), while activation energy is 185 kJ/mol [34].

Another positive contribution is brought by the steam reforming reaction which, being an endothermic reaction, is favored by higher temperatures.



Here the methane is converted to more H_2 and CO using H_2O . The values of pre-exponential factor and energy activation are $1.3 \cdot 10^7$ mol/(m²/s) and 214 kJ/mol respectively [34].

Furthermore, to complete the initialization of the simulation, the software requires additional input parameters; among all the tests performed on the rooftop of the Energy Center, the most accurate is the #3 one. That's why the model was built in order to recreate the layout of the third experiment.

The volume of the reactor used for the experiment was equal to $3.23 \cdot 10^{-6} m^3$, being the diameter of the tube 15.37 mm and the L/D ratio equal to 1.5. As a first approximation, the hematite particles were considered to be spherical with a diameter of $80 \mu m$ [21].

In order to calculate the number of particles contained inside the volume of the reactor, the following formula was used:

$$N_{spheres} = \frac{6(1 - E) \cdot V_{tot}}{\pi d^3} \quad (4.2)$$

Knowing the number of particles, which is equal to 8438246, and the area of the single particle, it is possible to calculate the total area of reaction by multiplying these two quantities. As a result, this area will be equal to $0.68 m^2$. For what concerns the initial conditions of the reactant, the inlet value of the gas concentrations was set to zero (as a result of the voiding function of the pump). The surface concentration of the powders was also required for the initialization: it could be calculated by considering the moles of hematite present inside the pipe and dividing it by the surface of reaction. Given the mass of hematite powders, which is equal to 2.7 g, the surface concentration can be set to $0.05 mol/m^2$. Furthermore, the number of reacting sites can be calculated by multiplying the surface concentration by the number of oxygen atoms present inside the hematite, which is equal to 3. As a result, the number of reactive sites is $0.15 mol/m^2$. Additionally, an inlet flow of the CH_4/N_2 mixture was considered (with the usual proportion of 35% methane and 65% nitrogen).

The result of the simulation can be seen in the following:

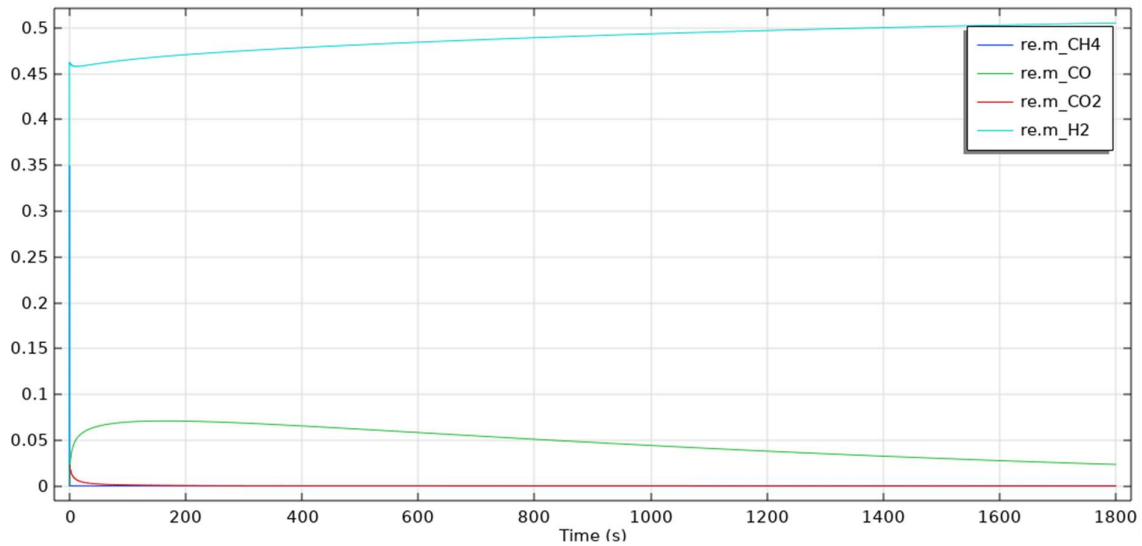


Figure 78: Simulation output.

Here we can see the plot against time of the output gases concentrations. In particular, in fig. 79 it is possible to see the concentrations of CH_4 , H_2 , CO and CO_2 . It's also interesting to compare the simulation's results with the outcome of the third experiment:

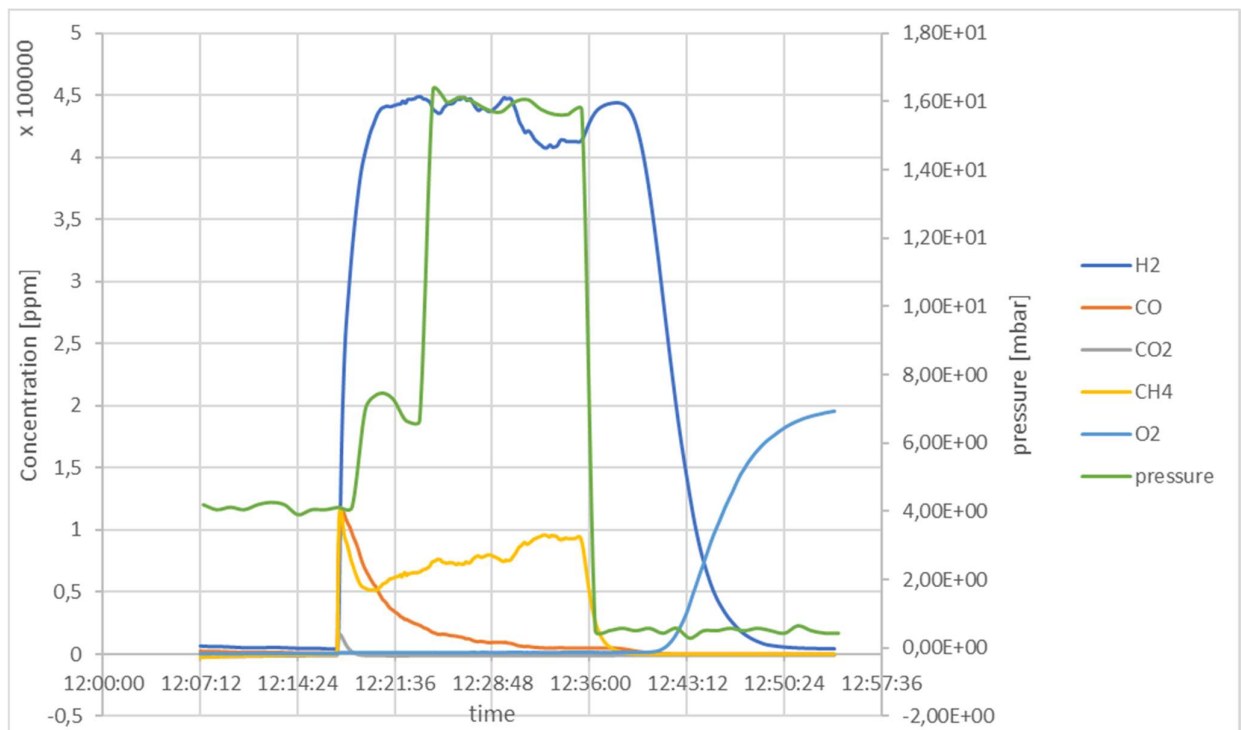


Figure 79: Result of #3 experimental test.

In both the real and simulated case, an interesting aspect can be observed: as soon as the reaction starts, thanks to the external heat provided and to the methane injected, the sudden increase in the concentration of the other gases is detected. Furthermore, a similarity in the output concentration of hydrogen can be seen: in the simulation the concentration of H_2 ranges between 40% and 50%, while in the experimental test it would have a similar output, ranging between 40% and 45%. However, this similarity doesn't last for long due to the failure of the pipe during the experimental testing, which provoked a sudden decrease of the H_2 concentration. For what concerns CO we can also note a similarity: in both experimental results and simulation it can be seen how the CO concentration peaks between 10% and 15% and then decreases shortly after. The same trend can be noted for the CO_2 which however has much lower values.

The main difference can be noted in the output concentrations of methane: in the experimental test the analytic could detect a non-negligible fraction of unreacted methane, of which we have no trace in the simulation's result. This can be attributed to the fact that these sources of imperfection that occurred during the testing due to the not constant meteorological conditions cannot be represented in the simulation because of the ideality of its results.

Another interesting result can be seen in the fig. 81:

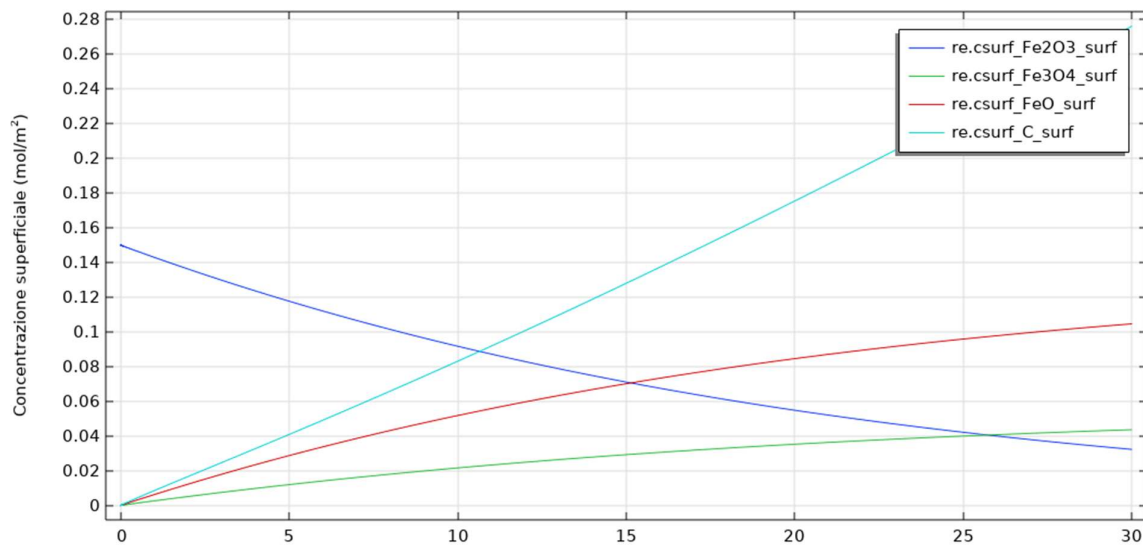


Figure 80: Surface concentration of solid components.

Here, it can be noted how the hematite concentration, which initially is the only solid component present, slowly decreases with time, while the concentration of Fe_3O_4 (magnetite)

and FeO (wustite) gradually increase. The fact that the wustite is more abundant reveals that the tendency of the reaction toward complete reduction is more relevant than the one of partial reduction. It can also be noted the increase in concentration of solid carbon over the carrier. The reason for this increase can be found in the methane cracking reaction, which is boosted in this temperature range.

5 Conclusions

In this study many aspects for the production of green hydrogen via chemical looping were assessed, starting from the review of the state of the art of CSP technology, followed by the analysis from a chemical point of view of the mentioned process. The literature review on chemical looping reduction and oxygen carriers for hydrogen production was used in order to properly set up the experiments carried out on the rooftop of the Energy Center facility. In particular, the use of methane as a reducing agent allowed the realization of the experiments without requiring the very high temperatures normally needed for the thermal reduction process. A particular issue encountered during the experimental phase of this study are related to the material of which the reactor was made of. Indeed, alumina, being a ceramic material, has very low thermal shock resistance, and if subject to high thermal ramps, as it can happen in the focus of the solar concentrator, will eventually break. In fact, during the two experiments in which the alumina tubes were used, the reactor failed as soon as it underwent the thermal shock. Looking for a material with higher thermal shock resistance, the following experiments

were lead using metallic reactors, even if the temperatures reached during the process were well above their melting points. Indeed, all the experiments performed had a destructive ending for the reactors' material. However, the Hastelloy pipe kept its structural integrity for longer compared to the other reactors and allowed to perform the measurements of the flue gases concentrations. This allowed to demonstrate that this kind of reaction is feasible in field experiments, and not only in laboratories. It is possible to state that the amount of hydrogen produced in the reduction step is already relevant: as it can be seen in the #3 experiment, its concentration was up to half of the total gases at the output of the reactor. The rest is composed by small quantities of CO, CO₂ and unreacted methane. It can also be said that, as shown in fig. 81, the partial oxidation was more relevant than the total oxidation, especially in more mature stages of the reaction. It is important to highlight the effect that meteorological conditions on the experiment itself: not only the presence of clouds would make the reaction stop due to the sudden drop of temperature, but it would also cause the forementioned phenomena of failure caused by thermal shock because of the high temperature gradient that occurs on the reactor's surface. This study leaves space to further investigation on the reactor's material: indeed, a suitable solution for this problem would be the exploitation of a metal with much higher melting point than the ones used as reactors. From the chemical loop's point of view, this work covered the reduction phase only. Space for deeper analysis is left for what concerns the oxidation step.

References

- [1] R. Guédez, A Techno-Economic Framework for the Analysis of Concentrating Solar Power Plants with Storage.
- [2] Y. L. He, K. Wang, Y. Qiu, B. C. Du, Q. Liang, and S. Du, “Review of the solar flux distribution in concentrated solar power: Non-uniform features, challenges, and solutions,” *Applied Thermal Engineering*, vol. 149. Elsevier Ltd, pp. 448–474, Feb. 25, 2019. doi: 10.1016/j.applthermaleng.2018.12.006.
- [3] A. Z. Hafez, A. Soliman, K. A. El-Metwally, and I. M. Ismail, “Design analysis factors and specifications of solar dish technologies for different systems and applications,” *Renewable and Sustainable Energy Reviews*, vol. 67. Elsevier Ltd, pp. 1019–1036, Jan. 01, 2017. doi: 10.1016/j.rser.2016.09.077.
- [4] “Descrizione collettori solari a concentrazione. 1 di 6.”
- [5] M. Günther, R. Shahbazfar, R. T. Fend, and M. Hamdan, “Advanced CSP Teaching Materials Solar Dish Technology.”
- [6] M. Günther, M. Joemann, S. Csambor, R. A. Guizani, D. Krüger, and T. Hirsch, “Advanced CSP Teaching Materials Parabolic Trough Technology.”
- [7] Pertti. Auerkari, Mechanical and physical properties of engineering alumina ceramics. Technical Research Centre of Finland, 1996.

- [8] M. Romedenne, R. Pillai, M. Kirka, and S. Dryepondt, “High temperature air oxidation behavior of Hastelloy X processed by Electron Beam Melting (EBM) and Selective Laser Melting (SLM),” *Corrosion Science*, vol. 171, Jul. 2020, doi: 10.1016/j.corsci.2020.108647.
- [9] F. H. Çakır, M. A. Sofuoğlu, and S. Gürgen, “Machining of Hastelloy-X Based on Finite Element Modelling,” *Advanced Engineering Forum*, vol. 30, pp. 1–7, Nov. 2018, doi: 10.4028/www.scientific.net/aef.30.1.
- [10] J. Lu, E. S. Choi, and H. D. Zhou, “Physical properties of Hastelloy® C-276TM at cryogenic temperatures,” *Journal of Applied Physics*, vol. 103, no. 6, 2008, doi: 10.1063/1.2899058.
- [11] J.-H. Park, “Oxidation of Hastelloy C276,” Feb. 2003, pp. 495–502. doi: 10.1063/1.1472578.
- [12] A. Thomas, M. El-Wahabi, J. M. Cabrera, and J. M. Prado, “High temperature deformation of Inconel 718,” *Journal of Materials Processing Technology*, vol. 177, no. 1–3, pp. 469–472, Jul. 2006, doi: 10.1016/j.jmatprotec.2006.04.072.
- [13] E. Chlebus, K. Gruber, B. Kuźnicka, J. Kurzac, and T. Kurzynowski, “Effect of heat treatment on the microstructure and mechanical properties of Inconel 718 processed by selective laser melting,” *Materials Science and Engineering A*, vol. 639, pp. 647–655, Jul. 2015, doi: 10.1016/j.msea.2015.05.035.
- [14] T. E. Abioye, D. G. McCartney, and A. T. Clare, “Laser cladding of Inconel 625 wire for corrosion protection,” *Journal of Materials Processing Technology*, vol. 217, pp. 232–240, 2015, doi: 10.1016/j.jmatprotec.2014.10.024.
- [15] P. Furler, J. R. Scheffe, and A. Steinfeld, “Syngas production by simultaneous splitting of H₂O and CO₂ via ceria redox reactions in a high-temperature solar reactor,” *Energy and Environmental Science*, vol. 5, no. 3, pp. 6098–6103, Mar. 2012, doi: 10.1039/c1ee02620h.
- [16] M. Tang, L. Xu, and M. Fan, “Progress in oxygen carrier development of methane-based chemical-looping reforming: A review,” *Applied Energy*, vol. 151, Elsevier Ltd, pp. 143–156, Aug. 01, 2015. doi: 10.1016/j.apenergy.2015.04.017.
- [17] “Perovskite-type oxides LaFe_{1-x}Co_xO₃ for chemical looping steam methane reforming to syngas and hydrogen co-production”.
- [18] T. Rager and J. Golczewski, “Solar-Thermal Zinc Oxide Reduction Assisted by a Second Redox Pair,” 2005.
- [19] † A Weidenkaff, A. Steinfeld, A. Wokaun, P. O. Auer, B. Eichler, and A. Reller, “DIRECT SOLAR THERMAL DISSOCIATION OF ZINC OXIDE: CONDENSATION AND CRYSTALLISATION OF ZINC IN THE PRESENCE OF OXYGEN,” 1999.

- [20] G. Levêque and S. Abanades, "Investigation of thermal and carbothermal reduction of volatile oxides (ZnO, SnO₂, GeO₂, and MgO) via solar-driven vacuum thermogravimetry for thermochemical production of solar fuels," *Thermochimica Acta*, vol. 605, pp. 86–94, Apr. 2015, doi: 10.1016/j.tca.2015.02.015.
- [21] W. Villasmil, M. Brkic, D. Wullemin, A. Meier, and A. Steinfeld, "Pilot scale demonstration of a 100-kWth solar thermochemical plant for the thermal dissociation of ZnO," *Journal of Solar Energy Engineering, Transactions of the ASME*, vol. 136, no. 1, 2014, doi: 10.1115/1.4025512.
- [22] T. Nakamura, "HYDROGEN PRODUCTION FROM WATER UTILIZING SOLAR HEAT AT HIGH TEMPERATURES," Pergamon Press, 1977.
- [23] L. Shen, J. Wu, J. Xiao, Q. Song, and R. Xiao, "Chemical-looping combustion of biomass in a 10 kWth reactor with iron oxide as an oxygen carrier," *Energy and Fuels*, vol. 23, no. 5, pp. 2498–2505, May 2009, doi: 10.1021/ef900033n.
- [24] L. Huang, M. Tang, M. Fan, and H. Cheng, "Density functional theory study on the reaction between hematite and methane during chemical looping process," *Applied Energy*, vol. 159, pp. 132–144, Dec. 2015, doi: 10.1016/j.apenergy.2015.08.118.
- [25] D. Li, R. Xu, Z. Gu, X. Zhu, S. Qing, and K. Li, "Chemical-Looping Conversion of Methane: A Review," *Energy Technology*, vol. 8, no. 8. Wiley-VCH Verlag, Aug. 01, 2020. doi: 10.1002/ente.201900925.
- [26] D. Ghosh, A. K. Roy, and A. Ghosh, "Reduction of Ferric Oxide Pellets with Methane*," 1986.
- [27] C. Lu et al., "Chemical looping reforming of methane using magnetite as oxygen carrier: Structure evolution and reduction kinetics," *Applied Energy*, vol. 211, pp. 1–14, Feb. 2018, doi: 10.1016/j.apenergy.2017.11.049.
- [28] E. R. Monazam, R. W. Breault, R. Siriwardane, G. Richards, and S. Carpenter, "Kinetics of the reduction of hematite (Fe₂O₃) by methane (CH₄) during chemical looping combustion: A global mechanism," *Chemical Engineering Journal*, vol. 232, pp. 478–487, Oct. 2013, doi: 10.1016/j.cej.2013.07.091.
- [29] A. A. El-geassy M Nasr and M. M. Hessien, "Effect Iron of Reducing Gas on the Oxide Compacts VolumeChange during Reduction of," 1996.
- [30] P. Charvin, S. Abanades, G. Flamant, and F. Lemort, "Two-step water splitting thermochemical cycle based on iron oxide redox pair for solar hydrogen production," *Energy*, vol. 32, no. 7, pp. 1124–1133, 2007, doi: 10.1016/j.energy.2006.07.023.
- [31] L. Ma et al., "Spinel-Structured Ternary Ferrites as Effective Agents for Chemical Looping CO₂ Splitting," *Industrial and Engineering Chemistry Research*, vol. 59, no. 15, pp. 6924–6930, Apr. 2020, doi: 10.1021/acs.iecr.9b06799.

- [32] M. Guo et al., “Cobalt doping modification for enhanced methane conversion at low temperature in chemical looping reforming systems,” *Catalysis Today*, vol. 350, pp. 156–164, Jun. 2020, doi: 10.1016/j.cattod.2019.06.016.
- [33] E. R. Monazam, R. W. Breault, and R. Siriwardane, “Kinetics of hematite to wüstite by hydrogen for chemical looping combustion,” *Energy and Fuels*, vol. 28, no. 8, pp. 5406–5414, Aug. 2014, doi: 10.1021/ef501100b.
- [34] J. T. Slycke, E. J. Mittemeijer, and M. A. J. Somers, “Thermodynamics and kinetics of gas and gas-solid reactions,” in *Thermochemical Surface Engineering of Steels: Improving Materials Performance*, Elsevier Inc., 2015, pp. 3–111. doi: 10.1533/9780857096524.1.3.

